論文 / 著書情報
Article / Book Information

題目(和文)	
Title(English)	Impact of global climate change and urbanization on the regional climate of megacities worldwide
著者(和文)	Do Ngoc Khanh
Author(English)	Do Ngoc Khanh
出典(和文)	学位:博士(工学), 学位授与機関:東京工業大学, 報告番号:甲第12757号, 授与年月日:2024年3月26日, 学位の種別:課程博士, 審査員:神田 学,木内 豪,髙木 泰士,中村 恭志,中村 隆志,VARQUEZ ALVIN CHRIST
Citation(English)	Degree:Doctor (Engineering), Conferring organization: Tokyo Institute of Technology, Report number:甲第12757号, Conferred date:2024/3/26, Degree Type:Course doctor, Examiner:,,,,,
学位種別(和文)	博士論文
Type(English)	Doctoral Thesis

Impact of Global Climate Change and Urbanization on the Regional Climate of Megacities Worldwide

Do Ngoc Khanh

Doctoral Dissertation

Global Engineering for Development, Environment and Society Course
Department of Transdisciplinary Science and Engineering
School of Environment and Society
Tokyo Institute of Technology

2024

Acknowledgements

I would like to express my gratitude to the following people and groups.

Firstly, I would like to thank Prof. Kanda for his supervision. His guidance and general suggestions were helpful in structuring, conducting the research, and presenting research results. I believe that his suggestion for creating appealing and concise titles for research papers and research proposals will be useful for the rest of my career.

Secondly, I would also like to thank Assoc. Prof. Varquez for his advice, comments, guidance in conducting research, and casual non-academic talk. He was important to me not only because he was my doctoral co-supervisor but also because he has been supporting me continuously since the time I enrolled in Tokyo Tech under the Global Scientists and Engineers Program (GSEP) eight years ago.

Thirdly, I also wish to thank Asst. Prof. Inagaki for his academic advice and Ms. Okamoto for her support on administrative procedures.

Fourthly, it was my pleasure to closely cooperate with Kanda laboratory's members, especially, Ms. Narita, Dr. Junnaedhi, and Mr. Hiroki. For the other members who I did not work closely with, it was very enjoyable to have casual discussions and lunch time with you.

Fifthly, I am grateful for the continued financial support of the Ministry of Education, Culture, Sports, Science and Technology for my study at Tokyo Institute of Technology since 2016.

Finally, I would like to dedicate this dissertation to my beloved family, especially my grandmother.

Contents

List of Figures

Chapter 1

Introduction

This chapter reviews the background of this study (climate change and urbanization), identifies research gaps, and sets the the study's scope and objectives.

1.1 Global Climate Change

Global climate change is progressing at unprecedented rate with global surface temperature of approximately 1.1 °C higher than 1850–1900 in 2011–2020. At the 2015 United Nations Climate Change Conference (COP21), the Paris Agreement, which sets a target of limiting global warming to 1.5 °C above pre-industrial level, was adopted. However, the latest state of knowledge reveals that it is more than 50 % certain that global warming will reach 1.5 °C in 2021–2040 although it may decline afterward in certain scenarios. In order to achieve the targets of the Paris Agreement, each country can make its own nationally determined contribution (NDCs) to set of its climate-related target. However, as of October 2021, the declared commitments and the actual implemented policies might not be enough to limit warming below 2 °C (IPCC, 2023).

More than a century ago, the Swedish Nobel laureate Svante Arrhenius discovered that carbon dioxide is a driving factor for global warming. Specifically, Arrhenius found that doubling atmospheric carbon dioxide (CO_2) will lead to a 5 K increase in Earth's surface temperature near the Equator and a 6 K increase in high latitudes. Moreover, tripling CO_2 will lead to increases of 7 K and 9 K, respectively (Arrhenius, 1896). Since the industrial revolution, fossil fuels have become an integral part of the modern society. The combustion of fossil fuels and other human activities inevitably emit many greenhouse gases (GHGs) (including CO_2, methane (CH_4), and nitrous oxide (N_2O)) and eventually cause global warming.

However, it took many decades of research and debates after the discovery of the mechanism until the scientific and political consensus that global warming is caused by human activities is established. This development of consensus can be seen from the series of Assessment Reports (ARs) published by the Intergovernmental Panel of Climate Change (IPCC), which regularly conducts reviews of published research concerning climate change and summarizes research findings in the ARs starting from the First Assessment Report (FAR) published in 1990 until the latest Sixth

Assessment Report (AR6) published from 2021 to 2023. The assessment about whether the observed warming is human-caused in the ARs reads as follows.

- In the First Assessment Report (FAR): "The observed increase [0.3 to 0.6 °C of global mean surface air temperature over the last 100 years] could be largely due to … natural [climate] variability" (IPCC, 1992).
- In the Second Assessment Report (SAR): "[T]he balance of evidence suggests that there is a discernible human influence on global climate" (IPCC, 1995).
- In the Third Assessment Report (TAR): "There is new and stronger evidence that most of the warming observed over the last 50 years is attributable to human activities. … The observed warming over the 20th century is unlikely to be entirely natural in origin" (IPCC, 2001).
- In the Fourth Assessment Report (AR4): "Most of the observed increase in global average temperatures since the mid-20th century is *very likely* [> 90 %] due to the observed increase in anthropogenic GHG concentrations. It is *likely* [> 66 %] that there has been significant anthropogenic warming over the past 50 years averaged over each continent (except Antarctica)" (IPCC, 2007).
- In the Fifth Assessment Report (AR5): "Human influence [on the climate system] … is *extremely likely* [95 to 100 %] to have been the dominant cause of the observed warming since the mid-20th century" (IPCC, 2014).
- In the Sixth Assessment Report (AR6): "Human activities, principally through emissions of greenhouse gases, have *unequivocally* [emphasis added] caused global warming, with global surface temperature reaching 1.1 °C above 1850–1900 in 2011–2020" (IPCC, 2023).

In three decades, the language concerning the attribution of human activities to observed warming has changed from *the observed increase could be largely due to natural climate variability* to *human activities have unequivocally caused global warming*. This development in confidence of the statement could not be possible without the efforts of the scientific community in the development of advanced climate models and collection of large observation database.

Impacts of climate change is expected to be widespread among the atmosphere, ocean, cryosphere, and biosphere. With high confidence, climate change is expected to have adverse impacts on health and well-being (including heat, malnutrition, and harm from wildfire; mental health; and displacement); cities, settlements, and infrastructure (inland flooding and associated damages, flood/storm induced damages in coastal areas; and damages to infrastructure). Climate change is also expected to cause changes in the terrestrial, freshwater and, ocean ecosystems with high confidence. In terms of climate justice, communities which historically have little contribution to the current climate change are disproportionately affected. At the end of this century, humans may live in a world of 1 to 4 °C warming, depending on the pathway we decided to take and make commitment for (IPCC, 2023). That is to say, even though global warming and climate change are undesirable and may have devastating consequences, with determined efforts, the problem is still within our control.

1.2 Cities and Urbanization

While there is probably no definite answer to the question of when the first city came into its existence, it is known that cities in Mesopotamia (parts of present-day Iran, Kuwait, Syria, and Turkey) formed as early as the fourth millennium B.C. (Aruz, 2003). Since then, urbanization, in other words, formation of cities and the aggregation of people to cities, has been an inseparable part of human history. There are social science theories considering the process of urbanization as a byproduct of economic development. But there are also arguments that urbanization is driven by technological and institutional changes (for example, investments in health care, education, infrastructure) which increase the surplus of food supplies to support nonagricultural urban population and improve the resilience of densely populated urban settlements against infectious and parasitic diseases (Fox, 2012).

In modern history, urban population was about half of rural population in 1950 but became equal to the rural population near 2006 and is projected to be twice the rural population in 2050. World rural population has recorded almost no growth since the beginning of the millennium and is expected to start declining (UN-Habitat, 2022). Therefore, it can be said that virtually all newly born human are born in cities. The global annual rate of urban population in the 2015–2050 period is 1.48 % but there is a large variance between regions. While the rate is only 0.39 % in more developed regions, it is 2.09 % in less developed regions. Continental-wise, Africa has the highest annual rate of 3.17 % (UN-Habitat, 2022).

While the exact definition of what is a city is still under discussion, recently, a method called "Degree of Urbanization", proposed by six international organizations, defining cities as settlements with "population of at least 50 000 inhabitants in contiguous dense grid cells (> 1500 inhabitants per km^2)" was endorsed by the UN Statistical Commission in its 51st Session (Dijkstra et al., 2020). When classified by size, cities in the category with largest size are called megacities—cities with population of 10 million or more. The world had 33 megacities in 2018 and is expected to have 43 megacities by 2030 (UN DESA, 2018). These megacities are projected to house 8.8 percent of the world population by 2030. These megacities are the investigation target of this study.

From a meteorological and climatological point of view, there is a distinctive phenomenon called *urban heat island* (UHI) occurring in cities. UHI is the phenomenon that urban area are warmer than its surrounding. Luke Howard first observed and recorded the abnormal warmth of London seasonally and diurnally in the early 1800s (Oke et al., 2017, pp. 454–455). UHI has impact on energy demand for heating and cooling, exacerbate risks to human under heatwaves, and affect records of meteorological stations in urbanizing area which may worsen quality of inputs for global background climate change study (Oke et al., 2017, p. 237; Fujibe, 2011; D. Li & Bou-Zeid, 2013). The cause of UHI has long been thought to be due to the imperviousness of cities. Specifically, because cities are more impervious (i.e., less greeny) than its rural surrounding, evaporative cooling is reduced and sensible heat is enhanced. Consequentially, urban area becomes warmer (Oke, 1982). However, recently, it was argued that UHI is due to aerodynamics roughness of cities. Specifically, if an urban area is smoother than its surrounding, heat convection is less efficient in the urban area than in the rural area, thus, UHI occurs. On the contrary, if the urban area is rougher than its surrounding, it may become a heat sink (Zhao et al., 2014). However, subsequent research argued that the answer to the question of whether UHI is due to imperviousness or aerodynamics roughness may vary due to attribution method. It is then suggested that variations of daytime UHI is caused by the difference in the ability to evaporate water of urban and rural areas (D. Li et al., 2019). While it may take more time for the scientific process to finally figure out the root cause of UHI, the current state of knowledge agrees that change in land cover, building geometries, urban materials, and heat released from human activities (so-called, anthropogenic heat) are driving factors of UHI and it is possible to control UHI by adjusting those factors. Moreover, while UHI increases heat stress risks to human and reducing UHI may reduce these risks, UHI should not be the sole focus of heat mitigation study because the background climate can also be hazardous (Martilli et al., 2020).

1.3 Research Gaps

Because global climate change and urbanization are happening simultaneously and cities have great concentration of population, it is important to understand the interaction between climate change and urbanization so that future climate of cities can be better projected. Proper projection of future climate is crucial for proper projection of climate-related risks and proposal of mitigation and adaptation strategies. In the field of urban climatology, many studies have highlighted the contribution of urban warming to warming trend at cities (Levermore et al., 2018; Varquez & Kanda, 2018; F. Wang et al., 2015). The aim of the field also includes understanding the past, present, and future urban climate of cities (Adachi et al., 2012; Argüeso et al., 2014; Darmanto et al., 2019; Doan et al., 2019; Giannaros et al., 2013; Lemonsu et al., 2013; Shen et al., 2023) and to project heat-related risks to human (Cheung & Hart, 2014; Takahashi et al., 2007; Varquez et al., 2020).

Future climate projection at a global scale can be done by running general circulation models (GCMs) under various socioeconomical scenarios. However, using GCMs is not the default choice for urban climatological study because of several reasons. Firstly, GCMs were not originally designed targeting urban climatological research because cities occupy less than 3 % of total global land area (Schneider et al., 2009; Zhou et al., 2015). For that reason, most existing global urban climate projections are non-urban climate projection (Zhao et al., 2021). Attempts to include more sophisticated urban representation in GCMs (D. Li et al., 2016) and to make multi-model projection of global urban climates (Zhao et al., 2021) are relatively recent. Despite these recent advancements, urbanization is still a process not considered explicitly in global climate projection. Secondly, even though GCMs can study bulk property of urban areas, they cannot study urban climate in high detail because urban extent is usually much smaller than the resolution of a GCM grid. In other word, for GCMs, urban meteorological and climatological process is mostly a sub-grid process. Increasing GCM spatial resolution is a direct solution but it is computationally impractical using current technologies, with the exception of demonstration to showcase model capability (Miyamoto et al., 2013).

In practice, regional climate models (RCM) coupled with urban surface models (Kusaka & Kimura, 2004; Masson, 2000; Wouters et al., 2016) are more suitable for study at city scale. They have been used to investigate urban heat island (H. Li et al., 2019; Varentsov et al., 2018), precipitation (Miao et al., 2011; Reder et al., 2022), and found potential in operational weather forecasting (Hamdi et al., 2012). In addition, using RCM to downscale GCMs' projection is one method to project future city climate. Projection for cities around the world have been conducted but there are some remaining issues, specifically on the following three points which will later become the focus of this study.

1. There are three important factors in urban modeling which are the present and futuristic spatially distributed projection of (1) urban morphological parameters (e.g., building height, plan area index, and roughness length), (2) urban expansion, and (3) anthropogenic heat emission. However, in past studies, these parameters were only partially considered. For example, one global study (McCarthy et al., 2010) considered anthropogenic heat but not heterogeneous urban morphological parameters nor urban expansion; a study for Tokyo (Adachi et al., 2012) considered spatially varying anthropogenic emission but used constant urban morphological parameters; a study for Sydney (Argüeso et al., 2014) considered urban expansion but completely ignore anthropogenic heat; a study for Hanoi (Doan et al., 2019) considered urban expansion and anthropogenic heat but did not mention urban morphological parameters (e.g., building height and roughness length). That is to say, the three factors have been considered more and more thoroughly, but they have not been considered fully yet.

2. It is not straightforward to generalize the methodologies of past studies due to their dependence on locally available datasets. For example, the study for Sydney (Argüeso et al., 2014) used local land use dataset, the study for Hanoi (Doan et al., 2019) used city future master plan, and the study for Tokyo (Adachi et al., 2012) used national energy use dataset. These local datasets are good for the concerned cities but they are not suitable for a multi-city study because they have not been available publicly for many cities worldwide yet. Moreover, it is difficult to collect and unite datasets of different format and not all cities have data and future plan published for a specific year or period (e.g., the 2050s).

3. In relation to the issues 1 and 2, there is additionally a geographical bias in urbanization and climate change study (Chapman et al., 2017). Specifically, while many studies were conducted for European, North American, and Chinese cities, few were conducted for the vulnerable South American and African cities. In addition to the geographical bias, the review also pointed out that only 14% of reviewed articles examined the combined effect of climate change and urban heat island and only 16% examined consequences to urban population. Recently, more studies (Geleta et al., 2022; He et al., 2022) have been done to address the geographical bias; however, the aforementioned issues (e.g., lack of consideration of urbanization and/or anthropogenic heat) persist.

1.4 Research Scope and Objectives

This research aims at contributing to the scientific understanding of interaction between global climate change and urbanization by attempting to filling in the aforementioned research gaps.

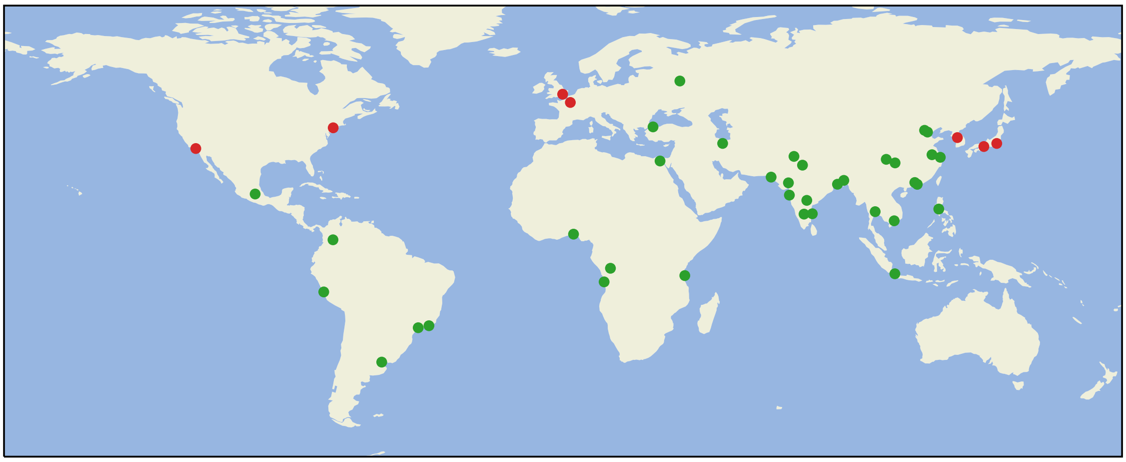

Figure 1.1: Locations of the world's 43 megacities. There are 7 megacities in developed countries (red dots) and 36 megacities in developing countries (green dots).

Table 1.1: List of 43 megacities (UN DESA, 2018). The city code of each city is taken from the IATA metropolitan area code or the code of a major international airport in the city.

City	Code	City	Code	City	Code	City	Code
Ahmadabad	AMD	Delhi	DEL	Lahore	LHE	Osaka	OSA
Bangalore	BLR	Dhaka	DAC	Lima	LIM	Paris	PAR
Bangkok	BKK	Guangzhou	CAN	London	LON	Rio de Janeiro	RIO
Beijing	PEK	Ho Chi Minh City	SGN	Los Angeles	LAX	Seoul	SEL
Bogota	BOG	Hyderabad	HYD	Luanda	LAD	Shanghai	SHA
Buenos Aires	BUE	Istanbul	IST	Manila	MNL	Shenzhen	SZX
Cairo	CAI	Jakarta	JKT	Mexico City	MEX	São Paulo	SAO
Chengdu	CTU	Karachi	KHI	Moscow	MOW	Tehran	THR
Chennai	MAA	Kinshasa	FIH	Mumbai	BOM	Tianjin	TSN
Chongqing	CKG	Kolkata	CCU	Nanjing	NKG	Tokyo	TYO
Dar es Salaam	DAR	Lagos	LOS	New York	NYC		

To address all the three issues concerning high-resolution regional climate projection for megacities identified in Section 1.3, the target of this research is to make high-resolution future climate projections for megacities which

- cover all 43 megacities (Table 1.1 and Fig. 1.1) classified by the United Nations (including African and South American cities, addressing issue 3),
- consider present and future spatially varying urban morphological parameters, urban expansion, and anthropogenic heat emission (addressing issue 1),
- use only public databases and open source software for the projection (addressing issue 2),
- focus on two aspects of urban warming (global warming and urbanization-induced warming),

- examine possible consequences to urban dwellers,
- publicize all global databases needed for climate projection of any cities of interest, not limited to megacities.

1.5 Structure of this Dissertation

This dissertation is divided into seven chapters as described graphically in Fig. 1.2 and textually follows.

- Chapter 1 (Introduction) reviews the background of this study (climate change and urbanization), identifies research gaps, and sets the scope and objectives for this study.
- Chapter 2 (Research Framework) overviews the theoretical framework and methodology of this study, including urban surface models, dynamical downscaling, and the pseudo-global warming method.
- Chapter 3 (Construction of Supporting Datasets) summarizes the procedure of constructing urban morphological parameters and anthropogenic heat dataset used as input for conducting numerical simulations in this study.
- Chapter 4 (Future Climate of Megacities: Summer Month Case Study) reports the results of a pilot study examining the feasibility of global meso-scale urban climate study for 43 megacities in a summer month (August).
- Chapter 5 (Future Climate of Megacities: Extension to Full Year) reports the results of a full-scale global urban climate study and identify impacts of global climate change and urbanization on exposure of megacity inhabitants to extreme warming.
- Chapter 6 (Future Climate of Megacities: Climate Extremes) examines possible interactions between global climate change and urbanization under several instance of heatwaves, a type of extreme weather events.
- Chapter 7 (Concluding Remarks) summarizes the main findings of this dissertation, identifies limitations, and proposes possible direction for future research.

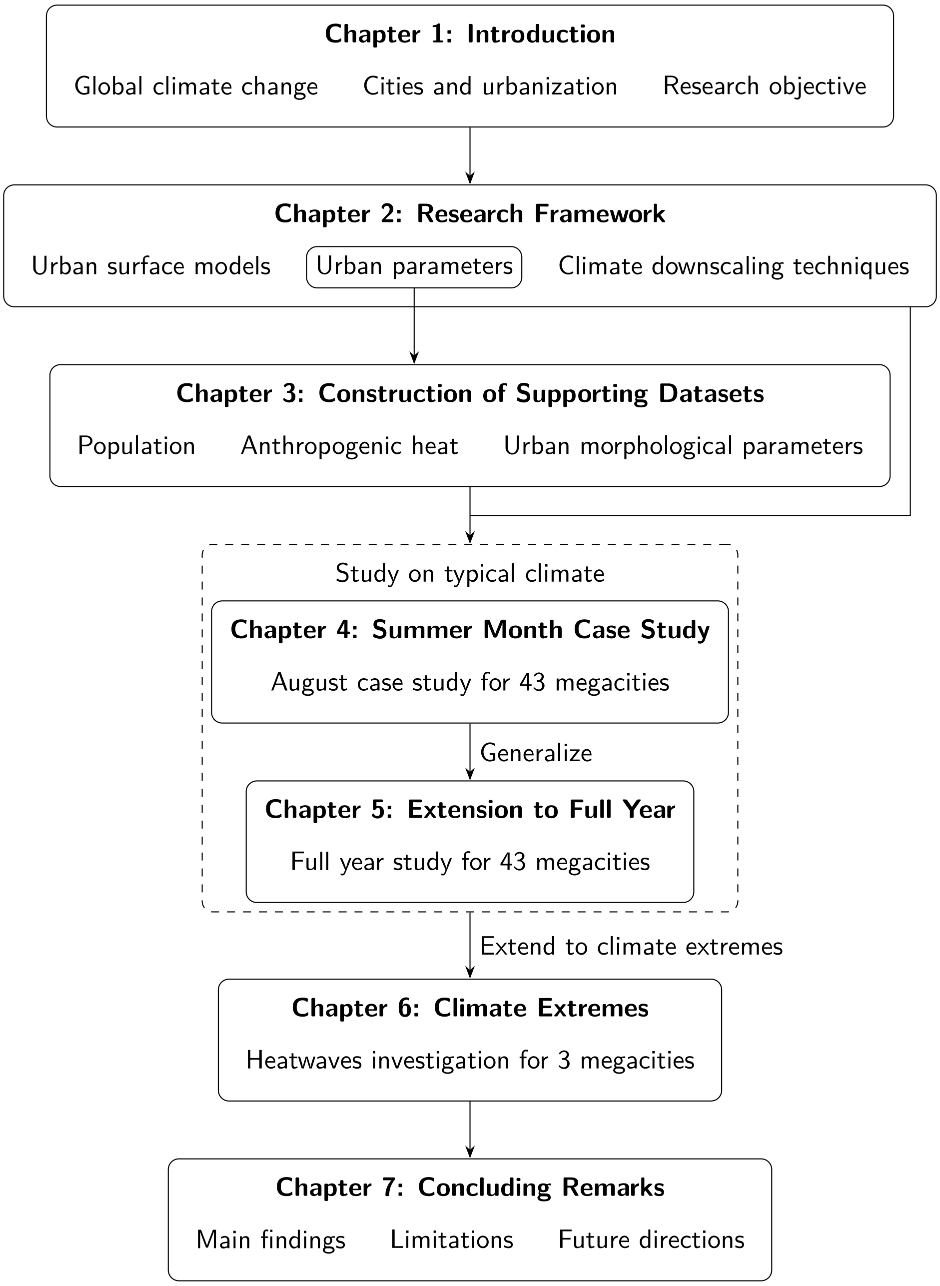

Figure 1.2: The structure of this dissertation.

CHAPTER **2**

Research Framework

This chapter overviews the theoretical framework and methodology of this study, including urban surface models, dynamical downscaling, and the pseudo-global warming method.

2.1 Energy Balance of Urban Surfaces

To understand the climatology of cities, it is crucial to understand the exchange of energy between urban surfaces and its surrounding (horizontal interaction) and the upper atmosphere (vertical interaction). The energy exchange is depicted conceptually in Fig. 2.1 and mathematically in the following equation of energy balance,

$$Q^* + Q_F = Q_H + Q_{LE} + \Delta Q_S + \Delta Q_A, \tag{2.1}$$

in which

- Q^* is the net all-wave radiation which accounts for downwelling and upwelling shortwave and longwave flux,
- Q_F is the anthropogenic heat flux, in other words, heat generated from human activities,
- Q_H is the sensible heat flux,
- Q_{LE} is the latent heat flux, which resulted from evapotranspiration,
- ΔQ_S is the change in the net energy stored in all urban structure (for example, building, roads, ground, air),
- $\Delta Q_A = Q_{A,in} - Q_{A,out}$ is the change in energy of the control volume due to advection, which is usually ignored/avoided in practice by selecting or assuming a large and horizontally homogenous urban surface (Oke et al., 2017, p. 159).

The net all-wave radiation Q^* can be expressed as

$$Q^* = K_{\downarrow} - K_{\uparrow} + L_{\downarrow} - L_{\uparrow}, \tag{2.2}$$

in which

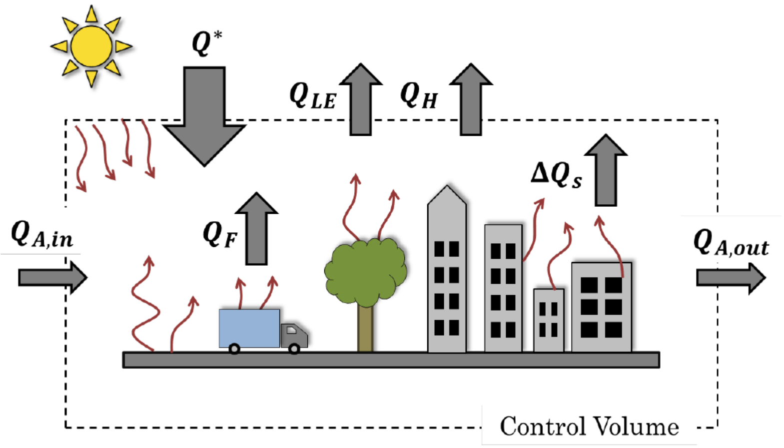

Figure 2.1: Energy balance of urban surface. (Source: Hrisko et al., 2020. © The Authors. Used under CC BY 4.0.)

- $K_\downarrow$ is the downward shortwave flux from the Sun,
- $K_\uparrow$ is the upward shortwave flux due to reflection,
- $L_\downarrow$ is the downward longwave flux emitted from the upper air, cloud droplets, aerosol particles, and others,
- $L_\uparrow$ is the upward longwave flux consisting of emitted the urban surface and reflected longwave radiation.

For a flat surface, the reflected upward shortwave radiation $K_\downarrow$ is a direct function of $K_\downarrow$ expressed as

$$K_\uparrow = \alpha K_\downarrow, \tag{2.3}$$

in which the albedo α is a dimensionless physical quantity describing the reflectivity of the surface with respect to shortwave radiation. Albedos for grass, fresh snow, and urban are 0.16–0.26, 0.80–0.90, and 0.09–0.23, respectively (Oke et al., 2017, p. 129).

Similarly, for a flat surface of temperature T, the upward longwave flux $L_\uparrow$ can be expressed as

$$L_\uparrow = \varepsilon\sigma T^4 + (1 - \varepsilon)L_\downarrow, \tag{2.4}$$

in which ε (dimensionless) is the emissivity of the surface and $\sigma \approx 5.67 \times 10^{-8}\,\mathrm{W\,m^{-2}\,K^{-4}}$ is the Stefan-Boltzmann constant. Most surfaces (with few exceptions such as coated windows and (polished) metals) have emissivity greater than 0.9 (Oke et al., 2017, pp. 129–130) and are closed to a black body (a body with an emissivity of unity). Consequently, most surfaces are good absorber of longwave radiation because they reflect less than 10 % of incoming longwave radiation.

In Eq. (2.1), there is only one unnatural term which is the anthropogenic heat flux Q_F. Unlike the other terms, Q_F does not strictly emerge from the surface or pass through the surface. In modeling, Q_F is occasionally added directly to surface sensible heat flux Q_H. However, from experience, this method of direct addition may give very high surface and near-surface temperature in locations with high Q_F such as power station. For that reason, considering the nature of Q_F which is mostly excess heat from combustion that directly modifies the temperature of the air, Q_F can be converted to the tendency of the temperature at the first level of atmosphere as in the following equation.

$$\frac{\partial T_{1,\mathrm{AH}}}{\partial t} = \frac{Q_F}{\rho c_p z_1}, \tag{2.5}$$

where

- $\frac{\partial T_{1,\mathrm{AH}}}{\partial t}$ ($\mathrm{K\,s^{-1}}$) is the in tendency of temperature at the first model level due to anthropogenic heat. The tendency due to other factors should be calculated by other components of the model,
- c_p ($\mathrm{J\,K^{-1}\,kg^{-1}}$) is the specific heat capacity of air,
- ρ ($\mathrm{kg\,m^{-3}}$) is the density of air,
- The product ρc_p ($\mathrm{J\,K^{-1}\,m^{-3}}$) is also called the volumetric heat capacity of air,
- z_1 (m) is the height of the first atmospheric level.

In this approach, it is assumed that all emitted anthropogenic heat will quickly rise to and heat up the upper atmosphere. Furthermore, Q_F is not a component of the energy balance equation (Eq. (2.1)). However, the energy balance of the surface is modified (indirectly) because hot air due to anthropogenic heat can enhance convection which in turns can modify surface temperature, sensible heat flux, and latent heat flux. This dissertation employs the latter approach in handling anthropogenic heat.

In reality, the urban surface is not a flat and homogenous surface but a heterogenous surface with three dimensional (3D) structures (mainly buildings) built on top. Hence, the urban surface has multiple facets, which are exposed to differently to radiation. Incoming radiation is reflected many times between different facets before finally get absorbed. Similarly, outgoing radiation is also multi-reflected before finally escape to the upper atmosphere. While accounting for these 3D properties of the urban surface has become the norm in the field of urban climatology; historically, development of urban surface models has started from regarding the urban surface as a flat surface nevertheless.

2.2 Urban Surface Models

Urban surface models belong to a bigger group of land surface models (LSMs)—models that simulate the exchange of energy, water, and occasionally other components of the atmosphere (for example, CO_2, NO_x) between the surface of the Earth and the upper atmosphere. While urban surface models in particular and LSMs in general can be used standalone, they are often used as a sub-model of a larger weather or climate model.

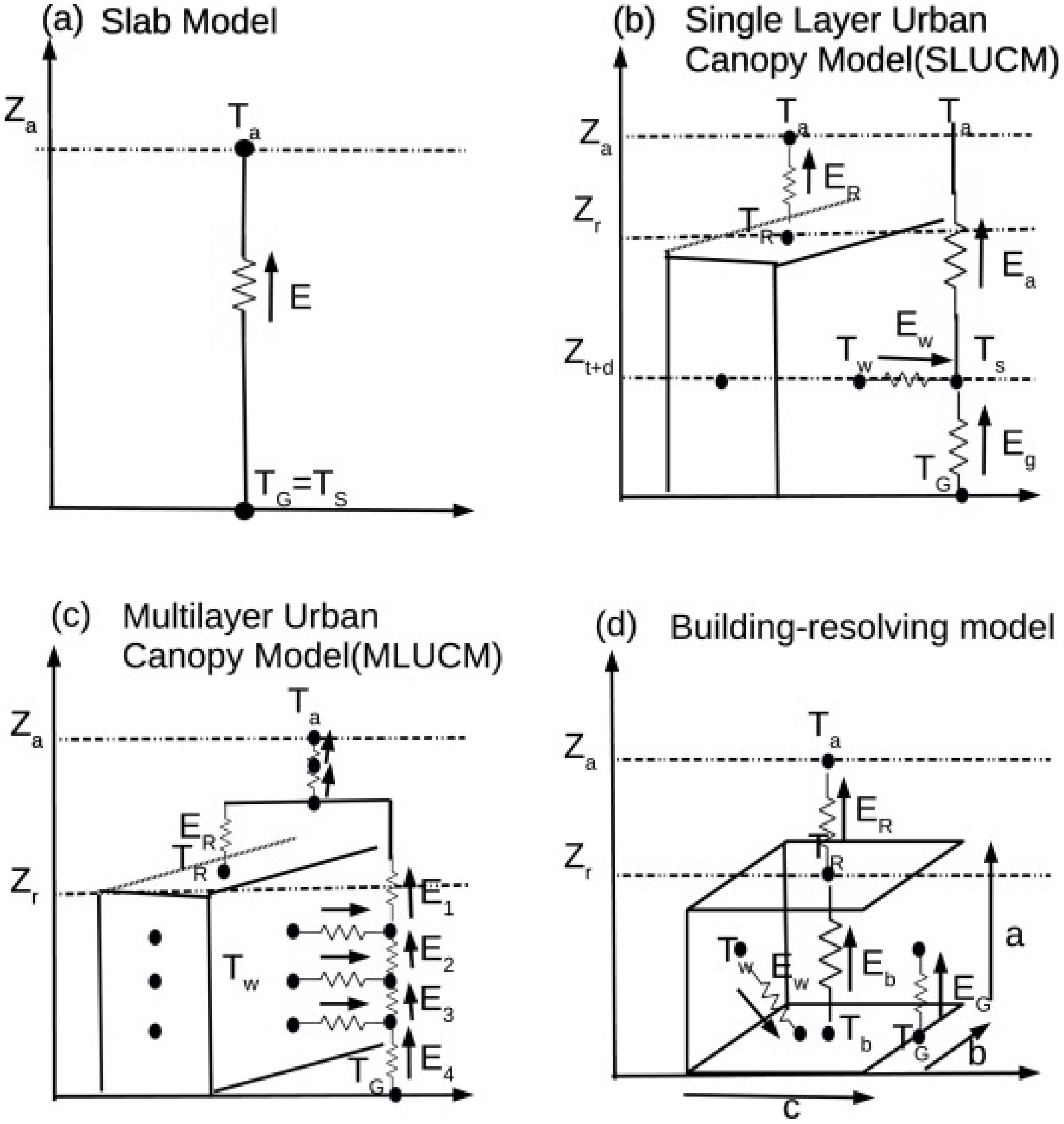

Figure 2.2: Major types of urban surface models. (Source: Garuma, 2018. © Elsevier. Used with permission.)

Slab models (Fig. 2.2(a)) are urban surface models in its simplest form. Slab models regard urban surface as flat soil/vegetation surfaces with large heat capacity (to account for heat storage in buildings), large roughness length (to account for drags), and/or small albedo. In slab models, three dimensional features of urban surface are not explicitly modeled and are expected to be (properly) implicitly modeled via the adjustment of the aforementioned parameters. Energy exchange between the surface and the upper atmosphere occurs without any obstruction. While slab models computational cheap, they were found to be unable to (1) capture heat storage of actual urban surfaces, which extends from the ground to certain height, because the only modeled heat sink is the ground; (2) capture drags due to buildings; (3) consider multi-reflection of radiation (Garuma, 2018). These drawbacks and the development of better urban surface models that incorporate three dimensional urban structures have made slab models no longer the default methods for urban climatological studies. However, it should be noted that slab models are still in used in the present, for example, in the JULES-GL7 land surface model (Wiltshire et al., 2020) which is a component of HadGEM3—a GCM member of the Coupled Model Intercomparison Project (CMIP).

A major advancement in the modeling of urban surface was the development of single-layer urban canopy models (Fig. 2.2(b)) such as the single-layer urban canopy model of Kusaka et al. (2001) and the Town Energy Balance scheme (TEB) of Masson (2000). While urban representation is greatly simplified as two infinitely long buildings located on two sides of an infinitely long road, important parameters that can capture the three-dimensional nature of urban surfaces such as building height, roof width, and road width were employed. Temperature of three surfaces (road, wall, and road) are simulated independently. The fluxes from three surfaces are then added up to get the total flux from the urban surface to the upper atmosphere. The formation of the model and the parameters make it possible for the models to account for influences of buildings to the flow and the reduction of incoming and outgoing longwave and shortwave flux due to shading and reflection. Single-layer urban canopy models were found to be better than slab models in modeling urban heat island (because of better simulated nighttime cooling rate) (Kusaka et al., 2012), surface energy balance (Shaffer et al., 2015), and temperature (Fallmann et al., 2013). However, it should be noted that all of these improvements does not necessarily emerge together. With few parameters to tune, low computational demand, and incorporation in well-known weather models such as WRF (Chen et al., 2011), single-layer urban canopy models have become a widely used option for urban climate modeling.

At higher complexity, there are multilayer urban canopy models (Fig. 2.2(c)) such as the BEP model by Martilli et al. (2002) and others (Kondo et al., 2005; Krayenhoff et al., 2020). It should be noted that while multilayer urban canopy models are more complex than single-layer urban canopy models, they were developed almost in parallel with each other. In multilayer urban canopy models, the canopy and the wall surface is sliced vertically into multiple layers and fluxes between these layer are simulated. To fully utilize a multilayer model, the bigger atmospheric model should have high vertical resolution close to the ground so that the urban canopy can be divided into multiple layers (Chen et al., 2011). In other words, if the concerned quantity is only the total feedback of the urban canopy to the upper atmosphere and close examination of the vertical profile of variables within the urban canopy is not needed, multilayer urban canopy model should, theoretically, have

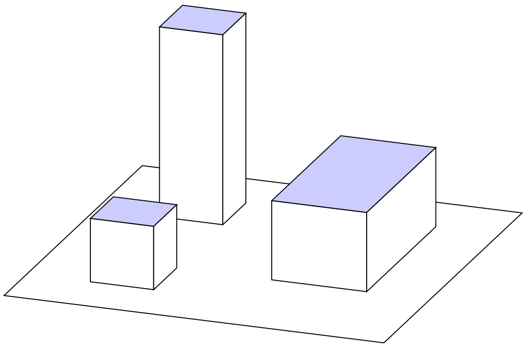

Figure 2.3: Plan area index λ_p

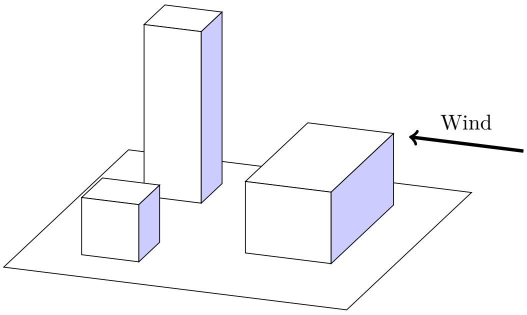

Figure 2.4: Frontal area index λ_f

equal performance with the simpler single-layer counterparts. Inter-model comparisons have also revealed that higher complexity does not necessarily lead to better performance (Best & Grimmond, 2013).

The most sophisticated urban surface models are building-resolving models (Fig. 2.2(d)). At this complexity, high-resolution (in the order of meters) computation fluid dynamics (CFD) models (for example, PALM, OpenFOAM, and other large-eddy simulation (LES) models) together with detailed information of every single building are used so that air flow, heat fluxes in and out of all buildings via all facets are resolved. They are capable of highly complicated tasks such as simulation of dispersion of particles in cities and generation of detailed wind hazard maps during typhoon (Ahmad et al., 2017; Karttunen et al., 2020; Takemi et al., 2019; Xie & Castro, 2009). These models are, in general, very computationally expensive. Therefore, unlike the three simpler urban surface models, building-resolving models are usually not coupled with atmospheric models in an online simulation. However, they can be used to simulate flow in and above cities to figure out the aerodynamic properties (for example, roughness length for momentum, zero-plane displacement height) of cities (Inagaki et al., 2022; Kanda et al., 2013). These properties are then used as input parameters for single-layer or multilayer urban canopy models coupled with larger weather models in online simulations.

2.3 Parameters in Urban Surface Models

Similar to all other surface models, there are also parameters that must be set so that urban surface models can perform its calculation. There are some common parameters that exist in all surface models (for example, albedo, emissivity, and heat conductivity). Therefore, in this section, some commonly used parameters which are specific to urban surface models in general and to single-urban canopy models in particular will be discussed.

Building height H (m) is probably the simplest parameters that can be used to describe the three dimensional nature of urban surfaces. Average building height H_{avg} is usually used but standard deviation σ_H, maximum building height H_{max}, and probability distribution functions of building height can also be used additionally.

Plan area index λ_p (dimensionless) is defined as the ratio of building footprints to the total

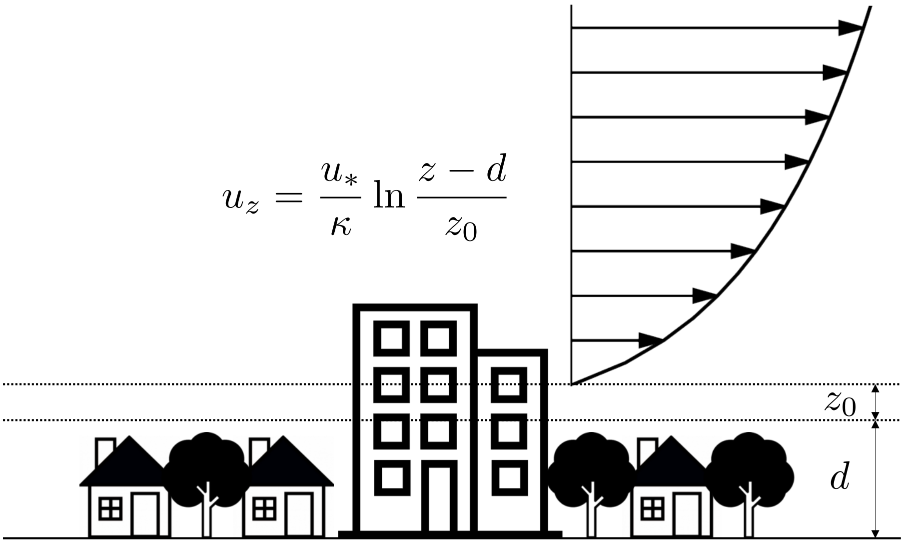

Figure 2.5: A conceptual image of the logarithmic wind profile over an urban area.

ground surface area (see Fig. 2.3). This value describes how densely buildings are packed in the area of interest.

Frontal area index λ_f (dimensionless) is defined similarly to the plan area index, frontal area index refers to the ratio of the total area of building facets facing the wind to the total ground surface area (see Fig. 2.4). By definition, λ_f is dependent on the direction of the incoming wind. In practice, a database of λ_f for several wind directions is stored (for example, as in the US National Urban Database and Access Portal Tool (NUDAPT) database (Ching et al., 2009)), or only a single value of λ_f is used assuming that the area of interest has wind-direction-independent λ_f. In a similar manner, the **vegetation fraction** λ_v (dimensionless) which describes the vegetation cover of the urban area of interest can also be defined.

When the atmosphere is neutrally stratified, mean wind speed u_z (m/s) at a certain height z (m) above the ground follows the logarithmic profile (Fig. 2.5) as described mathematically as

$$u_z = \frac{u_*}{\kappa} \ln \frac{z-d}{z_0}, \tag{2.6}$$

in which u_* (m/s) and $\kappa \approx 0.4$ are the friction velocity and the von Kármán constant, respectively. The remaining two parameters in the equation are the **roughness length for momentum** z_0 (m) and the **zero-plane displacement height** d (m), respectively. The roughness length z_0 describes how rough the surface the wind flow over is. The higher z_0, the more slowly the mean wind speed increases with height. On the other hand, the usage of the zero-plan displacement height is that, when the roughness elements (for example, trees, buildings) are densely pack, from the view point of the wind, it looks like the wind is flowing over a surface which is elevated from the actual ground by the height d.

Sky view factor (SVF, dimensionless) refers to the fraction of radiative flux leaving the surface at a certain point escapes from the canopy to the upper atmosphere (that is, the sky) (Oke et al.,

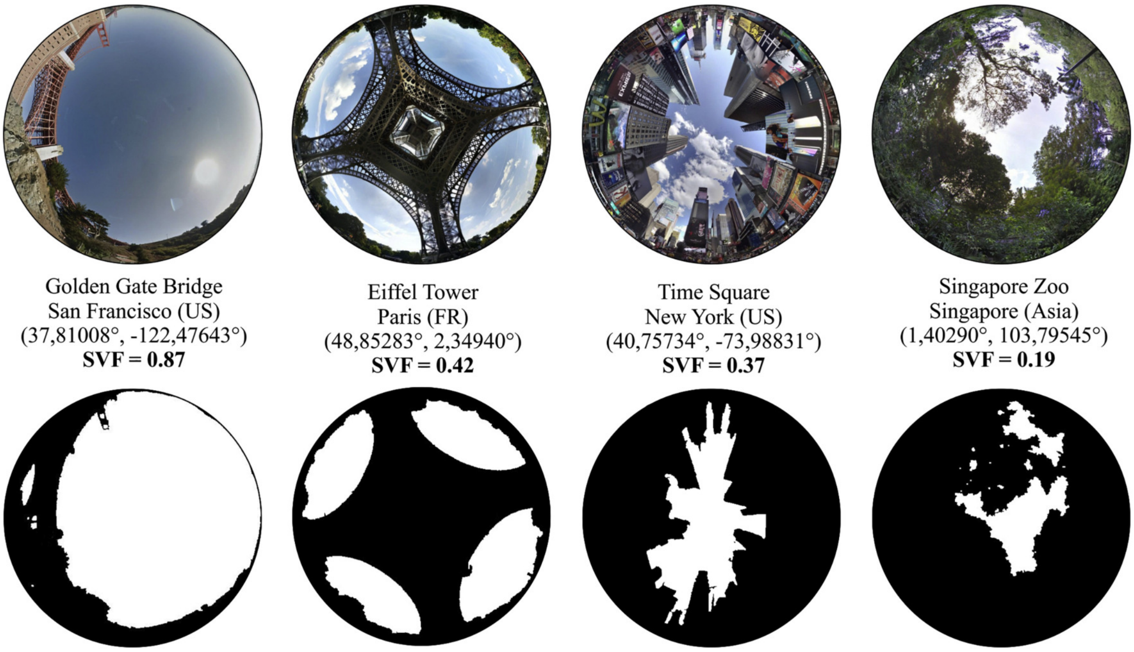

Figure 2.6: Fisheye photographs generated from Google Street View (top), detected horizon limitations (bottom), and respective Sky View Factors (bolded text) for four locations around the globe. (Source: Middel et al., 2018. © The Authors. Used under CC BY-NC-ND 4.0.)

2017, pp. 22–23). A value of unity implies the non-existence of canopy and unobstructed passage of fluxes. The smaller the value, the more fluxes are blocked. Intuitively, the larger portion of the sky we can see, the higher the SVF. Quantitatively, the SVF can be measured by fisheye lens or spherical cameras (Honjo et al., 2019; Steyn, 1980). Examples of SVFs for various locations calculated from fisheye photographs generated from Google Street View are given in Fig. 2.6 (Middel et al., 2018). Theoretically, the SVF is defined at every single point on the surface; thus, in practice, a spatial average value may be used.

Anthropogenic heat flux Q_F ($\mathrm{W/m^2}$) refers to the heat generated by human activities. This value can be prescribed in the model with a constant value and a diurnal variation pattern but can also be inputted using actual measurement data or estimated datasets.

In reality, urban surfaces are highly heterogenous. Therefore, the aforementioned parameters should be set to be varying with each grid. However, this has not always been the case. In the particular example of widely-used single-layer urban canopy model implemented in the Weather Research and Forecasting (WRF) model, urban land use are classified into three categories.

- Low intensity residential: An area which is less densely populated than high intensity residential areas. Land cover is 30–80 percent constructed materials and 20–70 percent vegetation.
- High intensity residential: An area which is highly developed with high population density. Land cover is 80–100 percent constructed materials and less then 20 percent vegetation.
- Commercial, Industrial, Transportation: Infrastructure and highly developed areas which are not high intensity residential.

For each of the urban land use categories, a set of urban parameters is tabulated and set as input to the model (Tewari et al., 2007). Because the tabulated parameters are certainly not universal, there have been studies attempting to modify the table to meet their specific need (Giannaros et al., 2013; H. Li et al., 2019). At the same time, there have been efforts to increase the number of categories. A notable example is the concept of Local Climate Zones (LCZs), which has 10 urban categories (Stewart & Oke, 2012), and the World Urban Database and Access Portal Tools (WUDAPT) which help facilitating the sharing of LCZ map and urban morphological information (Ching et al., 2018). On the other hand, there have also been efforts to create two dimensional maps of urban morphological parameters (Ching et al., 2009; Darmanto et al., 2017; Kawano, 2018; H. Li et al., 2021). It can be said that both the categorical and the two-dimensional mapping approaches are equally scientifically meaningful and each has its own advantages and disadvantages. Specifically, the mapping approach can faithfully capture urban surfaces but obtaining parameters for every single grid can be challenging. On the contrary, it maybe less challenging to classify urban surfaces to several categories and this information can be used to evaluate the impact of different class of settlements to the regional climate; however, it is uncertain if the diverse urban surfaces on Earth can be grouped into several categories. In this study, the mapping approach is selected because of data availability.

2.4 Downscaling of Future Climate Projection for Urban Climatological Studies

Global future climate projection are now, in general, made using general circulation models (GCMs). They are numerical models based on a set of theoretically, semi-theoretically and/or experimentally derived dynamical equations capable of simulating the Earth system. New generation of models are capable of simulating not only the atmosphere and ocean but also the biosphere. Output from GCMs play a crucial role in the Coupled Model Intercomparison Project (CMIP) which is an important input for the IPCC to write its Assessment Reports (ARs). While powerful for global climate modeling, GCMs are not quite a good candidate for regional urban climate modeling. Firstly, GCMs were not designed targeting urban climatological research. GCMs was not designed to model urban area because despite the large concentration of population in cities, cities occupy merely 0.2 to 2.7 % (varying among multiple estimates) of the total global land area (Schneider et al., 2009; Zhou et al., 2015). Therefore, it can be expected that the direct effect of urban area to the climate system is insignificant. Secondly, GCMs, in general, have coarse resolution in the order of hundreds of kilometers. To give a comparison, Tokyo Metropolitan Area—the largest urban agglomeration on Earth—only spans one hundred kilometers west-east and south-north. However, the coarse resolution of GCMs is understandable because they aim at simulating the general characteristics of the Earth system. Moreover, the resolution must be in balance with computational cost and GCMs' simulation time frame which can be decades, centuries, or even millennia. Note that even though there are GCMs at extremely high resolution in the order of kilometers or finer (for example, NICAM), but they are also extremely computational expensive, thus, unsuitable for practical and operational use at the moment. Therefore, it can be said that GCMs are not suitable for urban climatological studies because GCMs at coarse resolution are cannot resolve cities (because cities are too "small") and GCMs at high resolution are too expensive.

Because of the above reason, climate projection for cities are usually done by downscaling global climate projection produced by GCMs. Downscaling refers to the process of obtaining finer-resolution information from coarse one. The two commonly used methods are statistical downscaling and dynamical downscaling. Statistical downscaling refers to the process of using statistical tools (for example, empirical relations, statistical models) to link large-scale atmospheric variables (produced by GCMs) with regional-scale variables. The method can be used for downscaling of, for example, temperature (Huth, 2002), wind (Gonzalez-Aparicio et al., 2017), precipitation (Tareghian & Rasmussen, 2013), and extremes (Bürger et al., 2012). One strong advantage of statistical downscaling is low computational load. However, disadvantages of statistical downscaling include the lack/non-requirement of physical basis and the correctness of the assumption that known statistical relations will remain valid in the future (Ekström et al., 2015). In recent years, machine learning and deep learning approaches to downscaling are being increasingly developed (Oh et al., 2022; Sachindra et al., 2018). They can also be considered a form of statistical downscaling. The other commonly used method is dynamical downscaling. Dynamical downscaling feeds coarse resolution GCMs-projected variables into numerical models (usually regional climate models (RCMs)), consisting a set of physics-based equations that describe the state of the Earth system, to predict variables at regional or local scales. An advantage of dynamical downscaling is the ability to physically interpret its results because the models in use are physics-based and the validity physics-based equations does not depend on the time of application. Disadvantages of dynamical downscaling include high computational cost and uncertainty in model parameters (Martinez-García et al., 2021). Dynamical downscaling will be discussed further because it is the method used in this research.

Within dynamical downscaling, there are two commonly used approaches: direct downscaling (Fig. 2.7(a)) and pseudo-global warming method (Fig. 2.7(b)). In direct downscaling, as its name implied, output from one realization (a run) of GCM is directly used as the forcing for an RCM simulation and local-scale variables are obtained from the RCM output. This is almost no doubt about the logical soundness this method. However, practically, there are several issues. The first problem is that, each GCM, when compared with the observation data from the real Earth, has some biases in its output. Thus, when this output is used as the forcing for RCM, the output of RCM will also carry this bias. This issue is demonstrated by Fig. 2.8 which compared the observed annual average near-surface air temperature at Tokyo observation station and the annual average near-surface air temperature simulated by five GCM members of CMIP6 taken at the grid closest to the observation station. While the observation point in Tokyo is not meant to be representative of a GCM grid with hundred-kilometer resolution, it can be seen from the figure that bias in GCM output does exist (in the order of kelvins). Moreover, different GCMs don't necessarily agree with each other on the past climate of almost the same point on Earth even when the quantity in question is historical annual average temperature, which has already happened and has a known value. GCMs also show discrepancies even for the global average surface temperature, which is one of the most

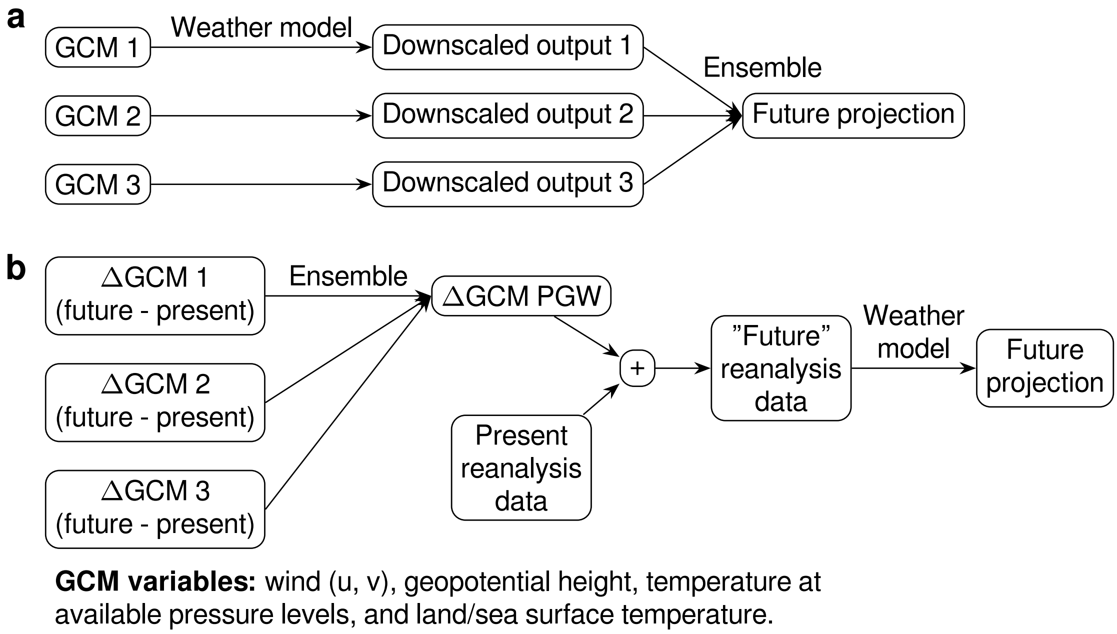

Figure 2.7: Two common methods for direct downscaling of global climate projections: (a) direct downscaling and (b) pseudo-global warming (PGW) method.

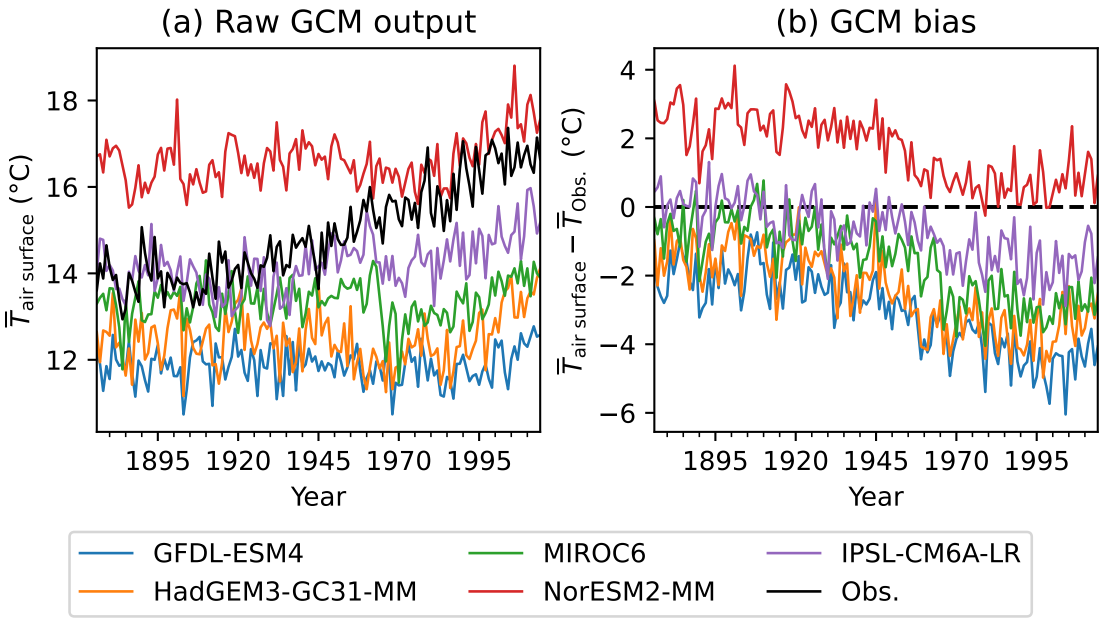

Figure 2.8: (a) Observed annual average near-surface air temperature at Tokyo observation station operated by the Japan Meteorological Agency (JMA) and the annual average near-surface air temperature simulated by five GCM members of CMIP6 taken at the grid closest to the observation station. (b) Bias of the simulated values against the observed values.

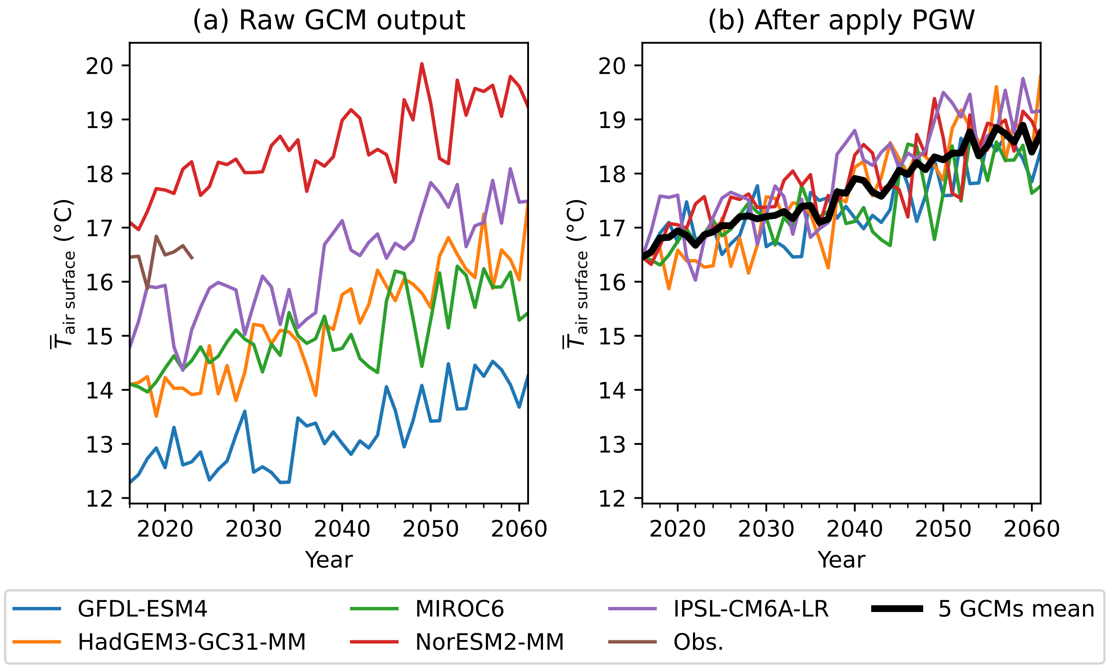

Figure 2.9: (a) Observed annual average near-surface air temperature at Tokyo observation station and future projections of the annual average near-surface air temperature made by five GCM members of CMIP6 taken at the grid closest to the observation station under the SSP5-8.5 scenario. (b) Future pathways of near-surface air temperature obtained by applying the PGW method.

basic variable (Fig. 2.10). The similar disagreement among models can be seen in their future projections (Fig. 2.9). However, it should be noted that while GCMs disagree on the exact value of a quantity, they agree on the anomaly when compared with reconstructed (in other words, observed or recorded) data (Fig. 2.10(b)) and also agree on the amplitude of variation (Fig. 2.9(b)). Therefore, it can be said that every GCM gives some useful information. The second problem is that, similar to bias, internal variability of the GCM also affect the output of RCM. The problems of bias and internal variability can be addressed by running a large ensemble of RCM simulations forced by many GCMs and many realizations. It can be expected that the large ensemble will help averaging out bias and internal variability and make it possible to obtain the "true" of more precisely, the most realistic downscaled climate signal. However, the large ensemble leads to the third practical issue of direct downscaling which is high computational cost and high preparation cost because a huge volume of GCM output needs be be downloaded, preprocessed, and then downscaled.

The other commonly used dynamical downscaling method is the pseudo-global warming (PGW) method (Fig. 2.7(b)) (Kimura & Kitoh, 2007; Schär et al., 1996). In this method, the differences between the GCM outputs in the future and a referenced present of multiple GCMs (and possibly multiple realizations) are ensemble averaged and then superimposed on (in other words, added to) a present reanalysis data to produce a "future" reanalysis data. This "future" reanalysis data is then inputted into an RCM so that it can be downscaled to higher resolution. The added variables are vertical profiles of wind speed (zonal and meridional), geopotential height and temperature; and the

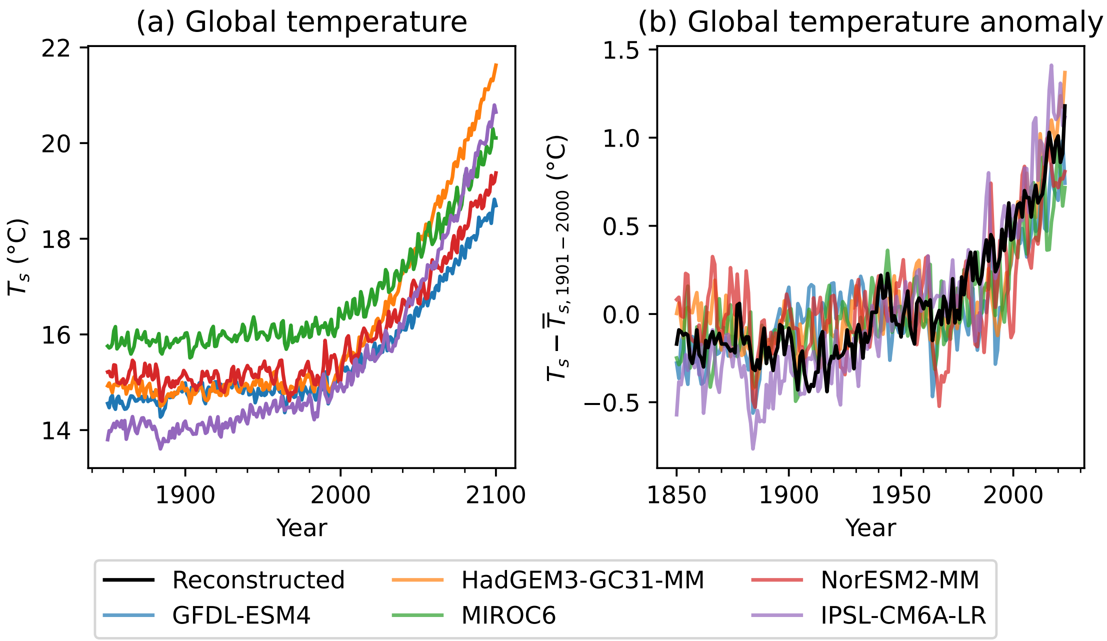

Figure 2.10: (a) Simulated global average surface temperature historically (1850–2014) and under ssp585 scenario (2015–2100) by five GCM members of CMIP6. (b) Historical global average surface temperature anomaly simulated by the five GCMs and reconstructed by the National Oceanic and Atmospheric Administration (NOAA) (NOAA NCEI, 2024). Reference for the anomaly is the 1901–2000 average.

surface temperature (including sea surface temperature). Humidity are usually not added because several reasons including (1) weak historical trend in relative humidity (Dai, 2006), (2) improperly adding absolute humidity may risk over-saturating the atmosphere at low temperature (Brogli et al., 2023), (3) it can be expected that RCM can solve for the new balance of water vapor based on the Clausius-Clapeyron relation (Adachi & Tomita, 2020). Because the ensemble average of multiple GCMs and realization is taken before the RCM is run, it can be expected that the downscaled output carries little bias. As can be seen in Fig. 2.9, the projections of future annual average near-surface air temperature for the grid near Tokyo differ by up to 5 °C among different GCMs. Even in direct downscaling method, it is unlikely that these projections can be inputted directly to RCMs without any bias correction because a 5 °C difference in mean temperature can lead to a completely different climate regime. On the contrary, after applying the PGW method (in other words, moving these projections close to the observed historical value), we can see that while the models disagree about the exact value of the quantity in question, they almost agree in the trend and amplitude of the variability of the quantity. By ensemble averaging the projection of all five models, we get a very smooth (and possibly closest-to-the-mean) projection of the future of the quantity. In addition to the bias-reduction benefit, computational cost is also greatly reduced by applying the PGW method.

In terms of disadvantages of PGW method, because the future simulation is essentially the present simulation with some well-averaged modifications of the temperature, pressure, and wind field, PGW method cannot capture large-scale intra- and inter-annual variability (for example, changes in frequency of El Niño). In other words, PGW method is unapplicable to answer questions about meteorological events whose frequency will change because of climate change because by the nature of the PGW simulation configuration, forcing inputted to the past/present and the future simulations has nearly identical (horizontal) spectra. In addition, in contrast to the direct downscaling method, it is not straightforward to see or prove the logical soundness of the PGW method. However, in practice, it has been shown that except for the aforementioned unapplicable cases, simulations using PGW method produced nearly identical output with the ones using direct downscaling (Brogli et al., 2023; Yoshikane et al., 2012). The PGW method is now widely use to evaluate the impact of warming on change in precipitation, temperature, snow under a warmer climate (Hara et al., 2008; Schär et al., 1996; Yoshikane et al., 2012), change in intensity of events (for example, heavy rain, cyclone) if they repeat in the future (Jyoteeshkumar Reddy et al., 2021; Taniguchi & Sho, 2015), and change in frequency of extreme precipitation (Doan et al., 2022). The last example may sound contradictory to the aforementioned inapplicability of the PGW methods but it is not the case. Under a warmer climate, it can be expected that there will be more water vapor in the atmosphere and non-extreme present rainfall may become extreme under that warmer climate. For that reason, the PGW method can still be applied to investigate possible change in frequency of extreme events under the assumption that there is no regime shift in the climatological forcing. Therefore, the PGW method is suitable for *narration* or *story-telling* of climate change (Brogli et al., 2023) in the sense that it is possible to compare a past event with its counterpart in a hypothesized climate and evaluate changes in the event's impact.

In the comparison between direct downscaling method and PGW method, it should also be noted that even though the PGW method has the word "pseudo" in its name, it does not mean that the PGW method is less real than the direct downscaling method. In the direct downscaling method, even though the output of GCMs obtained by running a long simulation from the past to the future are used as external forcing for RCM, there is no absolute guarantee that the future of the Earth system will match what the GCMs predict. As mentioned before in the analysis of Figs. 2.8 and 2.9, when in come to local climate, discrepancies among GCMs and between GCMs and observation are huge. On the other hand, while the process of creating "future" reanalysis data for RCM simulation in the PGW method is quite artificial, the "future" reanalysis data is not totally unreal because it is based on past and present reanalysis data which is derived from observation of phenomena that have actually happened on Earth. Therefore, once again, the PGW method is suitable for assessing how a past event will look like in the future (Brogli et al., 2023). From all the above analysis, the bottom line is that, there is no decisive factor that make the direct downscaling method superior to the PGW method or vice versa.

Chapter **3**

Construction of Supporting Datasets

In urban surface models, there are several commonly used parameters as discussed in Section 2.3. One highlight of this research is the input of global urban anthropogenic heat map and urban morphological parameters map (average building height H_{avg}, plan area index λ_p, frontal area index λ_f, roughness length for momentum z_0, and zero-plane displacement height d) to the Weather Research and Forecast (WRF) model for urban climate modeling. While all of these parameters are measurable, existing observation network and campaign are not enough to create a global dataset of these parameters derived purely from observation. Therefore, previous researchers have developed (semi-)empirical methods to construct global database of these parameters (Dong et al., 2017; Kawano, 2018; Khanh, 2019; Kiyomoto, 2018; Varquez et al., 2017, 2021). This dissertation inherits the results of those studies for its urban climate study. While the focus of this dissertation is not on the construction of these database, this chapter is dedicated to summarizing the methodology of the previous studies so that future studies can quickly utilize the methodology when handling new socioeconomic scenarios. The procedure summarized in this chapter can be applied to any socioeconomic scenarios. However, this dissertation used only the dataset constructed for the SSP3 and RCP8.5 scenarios under CMIP5.

3.1 Adjustment Population Map Using Nighttime Lights

LandScan™ Global population dataset estimates ambient (that is, 24-hour average) population at 30 arc-second spatial resolution. The dataset was found to mainly indicate population of residential areas. Using this population directly to estimate urban morphological parameters and anthropogenic heat may lead to underestimation for commercial areas where ambient population is low. For that reason, nighttime lights, which has higher intensity at commercial areas, were used to adjust the population map before the calculation of urban morphological parameters and anthropogenic heat.

Specifically, Visible Infrared Imaging Radiometer Suite (VIIRS) nighttime lights (Elvidge et al., 2017) was used. The data is available monthly. Average radiance composite images (v1) from the VIIRS Day/Night Band from the period January 2014 to March 2016 were resampled using spatial averaging to the resolution of LandScan™. Ensemble average (specifically, 20 % trimmed mean, that is, mean after discarding the lowest 20 % and the highest 20 %) of the images were then

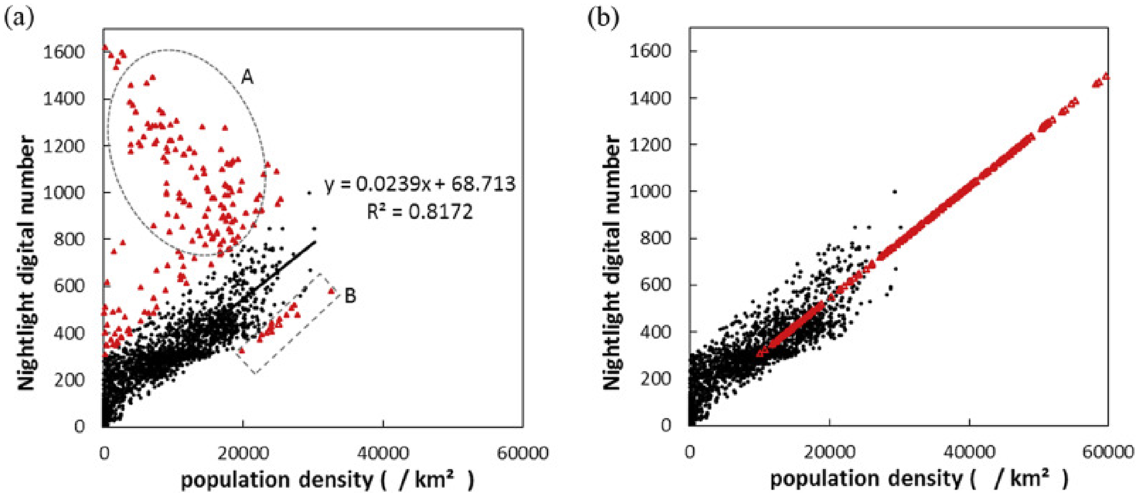

Figure 3.1: Concept of population density adjustment by nighttime lights. Red outliers are adjusted to follow the solid black regression line. Only outliers with nighttime lights above a certain threshold (300 in this case) is subjected to for adjustment. Note that the nighttime lights dataset used here is not VIIRS but the Global Radiance Calibrated Nighttime Lights dataset. (a) Before adjustment. (b) After adjustment. (Source: Dong et al., 2017. © The Authors. Used under CC BY-NC-ND 4.0.)

taken to produce a single nighttime lights dataset (hereinafter, nVIIRS). nVIIRS ($\mathrm{nW\,cm^{-2}\,sr^{-1}}$) is expected to capture the general nighttime lights condition.

nVIIRS was then used to adjust the population density information calculated from LandScan™. The concept of this process is shown in Fig. 3.1. In short, grids with nighttime lights disproportionate to the population density are considered outliers. The population density of these outlier grids are adjusted by using a linearly regressed function fit to the non-outlier grids' data. The detail steps are as follows.

1. Estimate a linear regression curve between both datasets within the same country boundary.
2. Using the Tukey's method, detect outliers and calculate a second linear regression from the non-outliers.
3. Population value at the outlier grids having nighttime light intensity above a certain threshold (nighttime lights threshold) are replaced with a new population value calculated using the second linear regression. However, adjustment is not applied if the adjusted population exceeds 2.5 times the maximum of pre-adjusted population density of all grids in the country.
4. Repeat the process for all grids and countries.

The nighttime lights threshold was imposed to prevent over adjustment outside of commercialized cities and to avoid the blooming effect of nighttime lights, For each country, the nighttime lights threshold was set to be $50\,\mathrm{nW\,cm^{-2}\,sr^{-1}}$ (empirical value) or the 99.9th percentile of all nVIIRS grids belong to that country, whichever is bigger. For the US, the threshold is fixed empirically to $120\,\mathrm{nW\,cm^{-2}\,sr^{-1}}$. This approach of using percentile to set threshold allows consideration of inter-country differences.

3.2 Projection of Future Population

To estimate a 1 km future distribution of AHE, a 1 km spatial projection of population density for a specified period is needed. Its projections must also be consistent with the known total projections for each country (available from the SSP database). Distributed population projection was achieved using two steps.

1. Extract 1 km urbanization probability for the future from a global urban growing projection dataset.

2. Construct a model to downscale the country-level population projection into 1 km grids using the projected urbanization probability and present population density distribution.

Specifically, GUGPS—a 30-arc-second spatial resolution global urban sprawling map (Zhou et al., 2019)—was used as projection of future urban growth. The GUGPS map was created using the SLEUTH model. For each year in the future, each grid has an integer probability value describing its likelihood to be urbanized. It is assumed that the urbanization probability of each grid correlates with the grid's population growth rate.

To predict the distribution of future population density, a discretized form of the logistic model (Morisita, 1965) was implemented for each grid of the same country as follows,

$$P_{i,j}^{n+1} = \frac{\left(A_{i,j}^{n} + 1\right) P_{i,j}^{n}}{1 + B_{i,j}^{n} P_{i,j}^{n}} \tag{3.1}$$

$$A_{i,j}^{n} = \exp\left(r_{i,j}^{n}\right) - 1 \tag{3.2}$$

$$B_{i,j}^{n} = \frac{A_{i,j}^{n}}{K^{n}} \tag{3.3}$$

where P refers to the population; n, i, and j refers to the year (discrete), longitudinal, and latitudinal coordinates, respectively. Parameters r and K are the natural population growth and the limiting values for population growth for each grid, respectively. K was set to the maximum population density value of all grids within the same country for the year 2013. On the other hand, r was assumed to be a linear function of the urbanization probability $f_{i,j}^{n}$ outputted from SLEUTH using the following equations,

$$r_{i,j}^{n} = \begin{cases} a^{n} f_{i,j}^{n+1}, & 0 < f_{i,j}^{n} < 100, \\ b^{n} f_{i,j}^{n+1}, & 100 \leq f_{i,j}^{n}. \end{cases} \tag{3.4}$$

where a and b are country-varying internal parameters for future years obtained by minimizing the root-square difference of the country-level total estimated $P_{i,j}^{n}$ for $n = 2001$ (starting period), 2006, 2009, 2010, 2012 and their corresponding real values taken from LandScan™. An additional constraint for the minimization was also set such that the absolute percentage error between the country-level total of estimated $P_{i,j}^{n}$ and those from the SSP dataset should not exceed 1 %. a and b were then recalculated for every decadal interval (i.e. a and b were set to the same value from the period 2041 to 2050). In terms of an optimization problem, it can be written as

$$\begin{aligned} &\underset{a^n,b^n}{\text{minimize}} && \sum_{\substack{y\in Y\\(i,j)\in C}} \left(P^y_{i,j} - P^{y,\text{LandScan}}_{i,j}\right)^2 \\ &\text{subject to} && \left|\sum_{(i,j)\in C} P^n_{i,j} - P^{\text{SSPDB}}_C\right| \Big/ P^{\text{SSPDB}}_C \le 1\,\%, \end{aligned} \tag{3.5}$$

where

- $Y = \{2001, 2006, 2009, 2010, 2012\}$ is the set of constraining years,
- C is a set of coordinates of grids belonging to a target country,
- P^{SSPDB}_C is the population of country C as projected in the SSP Database.

One exception to Eq. (3.1) is that, unpopulated grids ($P^n_{i,j} = 0$) that will be affected by urban sprawl ($f^{n+1}_{i,j} > 0$) was initialized with a $P^{n+1}_{i,j}$ value of 10.

Finally, adjustment of the population map by nighttime lights (Section 3.1) were performed. No future prediction of nighttime lights was conducted and the present nighttime lights dataset was used because of two reasons: (1) It is uncertain how country-level indicators from SSP and urban sprawl quantitatively relate with nighttime lights intensity. (2) Nighttime lights were mainly used to adjust the population distribution to have more representation in commercial areas which are assumed to not change up to the target future period.

3.3 Construction of Global Anthropogenic Heat Database

For each country, the total primary energy supply (TPES, symbol E_p, unit J) can be broken down into total final energy consumption (TFEC) and energy loss. TFEC can be broken down further to industrial and agriculture (IA) sector and commercial, residential, and transport (CRT) sector. Let the ratio of IA sector energy consumption, CRT sector energy consumption, and the energy loss within the TPES be R_{IA}, R_{CRT}, and R_L ($R_{IA} + R_{CRT} + R_L = 1$), respectively. It is assumed that all TPES will eventually be released to the atmosphere in the form of anthropogenic heat. Therefore, the term anthropogenic heat and energy consumption will be used interchangeably. First, TPES for each country must be obtained. Next, in order to build an hourly, monthly, spatially varying anthropogenic heat database, TPES must be broken down to each grid, each month, and each hour. Detail procedures are summarized in the following sections. Input datasets needed to construct the anthropogenic heat database are listed in Table 3.1.

3.3.1 Total Primary Energy Supply

The total primary energy supply (TPES) for each country is estimated using data from the SSP database released by the International Institute of Applied Systems Analysis (IIASA). Within the database, there are variations among different models (AIM, GCAM4, IMAGE, and MESSAGE), thus, ensemble average was taken. Two parameters were used to estimate E_p for each country.

Table 3.1: Input dataset for constructing the anthropogenic heat database for the present and the future. Hyphen (-) in the Future column indicates that the corresponding parameter is assumed to be the same as the present.

	Present	Future	Resolution
GDP	SSP database	SSP database	Country
TPEC	SSP database	SSP database	Region
Energy intensity	World Bank (2010 data)	-	Country
Energy balances	IEA	-	Country
Nighttime lights	VIIRS DNB Nighttime Lights	-	30 arc-second
Combustion sources	VIIRS Nightfire version 3.0 (Gravite)	-	Discrete
Population	LandScan™ 2013	Future projection	30 arc-second
Air temperature	NCEP/NCAR Reanalysis (2012 data)	CMIP5 database	Varying

1. Regional TPES (in other words, TPES of a economical region, consisting of multiple countries).

2. Country energy intensity m (TJ per US\$2011), which relates the energy consumption of a country to its GDP. Higher m means that more energy is needed to produce a unit of GDP.

From the two variables, regional TPES $E_{p,r}$ was broken down to country TPES $E_{p,c}$ by using country energy intensity as the weighting factor.

$$E_{p,c}^{y,SSP} = E_{p,r}^{y,SSP} \times m_c^{2010} GDP_c^y \Big/ \sum_{c \in r} m_c^{2010} GDP_c^y \,, \tag{3.6}$$

where y, c, r and SSP are year, country, region, and SSP scenario, respectively. Equation (3.6) uses 2010 energy intensity because there was negligible changes in energy intensity from 2010 to 2015 (Varquez et al., 2021). It is also assumed that the energy intensity will remain the same for the future projection.

3.3.2 Spatial Distribution of Total Energy Consumption

For each country, TPES must now be distributed spatially to all grids of the country. The annual average anthropogenic heat Q_{f-y} of a grid is considered to be

$$Q_{f-y} = Q_L + Q_{CRT} + Q_{IA} + Q_M + Q_{point}, \tag{3.7}$$

where

- Q_L is contribution of energy loss,
- Q_{CRT} is contribution of the CRT sector,
- Q_{IA} is contribution of the IA sector,
- Q_M is contribution of human metabolism (not a part of TPES),

- Q_{point} is contribution of point sources.

The total contribution of all point sources is set to be 10 % of TFEC. The reason of this attribution is based on previous research (Ichinose et al., 1999; Lee et al., 2009). Then, the contribution of point sources in a grid can be written as

$$R_{point} = 0.1(R_{CRT} + R_{IA}), \tag{3.8}$$

$$Q_{point,i,j} = R_{point} \times \frac{E_p}{T} \times \frac{d_{i,j}}{A_{i,j} \sum d_{i,j}}, \tag{3.9}$$

where

- $A_{i,j}$ is the area (in m^2) of the grid,
- T is the number of seconds in one year (that is, $365 \times 24 \times 60 \times 60$)
- $d_{i,j}$ is the weighting factor to distribute the total contribution of point sources to each grid which is discussed in detail in Section 3.3.5.

The contribution of energy loss and the IA sector is distributed to each grid as below.

$$s = R_L/(R_L + R_{IA}), \tag{3.10}$$

$$Q_{L,i,j} = \left(R_L - sR_{point}\right) \times \frac{E_p}{T} \times \frac{1}{\sum A_{i,j}}, \tag{3.11}$$

$$Q_{IA,i,j} = \left(R_{IA} - (1-s)R_{point}\right) \times \frac{E_p}{T} \times \frac{A'_{i,j}}{A_{i,j} \sum A'_{i,j}}, \tag{3.12}$$

where

- s is a factor to distribute the contribution of point sources between the energy loss and the IA sector energy consumption. This is to account for the fact that point sources can appear in both energy loss and the IA sector. For example, both steel mills and power plants are point sources. However, while energy consumption of steel mills appears in the IA sector, loss during power generation of power plants appears in the energy loss.
- $A'_{i,j}$ is equal to $A_{i,j}$ if the grid is populated and to 0 if the grid is unpopulated.

As can be inferred from the equations, energy loss is distributed equally to all grids within a country; however, energy from the IA sector is distributed equally to populated grids only.

The contribution of the CRT sector is distributed as follow.

$$Q_{CRT,i,j} = R_{CRT} \times \frac{E_p}{T} \times \frac{P_{d,i,j}}{A_{i,j} \sum P_{d,i,j}}, \tag{3.13}$$

where $P_{d,i,j}$ is the nighttime lights adjusted population density of the grid. From the equation, it can be inferred that energy from the CRT sector is distributed based on population density.

Human metabolism is considered to be a function of population density.

$$Q_{M,i,j} = P_{d,i,j} \times H_M, \tag{3.14}$$

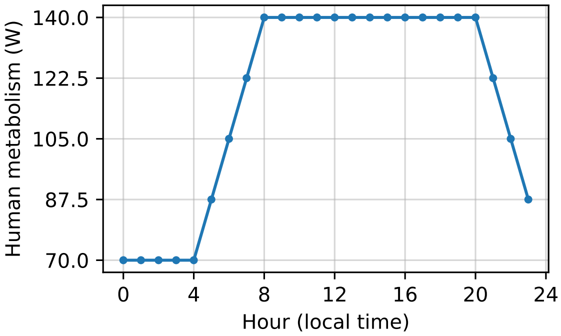

Figure 3.2: Variation of human metabolism (H_M) in a day plotted based on the explanation of Dong et al. (2017).

where H_M is the metabolism (in W) of a person. Dong et al. (2017) assumed, following a US data (Sailor et al., 2015), that H_M is 70 W during nighttime and 140 W during daytime and has a 5-hour linear transition between daytime and nighttime (Fig. 3.2).

3.3.3 Monthly Distribution of Anthropogenic Heat

The annual average anthropogenic heat of each grid must be now distributed to each month. The general formulation is that the monthly average anthropogenic heat Q_{f-m} is

$$Q_{f-m} = Q_{f-y} \times \beta_m, \tag{3.15}$$

where β_m is a weighting factor for the month m defined as the following.

$$\alpha_m = |T_m - 20| f_s + 1, \tag{3.16}$$

$$\beta_m = \frac{\alpha_m}{\sum \alpha_m / 12}, \tag{3.17}$$

where

- f_s is a sensitivity function which will be discussed below,

- T_m is the month average temperature in °C.

The equations assume that energy usage is lowest when the monthly average is 20 °C.

Regarding the sensitivity, energy usage is known to be sensitive to temperature. From energy usage data for US, Japanese cities, and London, two empirical equations for f_s was obtained for warm months and for cool months (Dong et al., 2017).

$$f_s = \begin{cases} f_{s-w}, & T_m > 20\,^{\circ}\mathrm{C}, \\ f_{s-c}, & \text{otherwise}, \end{cases} \tag{3.18}$$

$$f_{s-w} = \begin{cases} 0.3, & T_y < 10\,^{\circ}\mathrm{C}, \\ 0.002T_y^2 + 0.062T_y - 0.4495, & 10\,^{\circ}\mathrm{C} \leq T_y < 27\,^{\circ}\mathrm{C}, \\ 2.8, & \text{otherwise}, \end{cases} \tag{3.19}$$

$$f_{s-c} = \begin{cases} 2.8, & T_y < 10\,^{\circ}\mathrm{C}, \\ -0.0063T_y^2 + 0.1063T_y + 2.2806, & 10\,^{\circ}\mathrm{C} \leq T_y < 27\,^{\circ}\mathrm{C}, \\ 0.3, & \text{otherwise}, \end{cases} \tag{3.20}$$

where T_y is the annual average temperature.

3.3.4 Hourly Distribution of Anthropogenic Heat

Similar to the break down from annual anthropogenic heat to monthly anthropogenic heat, the break down from monthly anthropogenic heat to hourly anthropogenic heat is achieved by using a weighting factor.

$$Q_{f-h} = Q_{f-m} \times \gamma_h, \tag{3.21}$$

where γ_h is the weighting factor for the hour h. Four groups of diurnal variation of AHE was derived from the Tokyo bottom-up weekday AHE dataset of Moriwaki et al. (2008) as shown in Fig. 3.3.

3.3.5 Detection of High Heat-Emission Point Sources

There are several locations with very high anthropogenic heat emission without having neither high population density nor high nighttime lights (e.g., manufacturing and power plants). These locations are called point sources. Anthropogenic heat cannot be adequately distributed to these point sources using only the population density adjusted by nighttime lights dataset (Section 3.1). Therefore, some techniques are employed to detect point sources.

VIIRS-Nightfire is a product of VIIRS which contains information regarding the day-to-day location of detected combustion sources. Data for the period from December 2017 to February 2018 of Version 3.0 (GRAVITE) of the VIIRS-Nightfire was used. Close-to-permanent combustion sources was detected by the following procedure.

1. The geographical location (longitude and latitude) of the combustion sources are mapped onto a 30-arc-second gridded map.
2. The number of days $d_{i,j}$ each gridded is detected to contain a combustion source is counted. $d_{i,j}$ is used in Eq. (3.9) to distribute the total contribution of point sources to each grid.
3. Grids with no more than 3 days of detected combustion is discarded (in other words, $d_{i,j}$ is set to 0 if $d_{i,j} \leq 3$) because they are considered to have temporary combustion events (e.g., biomass burning, moving heat sources, fire incidents).

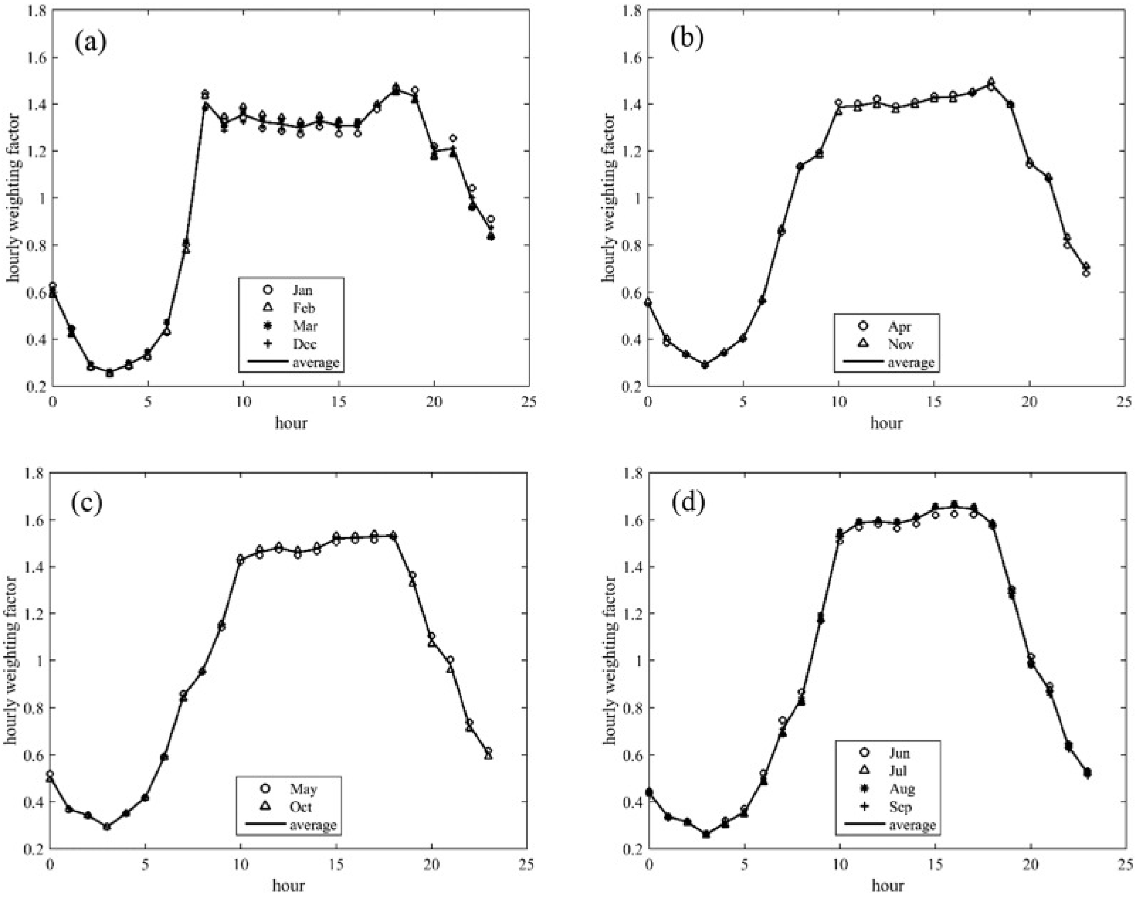

Figure 3.3: Hourly weighting factor of anthropogenic heat for each hour of the day in local time. Patterns are chosen based the monthly average temperature. (a) $T_m < 12.4$ °C, (b) 12.4 °C $\leq T_m <$ 16.95 °C, (b) 16.95 °C $\leq T_m <$ 20.95 °C, (d) $T_m \geq$ 20.95 °C. (Source: Dong et al., 2017. © The Authors. Used under CC BY-NC-ND 4.0.)

3.4 Construction of Urban Morphological Parameters

In this section, if there is no further explanation, population refers to population adjusted by nighttime lights (see Section 3.1).

3.4.1 Construction of Intermediate Datasets

Construction of Country Level GDP per Capita Dataset

Past data and future projections of country level GDP in 2005 US dollar and country population under different Shared Socioeconomic Pathways (SSPs) were extracted from SSP database version 2. As for the GDP, the projections by the Organization for Economic Co-operation and Development (OECD) and the International Institute for Applied Systems Analysis (IIASA) was used. For both future GDP and population, projections for SSP3 was used (C. & Lutz, 2017; Cuaresma, 2017; Dellink et al., 2017; Riahi et al., 2017).

Because the database includes many projected values by many models, the ensemble mean of

$$\begin{tikzcd}
\text{GDP} \arrow[r] \arrow[dr] & H_{\text{avg}} \arrow[r] \arrow[dr] & d \\
\text{Population} \arrow[r] \arrow[ur] & \lambda_p \arrow[r] \arrow[ur] \arrow[dr] & z_0 \\
 & & \lambda_f \arrow[u]
\end{tikzcd}$$

Figure 3.4: Dependency between the urban morphological parameters.

projected values among all models were taken as future GDP and population projections for each country. Based on these information, country level GDP per capita was calculated and a gridded dataset in which each grid cell contains the GDP per capita of the corresponding country was constructed.

Construction of Gridded Administrative Division Level Population Dataset

From gridded population density dataset and first-level administrative division boundary dataset (included in LandScan 2013™ dataset), a gridded dataset regarding population and population density of administrative divisions was constructed. Even though the definition of first-level administrative division varies from country to country (for example, prefecture in Japan, state in the United States and India, province in Vietnam), for the sake of simplicity, hereinafter, first-level administrative division is referred to as city. Each grid cell contains the following information about the corresponding city:

- Total population,
- Maximum population density,
- Normalized population density (*RPD*) defined as the ratio between population density of the grid and maximum population density among all the grids the city.

3.4.2 Construction of Global Urban Parameters Dataset

A gridded dataset of average building height (H_{avg}), plan area index (λ_p), frontal area index (λ_f), roughness length (z_0) and zero-plane displacement height (d) was constructed. The linkage between the parameters are summarized in Fig. 3.4.

The following modified version of empirical equations for estimating H_{avg} and λ_p proposed by Varquez et al. (2017) were used

$$\alpha_{H_{\text{avg}}} = 2 \times 10^{-11} \times GRDP_{\text{city}} + 9.80 \tag{3.22a}$$

$$\beta_{H_{\text{avg}}} = -2 \times 10^{-12} \times GRDP_{\text{city}} + 9.18 \tag{3.22b}$$

$$H_{\text{avg}} = \alpha_{H_{\text{avg}}} \times RPD + \beta_{H_{\text{avg}}} \tag{3.22c}$$

where *RPD* represent gridded normalized population density (defined in Section 3.4.1) and city GRDP (Gross Regional Domestic Product) ($GRDP_{\text{city}}$) is estimated as

$$GRDP_{\text{city}} = GDPPC_{\text{country}} \times P_{\text{city}} \tag{3.23}$$

where $GDPPC_{\text{country}}$ and P_{city} are country level GDP per capita and total population of city, respectively. The underlying assumption of Eq. (3.23) is that the city GRDP varies linearly with its population.

λ_p is estimated as

$$\lambda_p = -0.2532 \times RPD^2 + 0.4562 \times RPD + 0.1125. \tag{3.24}$$

Equation (3.24) is a parabola with the maximum of 0.318 at $RPD_0 = 0.90$. Under the assumption that an area with higher population density has higher λ_p than an area with lower population density, λ_p for an area with $RPD > RPD_0$ were estimated to be the λ_p at RPD_0.

λ_f was estimated from λ_p by the following equation proposed by Kanda et al. (2013):

$$\lambda_f = 1.42\lambda_p^2 + 0.4\lambda_p \qquad (0.05 < \lambda_p < 0.45) \tag{3.25}$$

Zero-plane displacement height d was estimated using the following equations proposed by Kanda et al. (2013):

$$\sigma_H = 1.05H_{\text{avg}} - 3.7 \tag{3.26a}$$

$$H_{\text{max}} = 12.51\sigma_H^{0.77} \tag{3.26b}$$

$$X = \frac{\sigma_H + H_{\text{avg}}}{H_{\text{max}}} \qquad (0 \le X \le 1) \tag{3.26c}$$

$$\frac{d}{H_{\text{max}}} = -0.17X^2 + \left(1.29\lambda_p^{0.36} + 0.17\right)X \tag{3.26d}$$

where σ_H and H_{max} are standard deviation of building height and maximum building height, respectively.

Roughness length z_0 was estimated using the following equations proposed by Kanda et al. (2013):

$$Y = \frac{\lambda_p \sigma_H}{H_{\text{avg}}} \qquad (Y \ge 0) \tag{3.27a}$$

$$\frac{z_0}{z_{0,\text{mac}}} = 20.21Y^2 - 0.77Y + 0.71 \tag{3.27b}$$

where $z_{0,\text{mac}}$ is estimated roughness length obtained from Macdonald equations (Macdonald et al., 1998):

$$\frac{d_{\text{mac}}}{H_{\text{avg}}} = 1 + A^{-\lambda_p}(\lambda_p - 1) \tag{3.28a}$$

$$\frac{z_{0,\text{mac}}}{H_{\text{avg}}} = \left(1 - \frac{d_{\text{mac}}}{H_{\text{avg}}}\right) \exp\left(-\left(0.5\beta\frac{C_D}{\kappa^2}\left(1 - \frac{d_{\text{mac}}}{H_{\text{avg}}}\right)\lambda_f\right)^{-0.5}\right) \tag{3.28b}$$

in which $A = 4.43$, $\beta = 1.0$, $C_D = 1.2$ is the nominal drag coefficient of a cubical obstacle and $\kappa = 0.4$ is the von Kármán constant.

3.4.3 Post-Processing

Firstly, urban parameters for all grids with population density lower than 2000 people/km^2 as non-urban area were set to zero.

Secondly, due to decreasing population, urban parameters for certain areas in 2050 were estimated to be lower than that of 2010. However, this study assumed that even with decreasing population, there would be no large-scale demolition of buildings causing decrease in urban parameters. Consequently, if a particular urban parameter for a grid cell in 2050 was estimated to be lower than that in 2010, the value of 2010 was used instead.

3.5 Chapter Summary

In this chapter, the methodology established by previous studies to construct global present and future population density, anthropogenic heat, and urban morphological database was summarized. The information in this chapter can be used by future study to adjust the database to other socioeconomic scenarios and pathways. The constructed parameter database will be used in the following chapters for projecting the future climate of megacities.

CHAPTER 4

Future Climate of Megacities: Summer Month Case Study

4.1 Introduction

As mentioned before, there have been attempts to project future climate for individual cities around the world (Adachi et al., 2012; Argüeso et al., 2014; Doan et al., 2016). These studies focused on individual cities, some utilized locally available datasets such as land-use dataset (Argüeso et al., 2014) and master plan for future urbanization (Doan et al., 2016). Furthermore, spatial distribution of futuristic projections of urban morphological parameters were not considered in many cases. Studies focused on cities in developing countries are still rare even though urbanization is progressing rapidly in developing countries. The drawbacks of the past research became the research gaps that this study attempts to fill in.

The study of Darmanto et al. (2019), while focused only on a single city, proposed a framework that relies solely on publicly available global datasets, and therefore can be flexibly extended to any region of interest. The purpose of this chapter is to modify and scale that approach to project future climate for the world's 43 megacities simultaneously at high resolution using publicly available global datasets. Target for numerical simulation is the mean climate condition in August in the 2006–2015 period and the 2046–2055 period. For most megacities, August is a summer month, which explains the title of this chapter. However, for a few megacities at mid- and high-latitude in the Southern Hemisphere, August is a winter month.

The objective of this chapter is to

- verify the feasibility of our approach in simulating decade mean temperature for many cities simultaneously,
- quantify the effect of urbanization on air temperature change at different spatial scale,
- investigate the effect of urbanization in non-urban areas surrounding urban areas.

A part of this chapter was published in scientific journals (Khanh et al., 2020, 2023a).

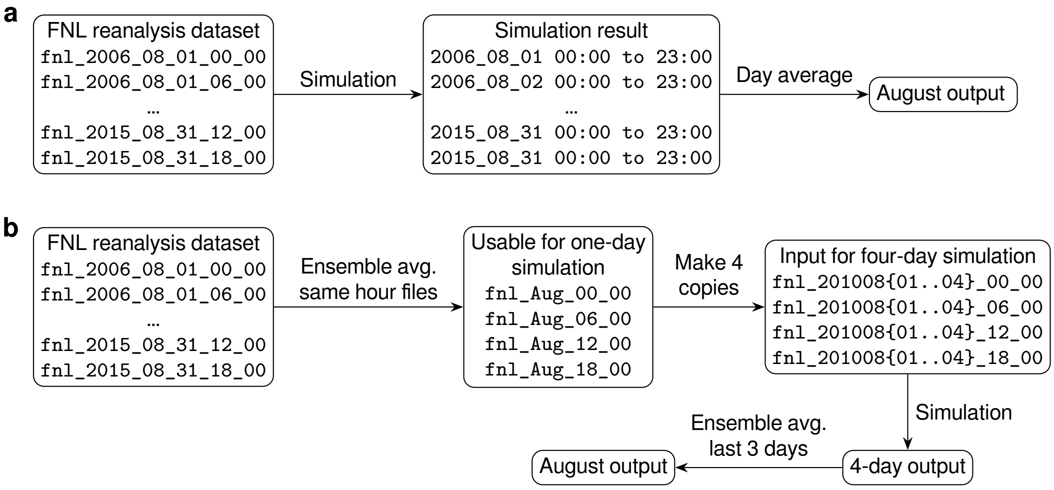

Figure 4.1: Simulation methods to obtain decadal average August climate. (a) The direct method. (b) The method used in this study.

4.2 Methodology

4.2.1 Meteorological Input

To know the average weather condition in a city in a certain month through out the present period (2006–2015), a conventional method is to run a 10-year simulation and then ensemble average the output data by month. However, this method (average after simulation, see Fig. 4.1(a)) is computationally expensive, thus, we attempted to use a cheaper method (simulation after average, see Fig. 4.1(b)). We explain in detail the process of obtaining the average weather condition for August over 2016–2015 period. The process for other months of the year is similar. First, we downloaded the National Centers for Environmental Prediction (NCEP) Final Operational Global Analysis (FNL) dataset for all hours and all days in January in the 2006–2015 period. Next, for each available hour of the day (00, 06, 12, and 18 UTC), we ensemble averaged all the FNL files of that hour in all Januaries of the decade. This operation resulted in a set of four meteorological input files which is enough for a one-day simulation. We regard this one day as a typical August day of the decade. We then assumed that this typical day repeats for four consecutive days and made four copies of the four meteorological input files so that we could run a four-day simulation. The first day of simulation was for model spin-up and its output was discarded. The remaining three-day simulation output was ensemble averaged to a one-day output which was used for further analysis. This method was tested in previous studies (Narita et al., 2019; Varquez et al., 2018). Practically, this method drastically reduce computational resources necessary to obtain decadal average temperature. Instead of running ten years of simulation, only four days of simulation is required. The rationale of this method can be summarized in the following points.

- By ensemble averaging the 10-year-long reanalysis dataset for a particular month, it can be expected that all extreme events (for example, heatwaves, typhoons, cold spells) happened in those months will have negligible influence and the actual representative climatological and meteorological feature of that month at that location can be obtained.

- Numerical weather models are essentially numerical partial differential equation (PDE) solvers. Numerical models, in general, favor smooth and well-behaved functions over difficult ones. It can be reasonably expected that if numerical models can simulate day-to-day weather at an acceptable accuracy/precision, it can also handle the much smoother and well-behaved the ensemble average input.

Meteorological input for simulation of future scenarios was constructed using the pseudo-global warming (PGW) method using the RCP8.5 run of five General Circulation Model (GCM) members (GFDL-ESM2M, IPSL-CM5A-LR, MIROC-ESM-CHEM, HadGEM2-ES, and NorESM1-M) of the Coupled Model Intercomparison Project phase 5 (CMIP5) were used. Details about the PGW method can be found in Chapter 2.

4.2.2 Urban Surface Boundary Consideration

For the present climate simulation, population density adjusted by nighttime lights were used to modify the MODIS land cover type dataset (included by default in the WRF model) to put more emphasis on urban land use. For the present simulation, all MODIS grids with the population count of at least 1000 are assigned to urban category. For the future simulation, all MODIS grids with the population density of at least 1000 per km^2 are assigned to urban category. Distributed urban morphological parameters and hourly varying global anthropogenic heat flux map was used. For the future climate simulation, population density was projected by combining a logistic model with a global urban sprawling map. Urban morphological parameters and anthropogenic heat flux map were calculated by the same method with the present case. Details of the construction of these parameters was discussed in detail in Chapter 3.

While this study does not attempt to attribute the change in temperature to each individual factor quantitatively, below, we discuss possible contributions of each factor qualitatively.

- Anthropogenic heat causes change in air temperature based on the law of thermodynamics. The effect of anthropogenic heat is known to be dependent on the season and the background climate (Varquez et al., 2018; L. Wang et al., 2023).

- Increase in roughness length for momentum z_0 slows down near-surface wind speed (Varquez et al., 2015; X. Wang et al., 2009).

- Zero-plane displacement height d impact is similar to the impact of changing topography. In the WRF model, d is added directly to the elevation as recommended (Kanda et al., 2013).

- Average building height H_{avg} affects canopy wind speed. The canopy wind speed is scaled down from the wind speed at the first model level. It increases with building height but decreases with roughness length. Therefore, H_{avg} can affect canopy wind speed, which will in turn affects heat transfer efficiency from canopy surfaces.

Table 4.1: Model setup

Domains	One-way nesting with a fine domain (2 km resolution) nested in a coarse domain (10 km resolution)
Sea surface temperature update	Disable
Adaptive time step	Enable
Microphysics	New Thompson et al. scheme
Longwave radiation	Rapid Radiative Transfer Model (RRTM) scheme
Shortwave radiation	Goddard shortwave
Surface layer	MM5 similarity
Land surface	Noah land surface model
Urban surface	Single layer urban canopy model with distributed urban morphological parameters
Planetary boundary layer	Mellor-Yamada Nakanishi and Nitto Level 2.5
Cumulus parameterization	Kain-Fritsch scheme for the coarse domain

- Plan area index λ_p and frontal area index λ_f are used to calculate the sky view factor (SVF) (Kanda et al., 2005). The relation between λ_p, λ_f and SVF is not monotonous. Increase in SVF allows more shortwave radiation to enter the canopy but also allows faster radiative cooling. SVF is also used to calculate view factors and energy exchange between different surfaces of the urban canopy with details explained in the original description of the urban canopy model (Kusaka et al., 2001). Because of these complex interactions, it cannot be conclude in one sentence if increase in λ_p and/or λ_f will cause increase/decrease in near-surface air temperature.

4.2.3 Model Configuration

A modified version of the WRF model v3.3.1 coupled with the single-layer urban canopy model was used (Kusaka & Kimura, 2004; Varquez et al., 2015). This modified version has improvements to consider spatial variations in urban morphological parameters. Performance of the model was verified in previous research (Darmanto et al., 2019; Varquez et al., 2015; Yucel et al., 2016). Compared to the original single-layer urban canopy model (Kusaka & Kimura, 2004) which handles three urban categories (low density residential, high density residential, and commercial), in this modified version, each urban grid is modeled by five morphological parameters: average building height (H_{avg}), plan area index (λ_p), frontal area index (λ_f), roughness length (z_0), and zero-plane displacement height (d). In addition, hourly spatially varying anthropogenic heat is emitted to the first atmospheric level and is not a part of the urban canopy model calculation. Detailed model setup is given in Table 4.1. The model code is available in GitHub (https://github.com/TokyoTechGUC/WRF-distributed-urban). The sensitivity of the urban canopy model to urban morphological parameters, in general, were confirmed in previous research (Z.-H. Wang et al., 2011). The sensitivity of this specific modification of the model to the change of urban morphological parameters, in particular, was also tested (Varquez, 2014). 41 set of domains were setup for 43 target cities Guangzhou and Shenzhen, Rio de Janeiro and Sao Paulo were grouped into two groups because

Table 4.2: Simulated scenarios.

Scenario	Urbanization	Climate forcing
Present	present	present
Intermediate	present	future
Future	future	future

Table 4.3: Root-mean-square error (RMSE, °C), bias (°C), standard error (SE, °C), and Pearson correlation coefficient (r) of simulated hourly 2 m air temperature. Note: $\text{RMSE}^2 = \text{Bias}^2 + \text{SE}^2$.

	RMSE	Bias	SE	r
Overall	2.01	0.98	1.76	0.96
Daytime	2.31	1.51	1.74	0.95
Nighttime	1.52	0.26	1.50	0.97
Individual cities	0.55 to 3.93	-2.11 to 3.58	0.54 to 2.56	0.81 to 0.99

of they are geographically close to each other. Each set of domain consists of a coarse domain and a fine domain with the resolutions of 10 km and 2 km respectively. The option of updating sea surface temperature at each input interval was turned off because of the short simulation period. The domains are listed in Appendix B.

4.2.4 Simulated Scenarios

We conducted simulation for three scenarios as summarized in Table 4.2. The present scenario is the basis for model verification and future projection. As for the future scenario, from the construction of input consisting of the global urban sprawling map assuming uncontrolled urban expansion, GDP and population growth projection under SSP3 characterized by high mitigation, adaptation challenges (Riahi et al., 2017), and highest emission forcing RCP8.5, we assume that the simulated future scenario represents the worst case scenario. There are also other studies using this coupling of SSP3 and RCP8.5 (Gao et al., 2024; Salam et al., 2017; M. Wang et al., 2020)

The intermediate scenario considers the change in climate forcing but does not take urbanization (urban sprawling and anthropogenic heat emission change) into consideration. This scenario is used to evaluate the impact of urbanization.

4.3 Results and Discussions

4.3.1 Verification of Simulated Present Climate Condition

The simulated present climate condition was compared against the ensemble of observation data. In detail, the simulated 2 m air temperature, which was available hourly, was compared against the ensemble of corresponding observations. Observations from world wide stations were obtained

Table 4.4: Mean and standard deviation of each domain's spatial mean of change in daily mean 2 m air temperature in intermediate scenario and future scenario with present scenario taken as the basis of comparison, and urbanization effect which is obtained by subtracting the change in intermediate scenario from the change in future scenario. Unit: °C.

Focus	Scenario		Urbanization effect
	Intermediate	Future	
Domain	1.79 ± 0.47	1.84 ± 0.49	0.05 ± 0.05
Old urban	1.82 ± 0.51	1.91 ± 0.51	0.09 ± 0.11
New urban	1.85 ± 0.50	2.13 ± 0.54	0.28 ± 0.13

from https://www.ogimet.com and only stations that reported data continuously in the 2006–2015 period were chosen. Refer to Appendix B for the number of stations available for each domain.

Validation result is summarized in Table 4.3. Overall, the model had a tendency to overestimate 2 m air temperature. However, comparing the bias in daytime and night time, it can be seen that the tendency was significantly stronger in daytime than in night time. At the level of individual cities, RMSEs and biases varied in larger ranges.

We concluded that the performance of the model in reproducing the present climate condition is adequate because of the following reasons:

- The meteorological input was not historical data but the ensemble of historical data,
- Differences are expected when comparing simulated temperature of a model grid which is spatial average with station data which is from point observation.
- Overall and in all breakdowns, Pearson correlation coefficient r indicated that simulated and observed 2 m air temperature were well-correlated,
- 76.1 % of simulated 2 m air temperature lay within one standard deviation of the corresponding observed value and 97.8 % lay within two standard deviations,
- Our approach relied solely on publicly available global input datasets with no adjustments made to adapt to any specific city.

We also concluded that the model is adequate for the following discussion about temperature change between the present and the future because the influence of the bias should be minimized in the difference, and for the discussion about urbanization effect because the effect arises from the difference in urban morphological parameters and urban land use between the intermediate and future scenario both of which have the same climate forcing.

4.3.2 Quantification of Urbanization Effect

Each domain's spatial mean of change in daily mean 2 m air temperature under different view points (whole domain, old urban, and new urban) is summarized in Table 4.4. Here we define an area

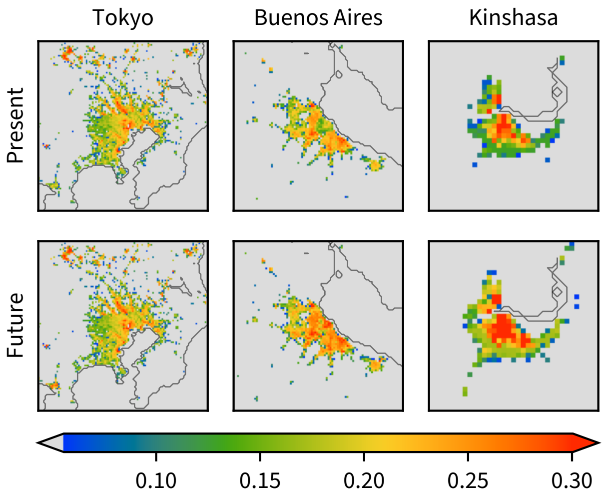

Figure 4.2: Plan area index (dimensionless) in the present and future scenario in some domains. Spatial scales are different and omitted.

(a) Daily minimum and maximum 2 m air temperature in the present and future scenarios

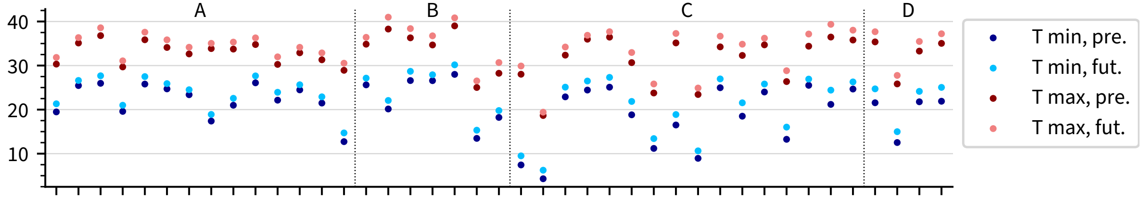

(b) Change in daily minimum and maximum 2 m air temperature between the present and future scenarios

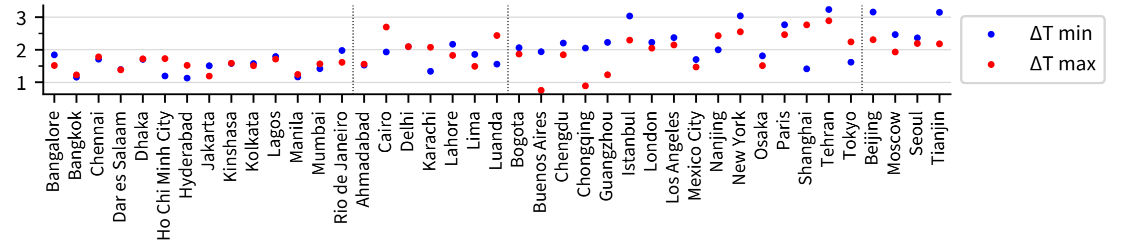

Figure 4.3: Spatial daily minimum and maximum 2 m air temperature in urban areas in August in the present and future scenarios, and their difference. Domains are grouped by Köppen climate classification (A: tropical, B: dry, C: temperate, D: continental) (Rubel & Kottek, 2010), domains in the same group are sorted in lexicographical order. Unit: °C.

Table 4.5: The time at which advected urbanization effect could be observed in local time.

Domain	Time range	Domain	Time range
Buenos Aires	8:00 to 9:00	Kinshasa	7:00 to 8:00
Dar es Salaam	18:00 to 8:00	Lagos	22:00 to 5:00
Karachi	15:00 to 5:00	Luanda	17:00 to 21:00

as *old urban* if it is an urban area in the present and as *new urban* if it is not an urban area in the present but it is an urban area in the future scenario. Note that *urban shrinking* or the replacement of an urban cover to a non-urban surface was not assumed in this study.

When looking at the whole domain (in other words, at a large scale), the effect of urbanization can still be observed, however, it is relatively insignificant compared to the global effects. This is because in each domain, urban area covers only (13.2 ± 10.5) % of the whole domain size. Even when all water bodies are excluded, the ratio is still only (17.2 ± 11.8) %.

Focusing on the old urban, the effects of urbanization becomes clearer with higher mean and also more variance than the whole domain. The large variance is due to the fact that the development in some old urban areas has been saturated (for example, Tokyo, Bangkok, and London) while it is still progressing rapidly in some others (for example, Dar es Salaam, Buenos Aires, and Kinshasa) as shown in Fig. 4.2.

The effect becomes clearest when looking at the new urban. The mean effect in the new urban is significantly higher than that in the whole domain and the old urban. The contribution of urbanization effect to the total temperature change in the new urban is (13.5 ± 5.9) %, which is not negligible. This clear effect is explainable by the fact that the formation of the new urban fundamentally changes the characteristics of land cover. Usually, the area of impermeable surface increases and vegetation fraction decreases. Consequently, there is less latent heat and more sensible heat, leading to the increase in air temperature.

Daily minimum and maximum temperature in urban areas in all domains in the present scenario, the future scenario and the difference between the two scenarios are summarized in Fig. 4.3. In 26 out of 41 domains, the increase in daily minimum temperature is higher than the increase in daily maximum temperature, implying a narrower diurnal temperature range (DTR) in the future. However, no correlation could be identified between present temperature statistics and change in DTR. In addition, the increase in daily maximum and minimum temperature is smallest in domains with tropical climate and highest in domains with continental climate. Further investigation is needed to understand mechanism of the difference between the increase of daily minimum temperature and that of daily maximum temperature, and the difference in the increase due to climate classification.

4.3.3 Wind and Urbanization Effect on Non-Urban Areas

By visually inspecting the two-dimensional distribution of urbanization effect and wind map, we found that in six domains (Luanda, Buenos Aires, Dar es Salaam, Karachi, Kinshasa, and Lagos), the effect of urbanization can be observed downwind. Specifically, going from the intermediate scenario

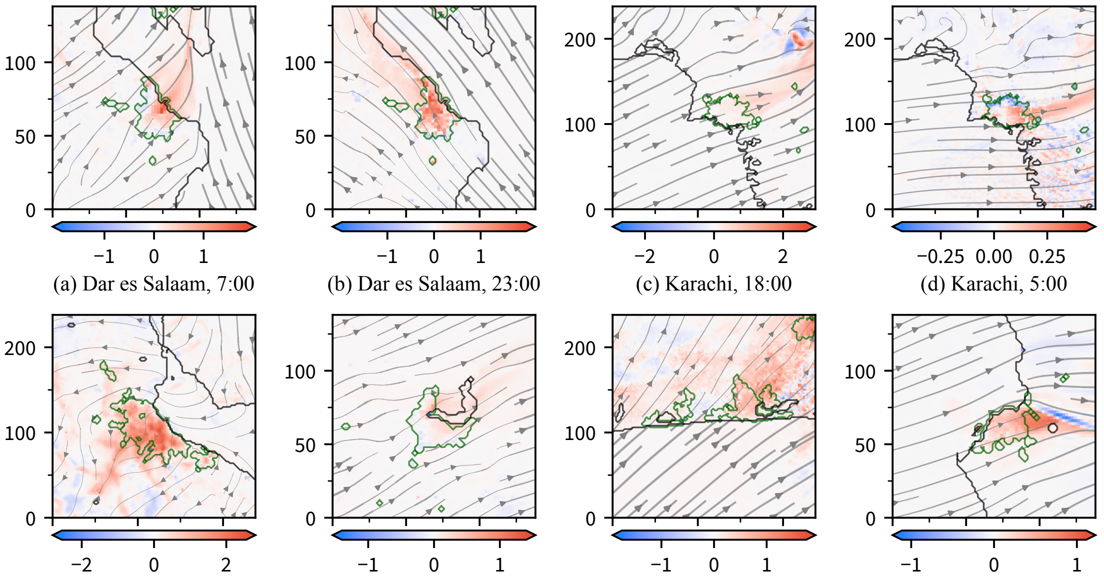

(a) Dar es Salaam, 7:00 (b) Dar es Salaam, 23:00 (c) Karachi, 18:00 (d) Karachi, 5:00

(e) Buenos Aires, 9:00 (f) Kinshasa, 7:00 (g) Lagos, 1:00 (h) Luanda, 17:00

Figure 4.4: Urbanization effect advected by wind in different domains at different time averaged throughout the simulation period. Coastline and inland water body boundary are depicted by black line. Urban area boundary is depicted by green line. The effect is measured in °C, the unit of horizontal and vertical axes is km, the time is local time. In each figure, the scales of the axes are the same.

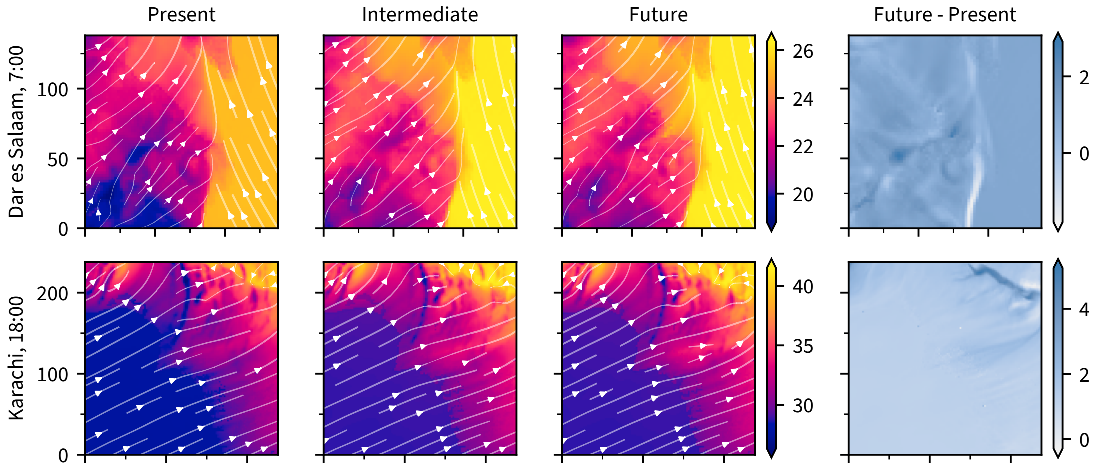

Figure 4.5: 2 m air temperature in Dar es Salaam at 7:00 and Karachi at 18:00 (local time) in the present, intermediate, and future scenario (averaged throughout the simulation period), and the difference between the present and the future scenario. The unit of temperature is °C, the unit of horizontal and vertical axes is km. In each figure, the scales of the axes are the same.

to the future scenario, increase in air temperature was observed in non-urban areas (including water body) downwind of urban areas. This increase should be due to the hot air advected from the urban areas upwind.

For example, in Dar es Salaam (Fig. 4.4(a) and (b)), the phenomenon was observed clearly from evening to sunrise. The long red tail did not originate from the surface directly beneath it because the tail changed with wind direction and it lay on the ocean while both urbanization expansion and increase in anthropogenic heat do not happen on the ocean and they have no dependency on wind direction. As depicted in the figure, the urbanization effect could be advected by the wind up to 60 km downwind.

Fig. 4.5 shows the air temperature in Dar es Salaam and Karachi in the present, intermediate, and future scenario at the time the phenomenon could be observed clearly. However, looking at these temperature maps, no discernible difference could be seen. The phenomenon could not be identified even when looking at the map of temperature difference between the present and the future scenario due to its high uniformity. This justifies the necessity of simulating the intermediate scenario in evaluating the effect of urbanization.

The time at which the phenomenon could be observed is summarized in Table 4.5. The time varied but in general, the phenomenon could be observed from late afternoon to next day's early morning in August.

These domains share the same feature of having relatively simple wind patterns. Topography may play a role but neither wind pattern nor topography is the decisive cause because the phenomenon could be observed in Buenos Aires, which has relatively complex topography, but could not be observed in Ho Chi Minh City, which is a flat river delta, very close to sea level, and also has a simple wind pattern. This argument does not imply that the phenomenon does not exist in Ho Chi Minh City and 34 other domains but the phenomenon, if exists, could not be visually identified. Perhaps a systematic method to quantify this phenomenon is required. In addition, there are other factors that cannot be analyzed within the scope of this study such as seasonal dependency.

4.4 Chapter Summary

In this chapter, we projected the 2 m air temperature change for 43 megacities in August between the 2006–2015 period (present period) and the 2046–2055 period (future period) using PGW method under the assumptions of uncontrolled urban expansion, RCP8.5 emission forcing, and SSP3 which we interpreted as the worst case scenario for the future.

Quantification of urbanization effect indicated that the effect is observable but negligible at large spatial scale, clearer in old urban area with large variance between saturated old urban and rapidly developing old urban. The effect is clearest and significant in new urban area. We also found that under certain conditions, urbanization effect in urban area can be advected by the wind resulting urbanization effect in faraway non-urban areas.

The methods established in this chapter will be extended further in the next chapter to produce full year projection.

Chapter 5

Future Climate of Megacities: Extension to Full Year

5.1 Introduction

In this chapter, the methodology established in the previous chapter is extended further to study the impact of global warming and urbanization on the regional climate of the 43 megacities. As cities are places with people, the analysis of this chapter focus on not only the regional climate but also on how the regional climate and its change can affect megacity residents. We show that urbanization can drastically speed up the warming in cities and significantly increase the number of people facing extreme warming.

A part of this chapter was published in a scientific journal (Khanh et al., 2023a).

5.2 Methods

Similar to the previous chapter, we also study the worst-case scenario by coupling the Shared Socioeconomic Pathways 3 (SSP3) and the Representative Concentration Pathway 8.5 (RCP8.5). Hereinafter, for conciseness, we use 2010 and 2050 to refer to the 2006–2015 and the 2046–2055 decade, respectively. Our projection consists of two steps: estimating the warming between the pre-industrial era and 2010 and projecting the warming between 2010 and 2050. The final projection is the summation of the two steps.

We estimate the warming between the pre-industrial era (1850–1900) and 2010 (i.e., 2006–2015 decade) by ensemble averaging and time average the of near-surface air temperature variable (tas) of five GCM members (GFDL-ESM2M, IPSL-CM5A-LR, MIROC-ESM-CHEM, HadGEM2-ES, and NorESM1-M) of the Coupled Model Intercomparison Project 5 (CMIP5) for each period and then take the difference between the two. We used the data from the historical run for the pre-industrial period and from the RCP8.5 run for the 2006–2015 period. The estimated warming level for each city is shown in Table A.1. We note that the choice of CMIP5 instead of the newer CMIP6 is to maintain consistency with the assumptions of other datasets (Varquez et al., 2021; Zhou et al., 2019) used in this study.

Table 5.1: Simulation scenarios.

Scenario	Urban surface	Meteorological input
Present	present	present
Intermediate	present	future
Future	future	future

The methods for projecting the warming between 2010 and 2050 is the same as in Chapter 4 except that instead of only one simulation for August for each city and each scenario, 12 simulations for 12 months were conducted.

Calculated urban morphological parameters are available on figshare (Khanh et al., 2021) and summarized in Table A.1.

5.2.1 Simulation Scenarios

Similar to the previous chapter, we also constructed three simulation scenarios (Table 5.1). The present scenario is used as hindcasting to evaluate model performance. The difference between the present and the intermediate scenario is used to assess the impact of global warming and the difference between the intermediate scenario and the future scenario is used to assess the impact of urbanization. We conducted one simulation for each city, each month of the year, and each scenario on the TSUBAME supercomputer.

5.3 Results and Discussion

5.3.1 Model Verification

The hindcasting result was verified against observation data downloaded from the NOAA Integrated Surface Database (ISD) and shown in Table A.2. To save computational resources, we inputted the ensemble average of historical weather data to the model, instead of using the common approach of inputting historical weather data to the model and then ensemble averaging simulation outputs. However, we obtained a good correlation between the simulated temperature and the ensemble average of observed temperature. Additionally, model bias has little effect because we only consider the difference between simulations. Thus, we conclude that the model performance is adequate for further discussion.

5.3.2 Urbanization-Induced Warming

For conciseness, we use the term "urbanization" to refer to projected urbanization between 2010 and 2050, and use the term "warming level" to refer to the increase in air temperature from the pre-industrial period. We project the spatial distribution of warming level in 2050 under two scenarios: with and without urbanization. Here, urbanization covers urban expansion, population change,

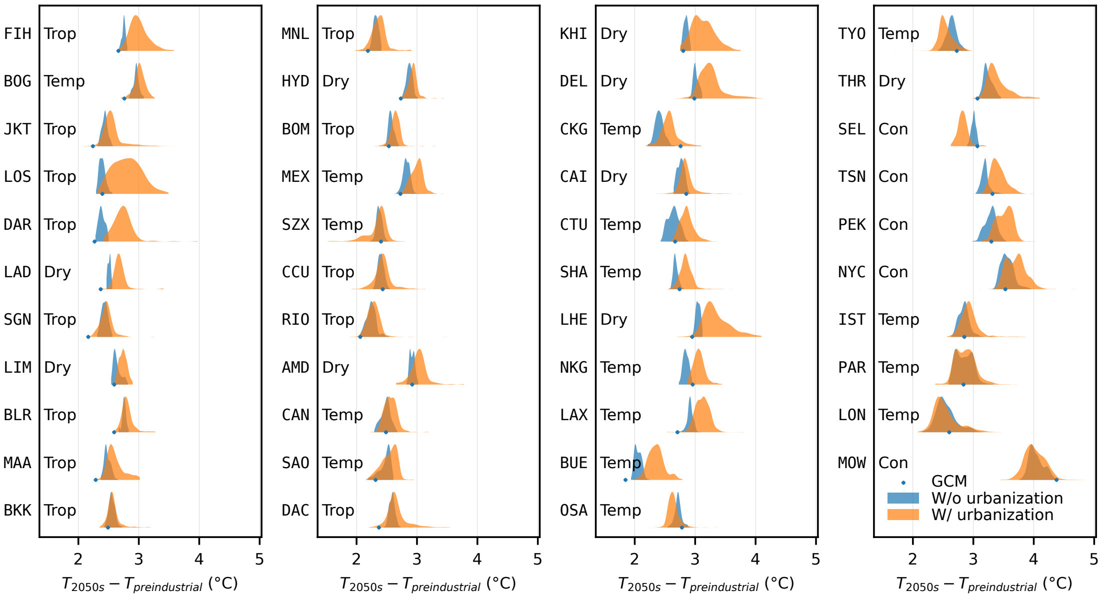

Figure 5.1: Kernel density estimate of 2 km by 2 km gridded warming level in 2050 ($T_{2050s} - T_{preindustrial}$) when urbanization between 2010 and 2050 is not considered (blue shaded area) and when it is considered (orange shaded area) in each of the 43 megacities. The average projection of five GCM members of CMIP5 is indicated by blue dots. Refer to Table 1.1 for city codes. Cities are sorted in the ascending order of latitude (from top to bottom, then, from left to right). Trop, Dry, Temp, and Con represents the Köppen climate classification of tropical, dry, temperate, and continental, respectively (Beck et al., 2018). See also Fig. 5.3 for a detailed graphical explanation.

and economic growth which in turn induces changes in urban morphology and anthropogenic heat emission in the model. The change in heat emission can be negative due to population decline.

The spatial distributions of the warming level in the 43 megacities are plotted using kernel density estimators together with the mean projection of five GCM members of CMIP5 in Fig. 5.1. In each city, the projection of the GCM members of CMIP5 can either fall on the left, on the right, or in the two distributions. That is to say GCM projection of warming level may be either higher or lower than downscaled RCM projection of warming level at urban areas. This difference suggests that using only GCM to project warming level of cities may be insufficient. Without considering the effect of urbanization, the spatial variance of warming level in the megacities are relatively small as indicated by the narrow widths of the blue shaded areas in Fig. 5.1. However, when urbanization is taken into account, the spatial distribution of warming level changes drastically. Together with the growth of the cities, building coverage, building height, and energy usage increases. These factors strengthen the urban heat island effect, making cities warm up faster than the regional and global average. Moreover, because cities do not develop uniformly, the speed of warming varies from location to location. In Fig. 5.1, the warming effect induced by urbanization is indicated by the shift of the warming level distribution from the blue shaded area to the orange shaded area. For example, using the rate of change of urban morphological parameters and anthropogenic heat emission (Table A.1) as a proxy for the speed of urbanization, shifts to the right can be seen clearly in fast

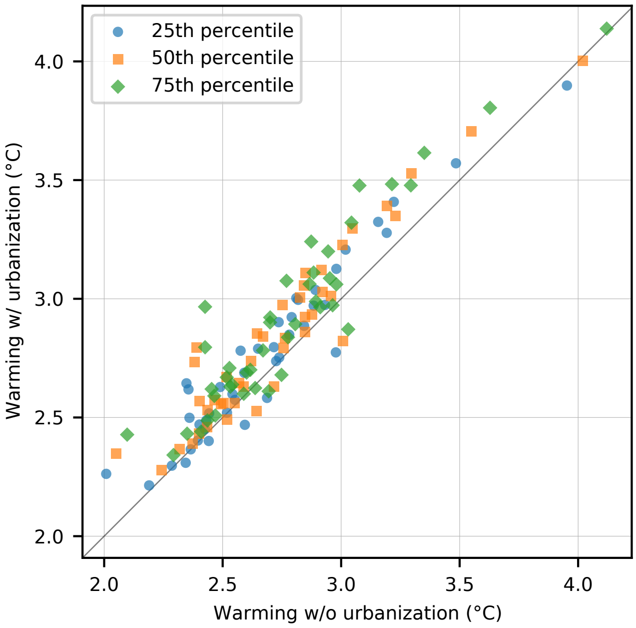

Figure 5.2: The first, second, and third quartiles (25th, 50th, and 75th percentiles) of the gridded warming level in 2050 when urbanization is not considered (horizontal axis) and when it is considered (vertical axis) in each of the 43 megacities. Thus, each city has three dots comparing the three quartiles of the corresponding blue and orange distribution in Fig. 5.1.

growing cities such as Kinshasa, Lima, and Chengdu. On the contrary, for highly developed cities that will be under population decline such as Tokyo, Osaka, and Seoul, incorporating projection of energy usage change results in milder warming than the warming projection without considering energy usage change (i.e., shifts to the left). Also in Fig. 5.1, the non-uniformity of the development speed within each city is reflected in the large variance of the warming level distribution. The warming level of all cities are listed in Appendix C.

Quantitatively, the average warming due to urbanization of each city varies from -0.17 to 0.40 °C with the mean and standard deviation of 0.12 and 0.12 °C, respectively. This large variance reflects the difference in urbanization speed among the cities. Additionally, the interquartile range of the gridded warming projection incorporating the urbanization effect of each city varies from 0.08 to 0.35 °C with the mean value of 0.15 °C. These values demonstrate the difference in warming speed even within the border of a single city. Comparing the quartiles of the gridded warming projection (Fig. 5.2), we found that in general, the projection without consideration of urbanization is lower than the projection with consideration of urbanization in all quartiles and the deviation grows as we move from the lower quartile to the upper quartile. Specifically, the average deviation for the first, second, and third quartiles are 0.08, 0.11, and 0.14 °C, respectively (see also Fig. 5.2). Thus, without considering urbanization, heat-related risks maybe underestimated, especially when the focus is on the upper quartile.

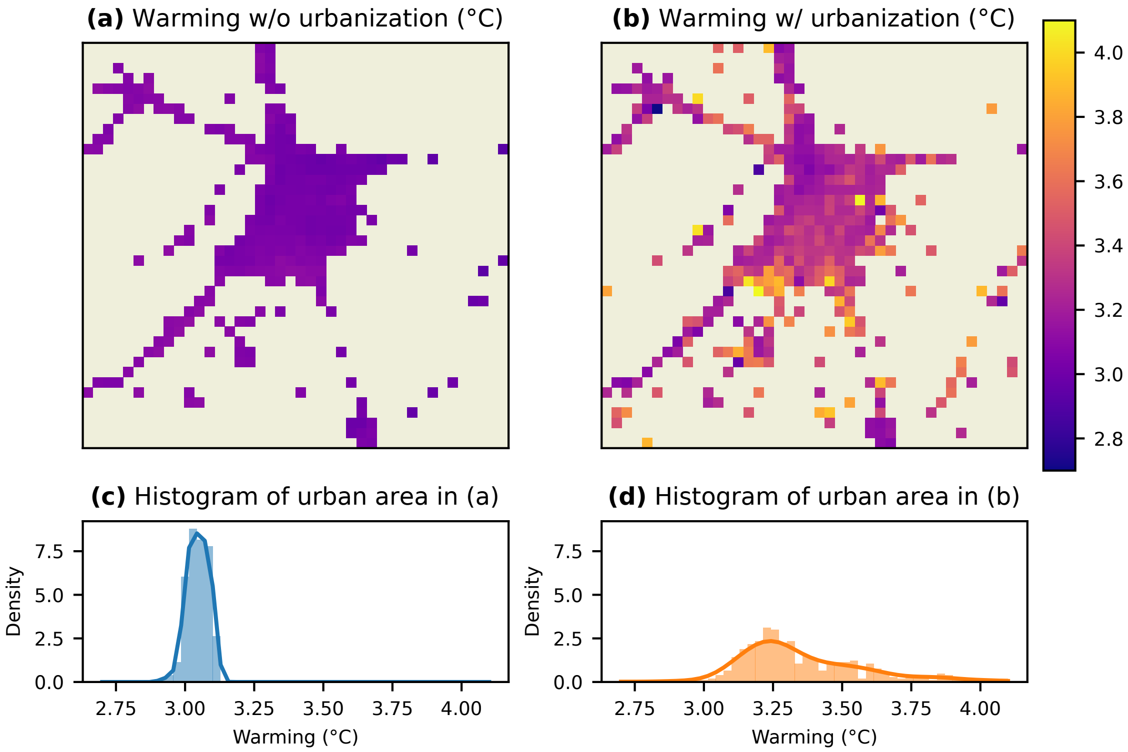

Figure 5.3: Related to Fig. 5.1. Detailed explanation for Lahore (LHE). First, the spatial distribution of the warming without and with urbanization in consideration is plotted in (a) and (b). White lines depict the urban boundary in the present (a) and future (b). These boundaries are drawn based on the land use dataset and they are not administrative boundaries. Next, the normalized histogram of warming within the urban area and kernel density estimates are calculated and plotted in (c) and (d). The distributions shown in Fig. 5.1 are the areas below kernel density estimates (the blue and orange lines), the height of the two areas are adjusted to be the same for better visibility.

5.3.3 Warming and Megacity Dwellers

The number of megacity dwellers affected by a certain warming level is controlled by three factors: present population, population growth, and urban warming. Urbanization is related to the last two factors. In this section, we attempt to quantify the contribution of each of the three factors. For concreteness and simplicity, we use 2.5 °C warming as an example to describe the calculation method. First, we overlaid the present population map with the projected warming level without urbanization map and counted the total number of people exposed to 2.5 °C warming (i.e., the number of people living at grids that have 2.5 °C increase in temperature). This is the number of people exposed to the warming assuming no population, urban, or energy usage growth (first row of Table 5.2(a)). Thus, we regard it as the contribution of present population. Next, we overlaid the future population map with the projected warming level without urbanization map and repeated the count. This is the number of people exposed to the warming assuming population growth but no urban or energy usage growth (thus, no urban warming; second row of Table 5.2(a)). The difference between this number and the contribution of the present population is the contribution of

Table 5.2: The number of people (million) in megacities exposed to various warming levels.

(a) The exposed population (million) under different considerations of urbanization. The plus sign (+) indicates an included factor.

Factors			Warming level			
Present pop.	Pop. growth	Urban warming	≥ 2.0 °C	≥ 2.5 °C	≥ 3.0 °C	≥ 3.5 °C
+			606	427	108	26
+	+		778	508	121	27
+	+	+	778	612	226	53

(b) Contribution of each factor (million of people and percentage) into the exposure to various warming levels.

Factor	Warming level			
	≥ 2.0 °C	≥ 2.5 °C	≥ 3.0 °C	≥ 3.5 °C
Present pop.	606 (78%)	427 (70%)	108 (48%)	26 (49%)
Pop. growth	172 (22%)	81 (13%)	13 (6%)	1 (2%)
Urban warming	0 (0%)	104 (17%)	105 (46%)	26 (49%)
Total	778 (100%)	612 (100%)	226 (100%)	53 (100%)

Table 5.3: Percentage of population in megacities affected by various warming levels. The base is 782 million people from 43 megacities in 2050.

Projection	Warming level			
	≥ 2.0 °C	≥ 2.5 °C	≥ 3.0 °C	≥ 3.5 °C
Without urban warming	99%	65%	15%	3%
With urban warming	100%	78%	29%	7%

population growth. Finally, we did the count for the future population map overlaid on the projected warming level with urbanization map. This is the number of people exposed to the warming when population growth and urban warming are both accounted (third row of Table 5.2(a)). Subtracting the contribution of present population and population growth from this number, we obtained the contribution of urban warming. As shown in Table 5.2(b), 612 million megacity dwellers are projected to be exposed to 2.5 °C warming with the total figure broken down to three contributors as: present population (427 mil., 70%), population growth (81 mil., 13%), and urban warming (104 mil., 17%)

Next, we focus on the impact of the urban warming factor. The projection of the number of people exposed to different warming levels when urban warming is accounted/unaccounted for is shown in Fig. 5.4 and Table 5.3. Regardless of the consideration of urban warming, almost 100% of the population in megacities will be exposed to 2.0 °C warming. Without considering urban warming, 65% of the population in megacities are already at risk of 2.5 °C warming. By considering urban warming, another 13% of the megacity population will be at that risk. Focusing on extreme

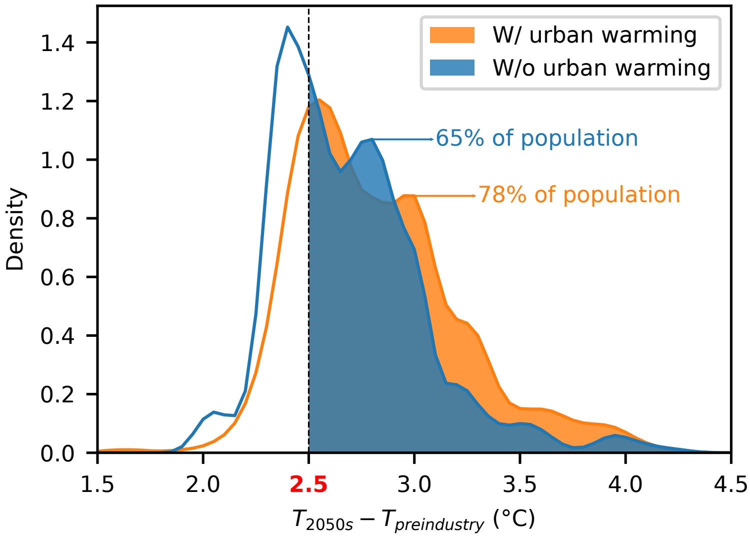

Figure 5.4: Warming level in 2050 (with and without consideration of urban warming) plotted against the number of people who will experience it. The plot is smoothed by a Gaussian kernel density estimator. The area under each curve represents 782 million people from 43 megacities in 2050.

warming of 3.0 and 3.5 °C, we found that the number of affected people is almost doubled when urban warming is taken into account. Moreover, as shown in Table 5.2(b), the contribution of the urban warming factor grows together with the extremeness of the warming level, from 0% in 2.0 °C warming to 17% in 2.5 °C warming and 49% in 3.5 °C warming. Therefore, limiting urban warming (e.g., finding optimal city layout, reducing anthropogenic heat) has a potential to reduce the number of people affected by extreme warming. However, finding a mitigation is not in the scope of this study. Note that all the numbers discussed so far are summations across all the megacities.

The estimation of the change in exposure has some uncertainties due to the uncertainty in estimating the annual average temperature change. The bootstrapping statistical method (*scipy.stats.bootstrap* function of the SciPy library) was used to estimate the uncertainty of temperature change and exposed population. The results of the exposed population at each warming level and its 95 % confidence interval (CI) are shown in Fig. 5.5(a). The CIs have small width (well below 10 %) and is the widest in the 3.0 to 3.5 °C warming range. This can be explained by the fact that under a certain future scenario, the probability of both very weak warming and very strong warming are low and the probability of close-to-the-middle warming level is higher. Therefore, the uncertainty of exposure at very low and very high warming level are low and more uncertainty can be expected at the medium warming level.

The above analysis can be broken down further to compare the difference between megacities in developed (see Fig. 5.5(b)) and developing countries (see Fig. 5.5(c)). In developing countries, it can be seen from Fig. 5.5(c) that the exposed population increases at almost all warming level when urbanization is considered. One exception is around the 4.0 °C warming level (which can also be seen in Fig. 5.4). Around this point, considering urbanization decreases exposed population. The

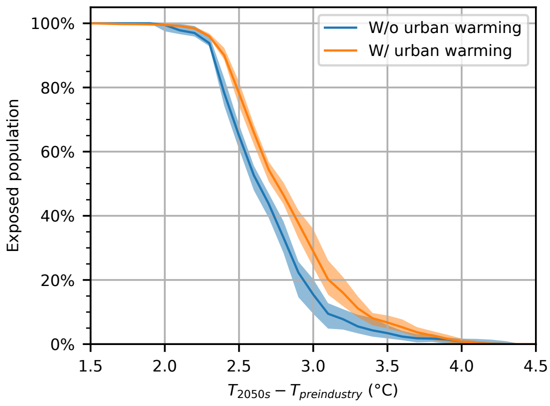

(a) All megacities. This is the cumulative distribution function of Fig. 5.4.

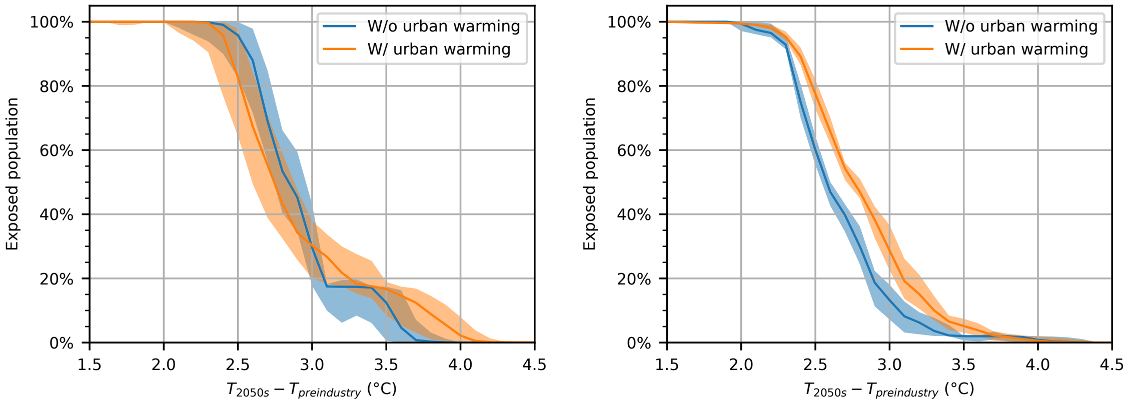

(b) Megacities in developed countries ($n = 7$).

(c) Megacities in developing countries ($n = 36$).

Figure 5.5: The percentage of population of megacities exposed to different warming levels with 95 % confidence intervals represented by the shaded areas.

reason is because Moscow (Russia) is considered a city in a developing country; however, future projection of population and energy usage of Moscow is lower than the present. Consequentially, the projected exposed population decreases when negative urbanization for Moscow is taken in to account. In contrast to megacities in developing countries, megacities in developed countries (see Fig. 5.5(b)) are expected to have population decline. Consequentially, when (negative) urbanization is taken into account, the projected exposed population decreases. However, there is a crossing point between the blue and the orange lines in Fig. 5.5(b) due to the fact megacities in the US are projected to keep growing, unlike megacities in the other developed countries. The bottom line of this analysis is that climatological analysis does not necessarily favor the socioeconomical classification of developing and developed countries.

Another noteworthy point of the comparison between megacities in developed and developing countries (Figs. 5.5(b) and 5.5(c), respectively) is that there are more uncertainties in the projection for the group of megacities in developed countries than its developing counterpart. While there may be many reasons (including meteorological, climatological, and socioeconomical reasons),

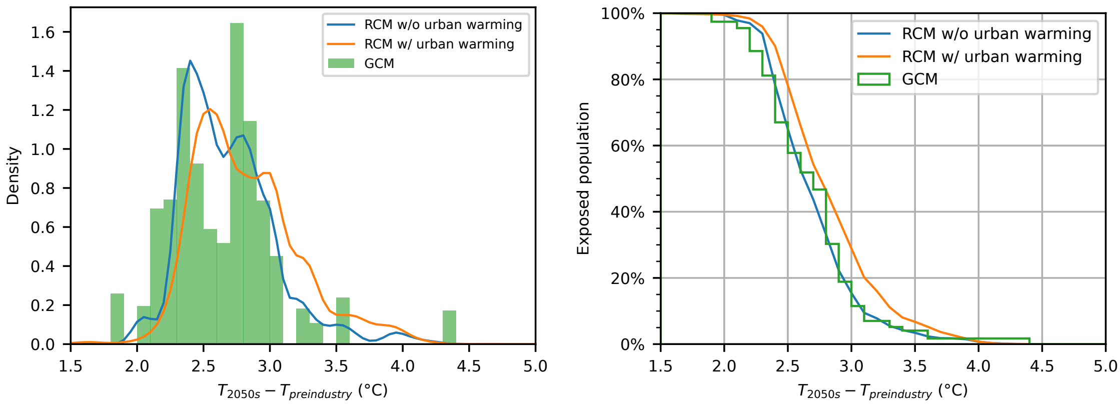

(a) Density function. (b) Complementary cumulative distribution function.

Figure 5.6: Similar to Figs. 5.4 and 5.5(a) but with the projection of exposure by the 5 GCMs (green block and line) added. Projection of GCMs is plotted using histogram because each city has only one GCM data point. The lines for megacities (blue and orange lines) and the histogram both represent 782 million people.

within this analysis, the main reason is the number of cities in each group and a mathematical property of standard deviation. In statistics, it is known that if $X_1, X_2, \ldots, X_n$ are independently and identically distributed variables all with standard deviation of σ, the mean $\overline{X}$ of X_i (in other words, $\overline{X} = (X_1 + X_2 + \ldots + X_n)/n$) will have the standard deviation of $\sigma / \sqrt{n}$. Because there are 7 megacities in developed countries and 36 megacities in developing countries, it is within expectation that when the cities are aggregated together to groups in Figs. 5.5(b) and 5.5(c), the developed country group will have roughly 2.3 times more uncertainty than the developing country group ($\sqrt{36/7} \approx 2.3$). The uncertainty in the projection for developed countries can be reduced by reducing the uncertainty in projection for individual city which can be achieved by, for example, conducting simulation for more days of the year. However, this possible improvement is beyond the scope of this study. This simple statistic analysis also shows that even though the uncertainty in projections for a particular city may be large, if we look at many cities as a pack, or at all cities together as in Fig. 5.5(a), some more certain conclusion may be derived. In addition, while it might be very tempting to divide things into groups (developing vs developed, in this case), there might be better analysis method.

We also attempt to compare the projection of exposure obtained by using temperature downscaled by RCM (specifically, WRF model in this study) and by using temperature obtained directly from the 5 GCMs of CMIP5 (after applying interpolation using the WRF Preprocessing System (WPS)). The result is shown in Fig. 5.6. Because the GCMs have coarse resolution, the distribution drawn using GCM data is also less smooth than the distribution drawn using downscaled data. This point is within expectation. Figures 5.6(a) and 5.6(b) both show that the RCM without urban warming distribution (blue) closely follows the GCM distribution (green). In Fig. 5.6(b), it can be seen that exposure calculated using GCM can be lower or higher than the exposure calculated using RCM without urban warming. This finding can be explained by the previous discussion of Fig. 5.1

that GCM can give both lower and higher projection of future warming levels when compared against RCM (with or without urban warming). Once again, this is because GCM mainly models natural land use while RCM can model highly detailed regional climate with mixture of land use. Furthermore, cities are, in many cases, warmer than its surrounding natural land due to urban heat island. However, it does not mean that cities' response to global warming will be stronger than natural land's response. Previous research has also pointed out the possibility that natural land may warm up faster than cities (Lemonsu et al., 2013). At the moment, there is not enough information to decide whether GCM or RCM projection is more trustworthy; however, both projections can be used as references for further examination.

Next, we turn the discussion to the discussion of risks. Risk of climate change to human has three components: hazard (a weather or climate event that can adversely affect people), vulnerability (level of preparedness to the hazard), and exposure (the presence of people in places that could be affected) (Oke et al., 2017, pp. 380–381; IPCC, 2012). For example, the risk of heat stroke for megacity dwellers has three components: hazard (high air temperature), vulnerability (varying with socioeconomic factors such as population pyramid and availability of cooling system), and exposure (the number of people living at places with high air temperature). Our result indicates that urban warming increases the number of people living at places with high air temperature, thus, increases the exposure component. This may increase the risk of heat stroke in the future. However, the increase in risk is not directly proportional to the increase in exposure because risk also depends on the variation of the hazard component (for example, change in heat wave frequency (Lhotka et al., 2018)) and the vulnerability component (for example, vulnerability is increased due to an aging population but can be lowered by preventive measures (Luber & McGeehin, 2008)). The same argument applies for other kind of heat-related risks; therefore, we conclude that without considering urban warming, there is a possibility of underestimating heat-related risks for cities. A comprehensive study accounting for many climatological and socioeconomical factors may be done in the future to fully project future heat-related illness risks.

5.3.4 A Simple Estimation of the Relation Between Socioeconomic Factors and Urban Warming

As described in detailed in Chapter 3, anthropogenic heat (AH) and urban morphological parameters in this study are all rooted in two socioeconomic factors: GDP and population (see also Fig. 3.4). To be precise, there is a third socioeconomic factor which is energy usage; however, as will be shown later, energy usage and GDP are closely linked. Therefore, in this section, we attempt to make a simple first-order estimation of the link between socioeconomic factors (GDP and population) and the average magnitude of urban warming. Ten megacities (Dar es Salaam, Kinshasa, Lagos, London, Moscow, Osaka, Paris, Seoul, Shenzhen, and Tokyo) are excluded from this analysis due to reasons discussed later (see the discussion for Fig. 5.9).

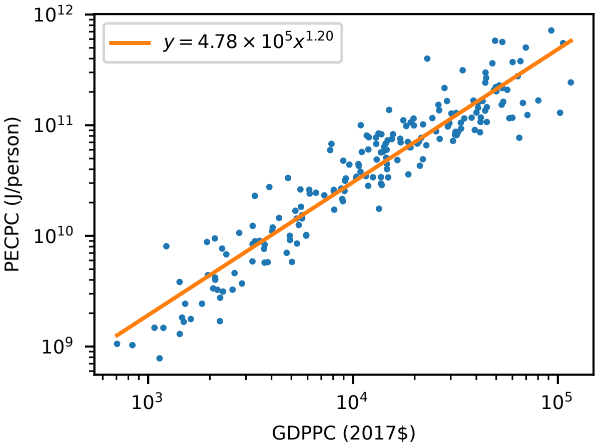

Figure 5.7: Relation between primary energy consumption per capita (PECPC) and GDP per capita (GDPPC) for 192 countries/regions worldwide in 2021 (OWID, 2024).

The Relation Between Energy Use per Person and GDP per Capita

We obtained the data of primary energy consumption per capita (PECPC, J/person) and GDP per capita (GDPPC, US$2017) for 192 countries and region around the world (OWID, 2024). By a simple linear regression (Fig. 5.7), it was found that the relation between the two quantities follows a simple power law of

$$PECPC = \alpha \times GDPPC^{\beta} \qquad (\mathrm{J/person}). \tag{5.1}$$

where $\alpha = 4.78 \times 10^5$ J/person and $\beta = 1.20$ are empirical coefficients. Note that for the dimensional analysis to make sense, the term $GDPPC$ in Eq. (5.1) should be precisely $GDPPC/1$ US$2017 (in other words, numerical value without the unit) but we omit the division against the unit for conciseness (Matta et al., 2011).

The Relation Between Urban Warming and Anthropogenic Heat

In this study, to account for the impact of urbanization both AH and urban morphological parameters were modified. Previous research has also shown that both AH and urban morphological parameters have strong contribution to urban temperature. For example, it was shown that air temperature is positive correlated with H_{avg}, λ_p and λ_f (Deng et al., 2023); urban heat island (UHI) intensity is strongly correlated with gross building volume and city size (Y. Li et al., 2020); UHI intensity is lower when roughness length is higher (Atkinson, 2003; Zhao et al., 2014); and the effect of urban geometries to temperature is less than but comparable to the effect of AH in an idealized setting (Atkinson, 2003). However, here, for simplicity, we assume that the magnitude of urban warming is solely due to the change in AH, even though both AH and urban morphological parameters were modified in the simulation.

Assuming a no wind and vertically well-mixed condition, the extent to which AH can heat up the atmosphere is up to the the boundary layer height. Let ΔAH be the annual averaged change in AH, ΔT is the annual averaged temperature change due to urban warming, and BLH be the harmonic

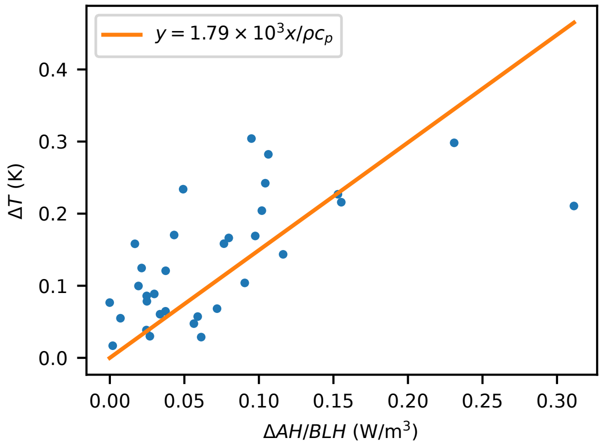

Figure 5.8: Relation between the change in anthropogenic heat (ΔAH), boundary layer height (BLH) and temperature change (ΔT). Each point represent one megacity.

mean of the monthly-hourly diurnal profile of the boundary layer height simulated by the WRF model. It can be expected that ΔT is proportional to $\Delta AH / \left(BLH \times \rho c_p\right)$ where $\rho c_p \approx 1200\,\mathrm{J\,m^{-3}\,K^{-1}}$ is the volumetric heat capacity of air. From Fig. 5.8, it can be seen that this relation is acceptably valid and we have the following equation.

$$\Delta T = \frac{\gamma}{\rho c_p} \times \frac{\Delta AH}{BLH} \quad (\mathrm{K}). \tag{5.2}$$

where

- $\gamma = 1.79 \times 10^3$ s is an empirical coefficient,
- $\Delta\psi = \psi_{2050\mathrm{s}} - \psi_{2010\mathrm{s}}$ for any quantity ψ.

In a closed system, γ should be equal to the integration time because of heat accumulation. However, in this system, γ is approximately 30 minutes. Therefore, it can be interpreted that the impact of anthropogenic heat lasts for about 30 minutes before dissipating. Factors that can affect the magnitude of γ include wind, urban geometries, and other atmospherical factors not considered explicitly in this section.

As a side note, for a set, harmonic mean refers to the reciprocal of the arithmetic mean of the reciprocals of the set's elements, In mathematical terms, the harmonic mean $H(X)$ of $X_1, X_2, \ldots, X_n$ is

$$H(X) = \left[\frac{X_1^{-1} + X_2^{-1} + \ldots + X_n^{-1}}{n}\right]^{-1}. \tag{5.3}$$

The Relation Between Anthropogenic Heat and GDP

Assuming that AH is proportional to primary energy consumption and inversely proportional to the surface area from which AH is emitted (for example, area of a city), we have the following relation by applying Eq. (5.1) for each city.

$$AH \propto \alpha \times GDPPC^{\beta} \times P/A, \tag{5.4}$$

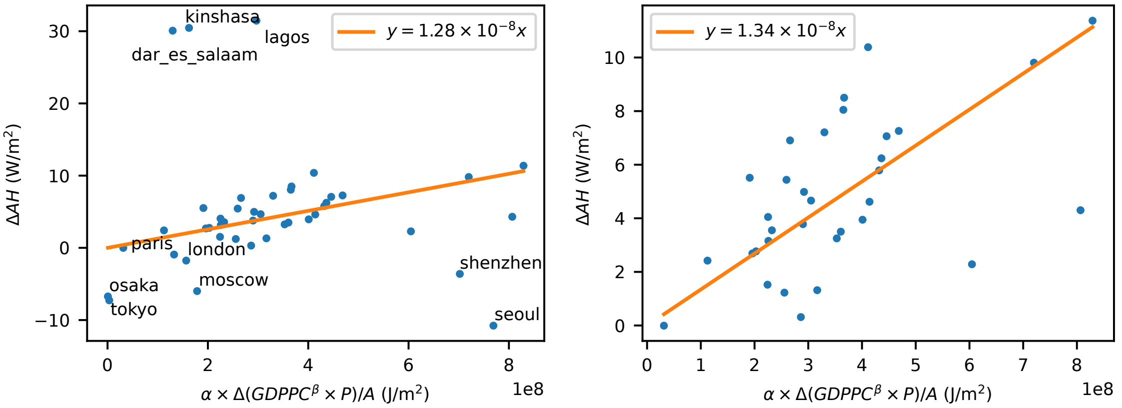

(a) For 43 megacities.

(b) After excluding 9 labeled cities in (a).

Figure 5.9: Relation between $\alpha \times \Delta \left(GDPPC^{\beta} \times P\right)/A$ and ΔAH.

where

- P (people) is the city's population,
- A (m^2) is the surface area of the city. Note that while city area changes with time, we can consider A to be a constant by setting it to the projected future city area and let the AH fluxes from current non-urban grids to zero.

Taking the difference between the values in the 2010s (the present) and the 2050s (the future) we have the following relation,

$$\Delta AH \propto \alpha \times \Delta \left(GDPPC^{\beta} \times P\right)/A, \tag{5.5}$$

Next, we examine the validity of Eq. (5.5) by using GDP, population, and AH data from the same source as in the simulation setup. As can be seen Fig. 5.9(a), the relation is acceptably valid for 33 megacities. The exception to the relation are 3 rapidly developing megacities (Dar es Salaam, Kinshasa, and Lagos) and 7 cities with saturated development (London, Moscow, Osaka, Paris, Seoul, Shenzhen, and Tokyo). For that reasons, the 10 cities are excluded from the analysis in this section. One side note is that, for Shenzhen domain, the part with saturated development and projected decline in energy usage is the Hong Kong Special Administrative Region. The Shenzhen city in Mainland China is still projected to grow. However, because of the proximity of the two administrative divisions, it was not possible to separate the two entities in the simulation. After excluding the 9 cities, we found a good correlation between the left and the right hand sides of Eq. (5.4) as in Fig. 5.9(b). Hence, we have the following equation.

$$\Delta AH = \zeta \alpha \times \Delta \left(GDPPC^{\beta} \times P\right)/A \qquad (\mathrm{W/m^2}). \tag{5.6}$$

where $\zeta = 1.34 \times 10^{-8}\,\mathrm{s}^{-1}$ is an empirical coefficients. Ideally, ζ should be $3.17 \times 10^{-8}\,\mathrm{s}^{-1} \approx 1/(365 \times 24 \times 60 \times 60\,\mathrm{s})$, which is the inverse of the number of seconds in a year. The empirical ζ is smaller than the ideal ζ but the orders of magnitude of the two match each other.

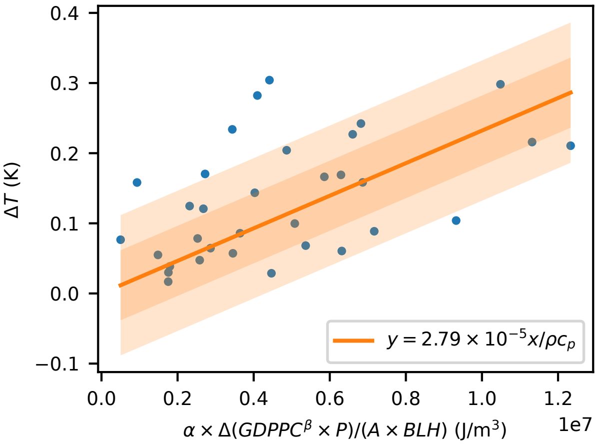

Figure 5.10: The relation between GDP per capita (*GDPPC*), population (*P*), city area (*A*), mean boundary layer height (*BLH*), and temperature *T*. Dark and light shaded area indicate 0.05 and 0.10 °C derivation from the regression line, respectively.

The Relation Between Socioeconomic Factors and Urban Warming

By combining Eqs. (5.2) and (5.6), we can get a rough estimation of future urban warming (see Fig. 5.10). The relation is

$$\Delta T = \frac{\eta}{\rho c_p} \times \frac{\alpha \times \Delta\left(GDPPC^{\beta} \times P\right)}{A \times BLH} \quad (\mathrm{K}). \tag{5.7}$$

where $\eta = 2.79 \times 10^{-5}$ (dimensionless) is an empirical coefficient. Note that to avoid propagation of errors due to multiple rounds of regression, this relation is obtained by fitting a linear equation to the data points in Fig. 5.10 instead of substituting Eq. (5.6) to Eq. (5.2) to get $\eta = \gamma\zeta = 2.40 \times 10^{-5}$. However, it can be confirmed that the η obtained by substitution is closed to η obtained by direct fitting. This equation can be interpreted as: temperature change due to socioeconomic development is proportional to the change in energy usage (the numerator of the second factor of Eq. (5.7) with the unit of J) and inversely proportional to the volume in which the extra energy can disperse (the denominator of the second factor of Eq. (5.7) with the unit of m^3).

As can be seen in Fig. 5.10, even though the estimation was made with a highly simplified bulk model, ignoring wind and the impact of all urban morphological parameters, the performance is remarkable. Specifically, the RMSE is 0.0807 °C, Furthermore, 14 cities (42 %) and 27 cities (81 %) have actual values of ΔT deviate less than 0.05 °C and 0.10 °C from the model's prediction, respectively. The 6 cities that deviate by at least 0.10 °C are Ahmadabad, Chengdu, Chongqing, Karachi, Lahore, and Luanda. It can be expected that these deviations can be explained by the excluded factors such as wind and urban morphological parameters. Note that in such a case, the coefficient η will change. In this relation, there is one parameter which is more difficult to obtain than the other parameters which is the boundary layer height. The direct way is to conduct a simulation or an observation, but because this relation only aims at rough estimation, output from reanalysis datasets (for example, NCEP FNL and ERA5) should suffice.

5.4 Chapter Summary

In this chapter, we projected the future climate of 43 megacities in the 2046–2055 decade under the worst-case scenario of RCP8.5 and SSP3 with consideration of changing urban morphological parameters and anthropogenic heat emission due to urbanization. The major findings are

- In the time frame of 40 years (2010s to 2050s), the effect of urbanization has small mean compared to the effect of global climate change. However, urbanization effect varies significantly from location to location even within the border of one city. Therefore, the spatial variance of the urbanization effect is possibly more important than the mean.

- 78% of megacity population (612 million people) may be exposed to 2.5 °C warming, in which 17% is due to urban warming induced by urbanization from the 2010s to the 2050s. Therefore, urbanization effect should be included in projections of future heat-related illness risks because the effect may increase the risks.

- A simple, first-order relation was derived to connect socioeconomic factors with the magnitude of urban warming. The magnitude is proportional to the change of GDP and population but inversely proportional to the city size and the atmospheric boundary layer height.

Chapter 6

Future Climate of Megacities: Climate Extremes

6.1 Introduction

In the previous chapters, the average features of future climate of megacities were discussed. In this chapter, extending from the methods and findings of previous chapters, we turn our eyes to extreme weather events. While there are many extreme events to be named (heatwaves, cold spells, typhoons, and floods), this chapter's focus is on heatwaves, especially 2022 heatwaves.

In 2022, intense heat waves occur all around the world. Temperature surpassed 40 °C, broke records in many places, severely affected human health, infrastructures, and economic activities (NASA Earth Observatory, 2022). Previous research revealed that urban area are affected more severely by heat waves than rural areas (D. Li & Bou-Zeid, 2013). As climate change progresses, it has been projected that in the future, heat waves might occur more frequently (Lhotka et al., 2018). Projection at global, regional scale (Perkins-Kirkpatrick & Gibson, 2017) and projection for individual cities (Lemonsu et al., 2014) have been done. However, there is currently a lack of studies covering many cities worldwide with diverse background and lack of consideration of futuristic urbanization projection (e.g., projection of change in anthropogenic heat driven by socioeconomic scenarios).

For that reason, in this chapter, we attempt to project three heat waves events occurred in 2022 in three megacities—Delhi (India), London (UK), and Tokyo (Japan)—to the future (the 2050s) under the worst case scenario (SSP3 coupled with RCP8.5). As an improvement from the previous chapters which only use global projections from the Coupled Model Intercomparison Project phase 5 (CMIP5), in this chapter, we also use global projections from the newly released CMIP6. The targets of this chapter are:

- projecting the general characteristics of the heat wave events if they reoccur in the future,
- quantifying the contribution of urbanization,
- quantifying the significance of the choice global climate projections (i.e., CMIP5 vs CMIP6).

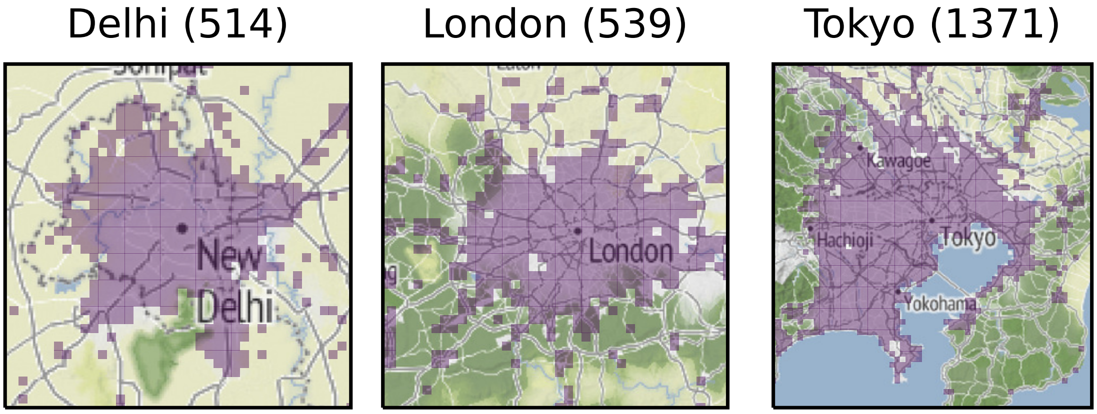

Figure 6.1: Analysis domains (a part of domain 2). The number in the brackets following each city name is the number of urban grids (purple shaded).

A part of this chapter was published in a scientific journal (Khanh et al., 2023b).

6.2 Methodology

A modified version of the Weather Research and Forecast (WRF) model v4.3.1 that can considered spatially varying urban morphological parameters and spatiotemporally varying anthropogenic heat was used (Khanh et al., 2023a). Note that in previous chapters, a modified version of the WRF model v3.3.1 was used. Those modifications were patched to the newer version of the official WRF model (v4.3.1) so that the code can be incorporated to the official model and made available to the research community. Simulation were conducted for Tokyo (2022/06/24–2022/07/02), Delhi (2022/04/06–2022/04/11) and London (2022/07/17–2022/07/19) with the first simulation days used for model spin-up and were excluded from all analysis. Model configuration is described below.

Each city was simulated using two domains with one-way nesting: 10 km resolution (101-by-101 grids) and 2 km resolution (101-by-101 grids for Delhi and London and 151-by-151 grids for Tokyo). The two domains are concentric and centered at 28.6° N 77.1° E, 51.5° N 0.2° W, and 35.5° N 140.0° E for Delhi, London, and Tokyo, respectively (see also Fig. 6.1).

Unlike the previous chapters which utilized the FNL reanalysis dataset (six-hour temporal resolution, 1° spatial resolution), in this chapter, the ERA5 reanalysis dataset with higher spatiotemporal resolutions (hourly temporal resolution, 0.25° spatial resolution) was supplied as initial and boundary conditions to the model for the present climate forcing cases. PGW method was applied similar to the previous chapters. For cases with CMIP5 forcing, five GCM members (rcp8.5 runs of GFDL-ESM2M, HadGEM2-ES, IPSL-CM5A-LR, MIROC-ESM-CHEM, NorESM1-M) were used. For cases with CMIP6 forcing, five GCM members (ssp5-8.5 runs of GFDL-ESM4, HadGEM3-GC31-MM, IPSL-CM6A-LR, MIROC6, NorESM2-MM) were used. Even though the CMIP5 members and the CMIP6 members are not exactly the same, they are of the same family and the CMIP6 members are newer version of the CMIP5 members. Here, we note that in CMIP6, there are two scenarios SSP3-7.0 and SSP5-8.5 (SSP3-8.5 does not exist in CMIP6). However, our urban

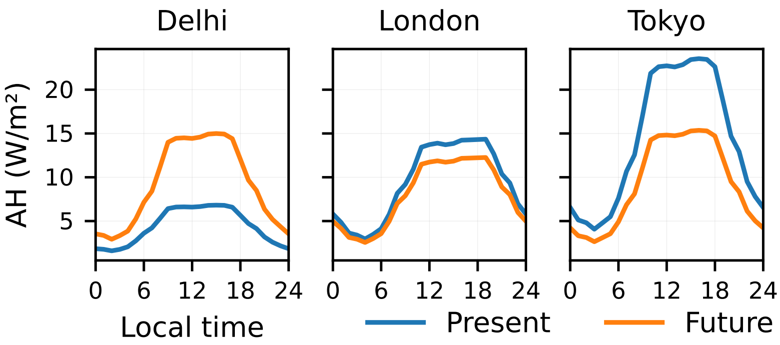

Figure 6.2: Comparison between spatial average of hourly anthropogenic heat between the present and the future.

Table 6.1: Simulation scenarios. Each scenario name has two characters: the first character represent climate forcing (P, 5, and 6 for present, CMIP5, and CMIP6, respectively), and the second character represent urbanization (P and F for present and future, respectively).

Scenario	Climate forcing	Urbanization
PP	Present	Present
PF	Present	Future
5P	CMIP5	Present
5F	CMIP5	Future
6P	CMIP6	Present
6F	CMIP6	Future

morphological dataset and anthropogenic heat dataset were constructed under SSP3 and RCP8.5 assumptions of CMIP5. Therefore, for the cases with CMIP6 forcing, when choosing GCMs, we prioritize the match of radiative forcing (RCP8.5) over the match of socioeconomic pathways (SSP5 and SSP3).

Spatially varying urban morphological parameters were estimated from population, nighttime lights, and gross domestic product (GDP) as in a previous study(Khanh et al., 2023a). The AH4GUC present and future global 1 km hourly anthropogenic heat dataset(Varquez et al., 2021) was also inputted to the model (Fig. 6.2). We note that the AH4GUC dataset was generated for the 2010s and 2050s decade under assumption of CMIP5 instead of the newer CMIP6. However, we use this dataset in this study because at the moment, there is no equivalent dataset under the assumption of CMIP6. Two urbanization scenarios were considered (present and future). The difference between the two scenarios is only in the change of anthropogenic heat. We did not change the urban morphological parameters between the present and the future cases. Similar to a previous research (Khanh et al., 2023a), we modified the MODIS land use dataset included in the WRF model package by setting all grids with population count of at least 1000 to urban category. The same land use dataset is used for all simulations (i.e., no future land use projection is considered).

With three climate forcing scenarios (present, future under CMIP5, future under CMIP6) and

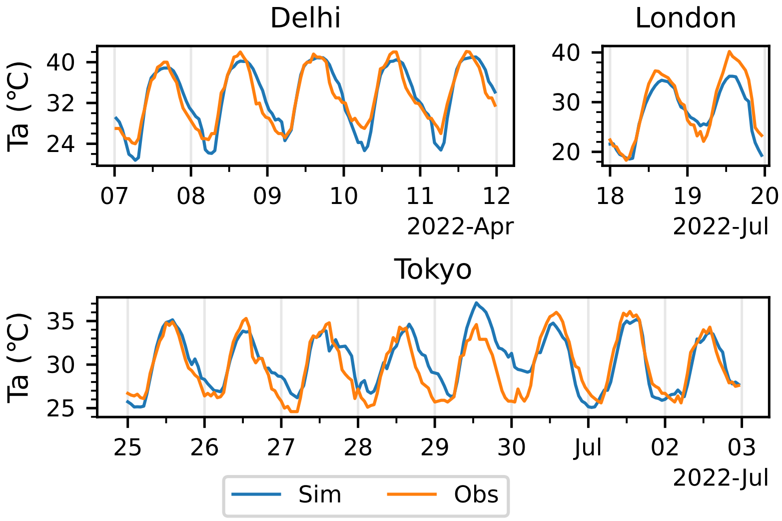

Figure 6.3: Comparison between observed air temperature (orange lines) and simulated near surface air temperature (blue lines).

two urbanization scenarios (present, future), six simulations were conducted for each cities as in Table 6.1.

6.3 Results and Discussion

6.3.1 Model Verification

Simulation results (scenario PP) were verified against observation data downloaded from the NOAA Integrated Surface Database (ISD) (Indira Gandhi International Airport station for Delhi, Heathrow station for London, and Tokyo station for Tokyo). Comparison between hourly observed air temperature and near surface hourly simulated air temperature (air temperature at the first level of WRF model; hereinafter, air temperature) is shown in Fig. 6.3. Even though observation data was point observation and simulation data is 2 km by 2 km grid value, it can be seen that the the model capture well diurnal variation and peaks. The Pearson correlation coefficient is 0.93, 0.95, and 0.86, root mean square error is 2.22, 2.58, and 1.81 °C, respectively for Delhi, London, and Tokyo. In this study, we mainly focus on the difference between simulation cases, thus, it is expected model bias will be minimized by subtraction. To get a reliable projection of future temperature (in terms of actual value, not increment), bias correction is necessary; however, it is not in the scope of this study. From the above analysis, we conclude that the model has adequate performance to study the concerned heat wave events.

6.3.2 Overall Projection

In this section, we give an overall projection of the heat wave events into the future by comparing scenario PP and scenario 6F. In Fig. 6.4, we compare the present and projected future average daily low/high temperature and nighttime/daytime mean temperature over the heat wave periods for the

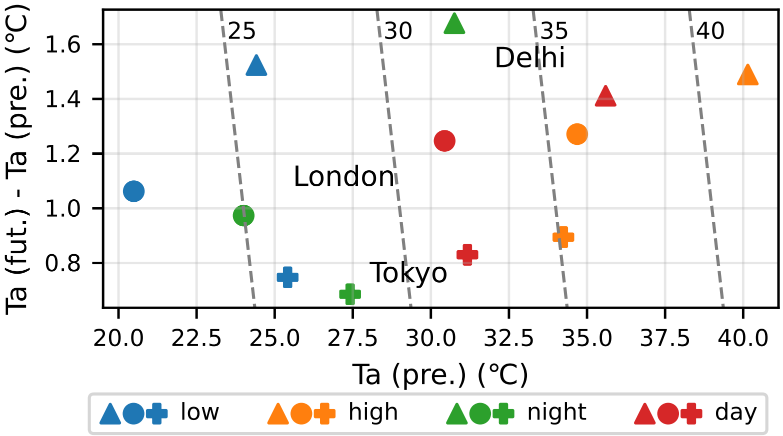

Figure 6.4: Comparison between present (scenario PP) and projected future (scenario 6F) average daily low/high temperature and nighttime/daytime mean air temperature over the heat wave periods for Delhi, London, and Tokyo. Slanting dashed lines connect points with equal sum of x- and y-axis, which can be used to read projected future temperature.

three cities. We found that if similar heat wave events happen in the future, all temperature indices will be higher than the present by 0.8, 1.1, and 1.5 °C on average in Tokyo, London, and Delhi, respectively.

6.3.3 Effects of Urbanization

Under the simulation configuration of this study, the effect of urbanization (i.e., changing anthropogenic heat) can be estimated in three different ways by comparing scenario PP with PF, 5P with 5F, or 6P with 6F. Let the urbanization effect extracted by those comparison be UP, U5, and U6, respectively. By comparing UP, U5, and U6 together, we can judge whether or not the effect of urbanization is influenced by background climate conditions. Specifically, if UP, U5, and U6 are all equals to each other, we can conclude that urbanization effect is independent from background climate conditions. On the contrary, if the three differs, there is a mechanism that suppresses or enhances urbanization effect. In this study, we focus specifically on air temperature change at urban areas (i.e., grids classified as urban in the model, see Fig. 6.1). We will first discuss general characteristics of the effect and then discuss the interaction between urbanization and background climate.

General Characteristics of Urbanization Effect

Time average of urbanization effect (UP, U5, and U6) over the heat wave periods at each urban grid was calculated. The spatial distribution of the time average is shown in Fig. 6.5 in the form of kernel density estimation, separately for daytime and nighttime. In addition, spatial map of the time average of the UP, U5, and U6 ensemble was taken. The spatial average and standard deviation of that map for each city is shown in Table 6.2. The number of urban grids in each city is shown in Fig. 6.1. Overall, urbanization effect in Tokyo and London are negative because of projected

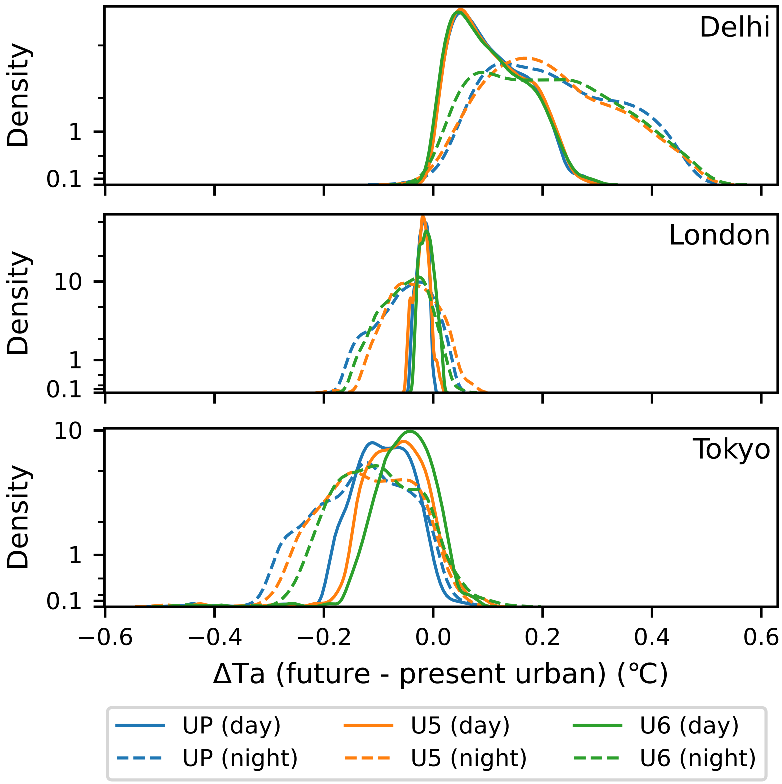

Figure 6.5: Comparison between urbanization effects evaluated under different background climate conditions in daytime (solid lines) and nighttime (dashed lines). The lines represent the spatial distribution (kernel density estimation) of time average of urbanization effect at each urban grid over the heat wave periods.

Table 6.2: Ensemble-spatial average and standard deviation of urbanization effect daytime and nighttime. Unit: 10^{-2} °C.

	Daytime		Nighttime	
	Mean	SD	Mean	SD
Delhi	9.3	5.6	21.0	10.5
London	-1.7	0.7	-4.5	2.9
Tokyo	-6.9	3.8	-11.6	6.9

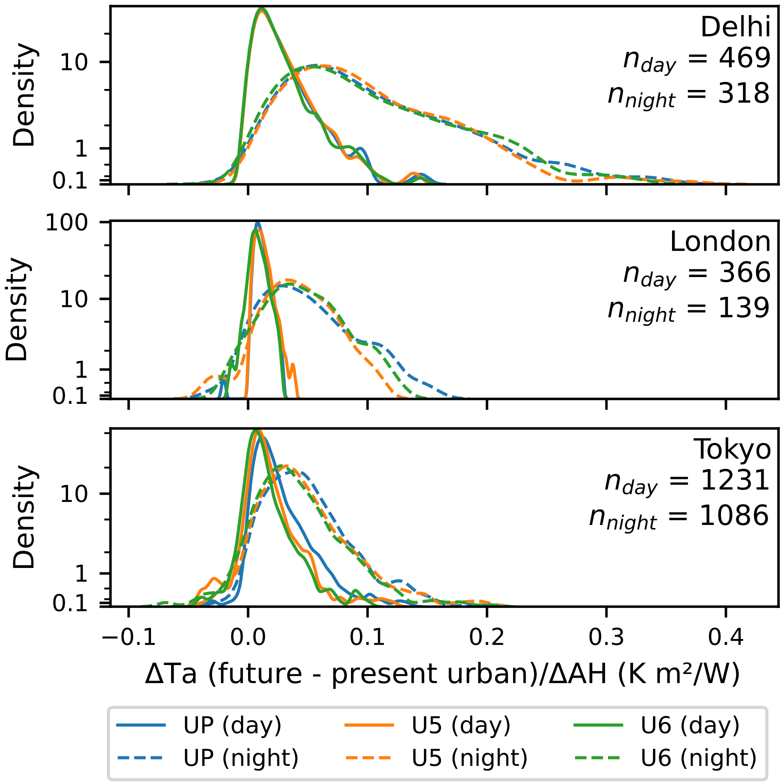

Figure 6.6: Similar to Fig. 6.5 but the average daytime/nighttime temperature change at each grid is normalized by the average daytime/nighttime anthropogenic heat change at that grid. Normalization is only done for grids with $|\Delta AH| \geq 1\,\mathrm{W/m^2}$. The number of grids satisfying the criterion is noted as n_{day} and n_{night}.

decline in anthropogenic heat due to declining population; the reverse is true for Delhi, where population and anthropogenic heat are both projected to be increasing.

From Fig. 6.5 and Table 6.2, it can be seen that in all three cities, the urbanization effect has larger mean (in terms of absolute value) and variance in nighttime than in daytime. Among the three cities, the mean value of urbanization effect is largest in Delhi at nighttime (0.21 °C), which is significant in the total warming at nighttime of 1.68 °C (Fig. 6.4). Depending on the location, the magnitude of urbanization effect is between −0.5 and 0.5 °C, with larger magnitude found in nighttime. This finding reaffirms findings from previous research (Darmanto et al., 2019; Khanh et al., 2023a) that urbanization effect has large spatial variance. We note that while the previous research considered changes in both anthropogenic heat and urban morphological parameters, this study only considers the first factor.

To better explain the effect of anthropogenic heat, we normalize the average daytime/nighttime temperature change at each grid by the average daytime/nighttime anthropogenic heat change at that grid and plotted it in Fig. 6.6, which describes how much temperature changes per unit of anthropogenic heat. Note that normalization is only done for grids with change in anthropogenic heat of at least 1 W/m^2 to avoid unwanted amplification of sensitivity due to division by near-zero value. The purpose of normalization is to investigate sensitivity of air temperature to anthropogenic

Table 6.3: Difference between the means of UP, U5, and U6 at daytime and nighttime. Unit: 10^{-2} °C. Statistical significant derived from the Kolmogorov-Smirnov test is indicated by * ($p < 0.05$) and ** ($p < 0.01$).

		U5 - UP	U6 - UP	U6 - U5
Day	Delhi	0.0	-0.3	-0.3
	London	-0.1	0.6^{**}	0.7^{**}
	Tokyo	2.3^{**}	4.1^{**}	1.8^{**}
Night	Delhi	-0.5	-0.7^{**}	-0.2^{**}
	London	0.9^{**}	-0.2^{**}	-1.1^{**}
	Tokyo	1.0^{**}	2.3^{**}	1.3^{**}

heat, a linear relation between the two quantities is not implied. Similar to the analysis of pre-normalized temperature change (Fig. 6.5), it can be seen that urbanization effect is stronger and more heterogeneous in nighttime than in daytime. This can be explained by the fact that during daytime, stronger near surface wind and higher boundary layer allows anthropogenic heat to disperse both horizontally and vertically, making both absolute magnitude and variance of urbanization effect smaller than during nighttime. It can be seen in Fig. 6.6 that the distributions at nighttime has long right tail. We inspected two-dimensional maps (not shown) of sensitivity visually and found that grids with high sensitivity tends to be in relatively less densely populated areas. One possible hypothesis for this phenomenon is that these areas have less buildings, thus, have smaller heat capacity, consequently, become more sensitive to anthropogenic heat. This hypothesis can be tested in future research by long term simulation of real atmospheric conditions or ideal simulations. It should be note that because anthropogenic heat is advected by wind and interacts with other components of the atmosphere, change in one location might be due to not only local anthropogenic heat change but also due to city-scale anthropogenic heat change and other factors. Therefore, this sensitivity analysis should be interpreted with care.

Urbanization–Background Climate Interaction

As shown in Fig. 6.5, UP, U5, and U6 have similar distributions in daytime and similar distributions in in nighttime; however, the distributions do not completely overlap. In this section, we check whether or not the difference in the distributions are statistically significant. We use the Kolmogorov-Smirnov test for goodness of fit to test if the distributions of urbanization effect are identical. The result is summarized in Table 6.3. There are statistical evidence that the effect of urbanization is not independent from background climate forcing except for Delhi in daytime. The difference between the means of UP, U5, and U6 are in the order of 10^{-3} to 10^{-2} °C. Comparing the difference between the means (in Table 6.3) to the means (in Table 6.2) for Tokyo and London (daytime and nighttime), we found that the maximum difference is 20 to 59 % of the corresponding means in terms of magnitude, therefore, nonnegligible. However, the difference between the means is about two orders of magnitude smaller than the means for Delhi. This finding suggests that the effect of changing anthropogenic heat varies significantly with background climate for Tokyo and London, but

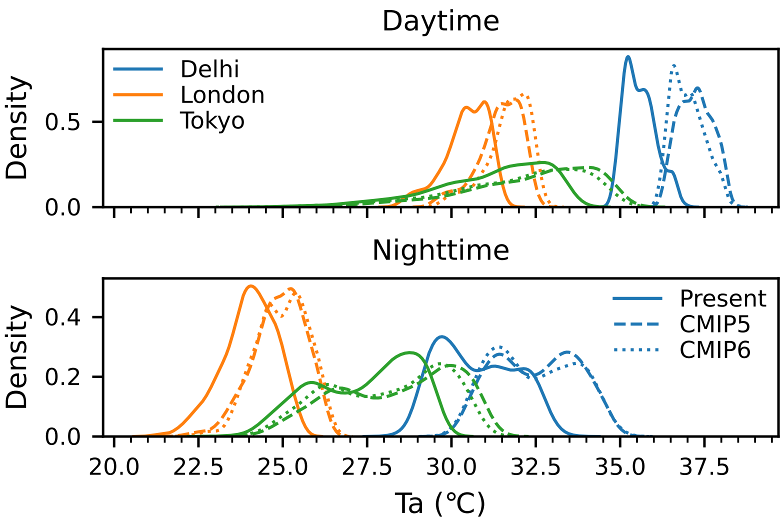

Figure 6.7: Spatial distribution of average daytime/nighttime temperature over the heat wave events in the present (scenario PP), under CMIP5 forcing (scenario 5F), and under CMIP6 forcing (scenario 6F).

negligible for Delhi, for the concerned heat wave events. We note that the dependency/independency discussed here is limited to the context of the analyzed heat wave events.

6.3.4 Future Climate Forcing: CMIP5 and CMIP6

Next we examine if the choice of climate forcing (CMIP5 or CMIP6) has significant influence on the projected future heat wave events. We compare the spatial distribution of average daytime/nighttime temperature over the heat wave events under present (scenario PP), CMIP5 (scenario 5F), and CMIP6 forcing (scenario 6F) for the three cities. The result is shown in Fig. 6.7.

Similar to the investigation of urbanization effect, we conducted the Kolmogorov-Smirnov statistical test to check if the temperature distribution under CMIP5 and CMIP6 forcing are identical. We found that the difference between CMIP5 and CMIP6 was statistically significant for all cities in daytime and for Tokyo in nighttime ($p < 0.01$), and insignificant for Delhi and London at nighttime ($p \geq 0.05$). In the statistical significant cases, the mean difference between CMIP5 and CMIP6 was (in absolute magnitude) between 0.22 and 0.31 °C. One hypothesis for this difference is that numerical models (GCMs) have been updated. Moreover, CMIP5 was based on Representative Concentration Pathways (RCP, for example, RCP8.5) while CMIP6 was based on Shared Socioeconomic Pathways (SSP) coupled with radiative forcing (for example, SSP3-8.5). Therefore, it can be expected that CMIP5 and CMIP6 future projections are different as previous research has also pointed out (Hamed et al., 2022).

While the choice of CMIP5 or CMIP6 has statically significant influence on the projected future heat wave events, it can be seen clearly from Fig. 6.7 that the difference between CMIP5 and CMIP6 is much less than the difference between CMIP5/CMIP6 and the present. Moreover, we note that the minimum between CMIP5 and CMIP6 indicates that if these heat wave events repeat in the future, air temperature will be 1.41, 0.99 and 0.83 °C hotter in daytime and 1.68, 0.88 and 0.69 °C hotter in nighttime for Delhi, London, and Tokyo respectively, on average. In other words, heat waves in the future is projected to be much hotter than in present, regardless of the choice of the older CMIP5 forcing or the newer CMIP6 forcing.

6.4 Chapter Summary

In this study, we attempted to project three heat waves event occurred in 2022 in three megacities—Delhi (India), London (UK), and Tokyo (Japan)—into the future (the 2050s) with consideration of different global climate forcing (CMIP5 and CMIP6) and futuristic projection of urbanization driven on socioeconomic changes under the worst-case scenario (SSP3 coupled with RCP8.5). The main findings are

1. Similar future heat waves will be approximately 0.8 to 1.5 °C hotter than the present. Average through the heat wave period, spatial mean of daily maximum temperature may reach 42, 36, and 35 °C (no bias correction) in Delhi, London, and Tokyo, respectively.

2. Urbanization (i.e., anthropogenic heat change) have stronger impact on the heat waves in nighttime than in daytime. In Delhi, urbanization may add 0.21 °C to nighttime temperature, on average. On the other hand, decreasing energy usage due to population decline in London and Tokyo may cool nighttime temperature down by 0.05 and 0.12 °C, on average, respectively.

3. Urbanization effect has large spatial variance. Absolute magnitude at certain locations in the cities may reach 0.50 °C.

4. Urbanization effect varies (statistically significantly) between different background climate (present, CMIP5, CMIP6), suggesting the existence of complex interaction between background climate condition and anthropogenic heat.

5. The choice of CMIP5 or CMIP6 as future climate forcing has statistically significant impact on the projection. However, the difference between CMIP5 and CMIP6 is much less significant than the difference between CMIP5/CMIP6 and the present.

Finally, to generalize the initial investigation results of this case-study, long-term and/or ideal simulation needs to be conducted.

Chapter 7

Concluding Remarks

7.1 Main Findings

This dissertation expand the current state of knowledge concerning the future regional climate of the world's 43 megacities by conducting future climate projection for the megacities at high resolution with realistic projection of local urbanization from the 2010s to the 2050s. The main findings of the climate projection are summarized as follows.

1. The effect of urbanization (in other words, temperature increase due to urbanization) is observable but may be negligible at large spatial scale. The effect is clearer in existing urban areas but large variance exists between saturated existing urban areas and rapidly developing ones. The effect is clearest and significant in new urban areas.

2. Under certain conditions, urbanization effect in an urban area can be advected by the wind, causing observable urbanization effect in rural areas far from the urban area.

3. In the time frame of 40 years (2010s to 2050s), the effect of urbanization has small mean compared to the effect of global climate change. However, urbanization effect varies significantly from location to location even within the border of one city. Therefore, the spatial variance of the urbanization effect is possibly more important than the mean.

4. 78% of megacity population (612 million people) may be exposed to 2.5 °C warming, in which 17% is due to urban warming induced by urbanization from the 2010s to the 2050s. Therefore, urbanization effect should be included in projections of future heat-related illness risks because the effect may increase the risks.

5. A simple, first-order relation was derived to connect socioeconomic factors with the magnitude of urban warming (Eq. (5.7)). The magnitude is proportional to the change of GDP and population but inversely proportional to the city size and the atmospheric boundary layer height. This relation can be used to quickly estimate the magnitude of urban warming without doing numerical simulation.

This dissertation also projected three heatwaves in 2022 happened in three megacities (Delhi, London, and Tokyo) to the 2050s to identify possible hazards of similar events in the future. The main findings for the concerned heatwaves are as follow.

1. Similar future heat waves will be approximately 0.8 to 1.5 °C hotter than the present. Increase of anthropogenic heat due to increasing population in Delhi can worsen heatwaves. The opposite is true for London and Tokyo due to decreasing population and energy demand.

2. Urbanization effect varies (statistically significantly) between different background climate (present, CMIP5, CMIP6), suggesting the existence of complex interaction between background climate condition and anthropogenic heat.

3. The choice of CMIP5 or CMIP6 as future climate forcing has statistically significant impact on the projection. However, the difference between CMIP5 and CMIP6 is much less significant than the difference between CMIP5/CMIP6 and the present.

7.2 Limitations and Recommendations for Future Research

Limitations and possible future research directions to address those limitations are as follows.

1. Because of limited computational resources, instead of conducting simulations for the full actual ten years, we conducted simulations using ensemble averaged monthly reanalysis data. Future study may develop other computational cheap methods to obtain decadal average of many meteorological variables and compare the performance of these methods against the direct simulation method.

2. We only made projection for the worst-case scenario while projections for other scenarios are equally important. In contrast to the worse-case scenario which gives the upper bound of the impact, best scenario gives the lower bound. The lower bound can be used to determine if the problem is still under control and to determine the minimum investment needed to protect megacities and megacity residences from global climate change and urbanization. Setting of climate change scenarios has been revised continuously from AR4 (A1, B1, etc.) to AR5 (RCP1.9, RCP8.5, etc.) and to the most recent AR6 (SSP1-1.9, SSP5-8.5, etc.) thanks to the advance in the collective knowledge of humanity. Thus, the scenario presented in this dissertation may become obsolete in the future. However, the important point is that the framework proposed can be used for the variety of setting. Specifically, projections for various scenarios can be done by adjusting the projections of urbanization and future energy usage inputted to weather and climate models. Moreover, coupling with integrated assessment models which examine the interaction between energy, climate, and socioeconomics system such as GCAM can give more flexibility to experiment design.

3. Only one urbanization pathway (uncontrolled urban sprawl) was considered in this study. Even though uncertainty due to different urbanization pathways is significant smaller than the

uncertainty due to emission scenarios or GCM projections in the case of a mature metropolis (Kusaka et al., 2016), the uncertainty for rapidly developing megacities in developing countries is unknown. Future research may explore many possibilities of urbanization (sparse city, compact city, interconnected of satellite cities) and evaluate their impacts.

4. Under the setting of this research, the term "impact of urbanization" should be read in full as "impact of urbanization projected under the future climate forcing of RCP8.5". In reality, urbanization and global warming happens simultaneously, unlike the two-step process (first global warming and then urbanization) presented here.

5. Except in Chapter 6, we utilized climate boundaries from CMIP5 datasets for consistency with urbanization scenarios and anthropogenic heat derived from past studies. However, given a generalized methodology presented herein, the findings may be advanced further by considering additional urbanization and climate-change scenarios, such as the newest available CMIP6 datasets.

6. The anthropogenic heat dataset used in this study currently has only two decadal average (the 2010s and the 2050s) and assumes mean conditions. However, in reality, when extreme weather events such as heatwaves or cold spells happen, it can be expected that the anthropogenic heat pattern will be drastically different from the mean condition. Thus, future study may also consider developing methods that can generate more anthropogenic heat maps for various weather conditions. For example, electricity consumption due to air conditioning can be estimated using building energy models (Nakajima et al., 2023). In addition, building materials database and estimation methods for energy usage from other sectors should also be developed. Finally, adjustment will be needed to ensure that the summation of the adaptive anthropogenic heat map is consistent with the projected total global/national energy usage.

7. In terms of potential impact of global and urban warming to megacity dwellers, this study only projected the change in exposure. For a complete projection of risks, information about the change in hazard and vulnerability together with expert knowledge in human health are required (Varquez et al., 2020). This is a shortcoming that needs to be addressed so that megacities have enough information to prepare mitigation and adaptation.

8. Because this study uses regional climate model, all identified impacts of global warming and urbanization are regional impacts. However, as the climate system is inherently complex and chaotic, there are possibilities of teleconnection. In other words, urbanization in one regional may cause changing climate in another distant region. Future research may explore this possibility by combining regional climate research with global climate research.

9. This study only consider one direct impact of urbanization which is the change of building geometries and anthropogenic heat. However, in reality, urbanization has many indirect impacts such as the conversion of distant natural land to farmland to support increasing non-agricultural urban population. In addition, decreasing population may cause demolition of buildings and increase in bare soil or green space in the future. The indirect impacts

of urbanization and the possibility of de-urbanization are both not considered in this study. Future research may consider this research direction. Nevertheless, it is noteworthy that considering both direct and indirect impacts of urbanization will require a future simulation that has a lot of parameters changed from the present simulation. Care should be taken because changing many parameters at once may produce chaotic, complex, and incomprehensible results.

10. This study shows the possibility of modeling regional climate of many cities worldwide with highly detailed urban representation. However, we did not attempt to evaluate the contribution of each urban morphological factors to the temperature change. Future research may address this shortcoming to produce better guideline for urban planning.

The model and global datasets used in this study has been published for free and unrestricted usage. Using our model and global datasets, further research can be done for many cities worldwide, not limited to megacities, to

- investigate the effect of urbanization on meteorological variables other than temperature (for example, humidity, wind speed, and precipitation) and other extreme weather events (for example, cold spells, and typhoons),
- investigate the dependency of urban warming on climate forcing, climate zone, and atmospheric circulation regimes,
- analyze variations and similarities of urban warming among different cities,
- project various consequences of warming to human (for example, change in thermal comfort, heat-related risks, mosquito-borne diseases risks (Messina et al., 2019)).

This study shows the feasibility of and advocates for regional climate study at global scale using a unified approach. However, study focusing on individual cities with fine tune will remain very important to adapt to specific needs that the method used in this study cannot cover. They will also serve as reinforcement for further development of this global approach. Nevertheless, we hope that our approach of using open source model and freely available global datasets will be especially useful for studying developing regions with little data available. We expect that along with global climatological research focusing on the whole globe and urban climatological research focusing on individual cities, more research examining city-scale phenomena from a global point of view will be conducted.

References

Adachi, S. A., & Tomita, H. (2020). Methodology of the constraint condition in dynamical downscaling for regional climate evaluation: A review. *J. Geophys. Res. Atmosphere*, *125*(11), e2019JD032166. https://doi.org/10.1029/2019JD032166

Adachi, S. A., Kimura, F., Kusaka, H., Inoue, T., & Ueda, H. (2012). Comparison of the impact of global climate changes and urbanization on summertime future climate in the Tokyo metropolitan area. *J. Appl. Meteorol. Climatol.*, *51*(8), 1441–1454. https://doi.org/10.1175/JAMC-D-11-0137.1

Ahmad, N. H., Inagaki, A., Kanda, M., Onodera, N., & Aoki, T. (2017). Large-eddy simulation of the gust index in an urban area using the lattice Boltzmann method. *Bound.-Layer Meteorol.*, *163*, 447–467. https://doi.org/10.1007/s10546-017-0233-6

Argüeso, D., Evans, J. P., Fita, L., & Bormann, K. J. (2014). Temperature response to future urbanization and climate change. *Clim. Dyn.*, *42*, 2183–2199. https://doi.org/10.1007/s00382-013-1789-6

Arrhenius, S. (1896). XXXI. On the influence of carbonic acid in the air upon the temperature of the ground. *Lond. Edinb. Dublin Philos. Mag. J. Sci.*, *41*(251), 237–276. https://doi.org/10.1080/14786449608620846

Aruz, J. (2003). Art of the first cities: The third millennium B.C. from the Mediterranean to the Indus. In J. Aruz & R. Wallenfels (Eds.), *Art of the first cities: The third millennium B.C. from the Mediterranean to the Indus*. Metropolitan Museum of Art.

Atkinson, B. W. (2003). Numerical modelling of urban heat-island intensity. *Bound.-Layer Meteorol.*, *109*, 285–310. https://doi.org/10.1023/A:1025820326672

Beck, H. E., Zimmermann, N. E., McVicar, T. R., Vergopolan, N., Berg, A., & Wood, E. F. (2018). Present and future Köppen-Geiger climate classification maps at 1-km resolution. *Sci. Data*, *5*(1), 1–12. https://doi.org/10.1038/sdata.2018.214

Best, M. J., & Grimmond, C. S. B. (2013). Analysis of the seasonal cycle within the first international urban land-surface model comparison. *Bound.-Layer Meteorol.*, *146*, 421–446. https://doi.org/10.1007/s10546-012-9769-7

Brogli, R., Heim, C., Mensch, J., Sørland, S. L., & Schär, C. (2023). The pseudo-global-warming (PGW) approach: Methodology, software package PGW4ERA5 v1.1, validation, and sensitivity analyses. *Geosci. Model. Dev.*, *16*(3), 907–926. https://doi.org/10.5194/gmd-16-907-2023

Bürger, G., Murdock, T. Q., Werner, A. T., Sobie, S. R., & Cannon, A. J. (2012). Downscaling extremes—an intercomparison of multiple statistical methods for present climate. *J. Clim.*, *25*(12), 4366–4388. https://doi.org/10.1175/JCLI-D-11-00408.1

C., S. K., & Lutz, W. (2017). The human core of the shared socioeconomic pathways: Population scenarios by age, sex and level of education for all countries to 2100. *Glob. Environ. Change*, *42*, 181–192. https://doi.org/10.1016/j.gloenvcha.2014.06.004

Chapman, S., Watson, J. E. M., Salazar, A., Thatcher, M., & McAlpine, C. A. (2017). The impact of urbanization and climate change on urban temperatures: A systematic review. *Landsc. Ecol.*, *32*, 1921–1935. https://doi.org/10.1007/s10980-017-0561-4

Chen, F., Kusaka, H., Bornstein, R., Ching, J., Grimmond, C. S. B., Grossman-Clarke, S., Loridan, T., Manning, K. W., Martilli, A., Miao, S., et al. (2011). The integrated WRF/urban modelling system: Development, evaluation, and applications to urban environmental problems. *Int. J. Climatol.*, *31*(2), 273–288. https://doi.org/10.1002/joc.2158

Cheung, C. S. C., & Hart, M. A. (2014). Climate change and thermal comfort in Hong Kong. *Int. J. Biometeorol.*, *58*(2), 137–148. https://doi.org/10.1007/s00484-012-0608-9

Ching, J., Brown, M., Burian, S., Chen, F., Cionco, R., Hanna, A., Hultgren, T., McPherson, T., Sailor, D., Taha, H., et al. (2009). National urban database and access portal tool. *Bull. Am. Meteorol. Soc.*, *90*(8), 1157–1168. https://doi.org/10.1175/2009BAMS2675.1

Ching, J., Mills, G., Bechtel, B., See, L., Feddema, J., Wang, X., Ren, C., Brousse, O., Martilli, A., Neophytou, M., et al. (2018). WUDAPT: An urban weather, climate, and environmental modeling infrastructure for the anthropocene. *Bull. Am. Meteorol. Soc.*, *99*(9), 1907–1924. https://doi.org/10.1175/BAMS-D-16-0236.1

Cuaresma, J. C. (2017). Income projections for climate change research: A framework based on human capital dynamics. *Glob. Environ. Change*, *42*, 226–236. https://doi.org/10.1016/j.gloenvcha.2015.02.012

Dai, A. (2006). Recent climatology, variability, and trends in global surface humidity. *J. Clim.*, *19*(15), 3589–3606. https://doi.org/10.1175/JCLI3816.1

Darmanto, N. S., Varquez, A. C. G., & Kanda, M. (2017). Urban roughness parameters estimation from globally available datasets for mesoscale modeling in megacities. *Urban Clim.*, *21*, 243–261. https://doi.org/10.1016/j.uclim.2017.07.001

Darmanto, N. S., Varquez, A. C. G., Kawano, N., & Kanda, M. (2019). Future urban climate projection in a tropical megacity based on global climate change and local urbanization scenarios. *Urban Clim.*, *29*, 100482. https://doi.org/10.1016/j.uclim.2019.100482

Dellink, R., Chateau, J., Lanzi, E., & Magné, B. (2017). Long-term economic growth projections in the shared socioeconomic pathways. *Glob. Environ. Change*, *42*, 200–214. https://doi.org/10.1016/j.gloenvcha.2015.06.004

Deng, X., Cao, Q., Wang, L., Wang, W., Wang, S., Wang, S., & Wang, L. (2023). Characterizing urban densification and quantifying its effects on urban thermal environments and human thermal comfort. *Landsc. Urban Plan.*, *237*, 104803. https://doi.org/10.1016/j.landurbplan.2023.104803

Dijkstra, L., Hamilton, E., Lall, S., & Wahba, S. (2020, March 10). *How do we define cities, towns, and rural areas?* Retrieved December 29, 2023, from https://blogs.worldbank.org/sustainablecities/how-do-we-define-cities-towns-and-rural-areas

Doan, Q.-V., Chen, F., Kusaka, H., Dipankar, A., Khan, A., Hamdi, R., Roth, M., & Niyogi, D. (2022). Increased risk of extreme precipitation over an urban agglomeration with future global warming. *Earth's Future*, *10*(6), e2021EF002563. https://doi.org/10.1029/2021EF002563

Doan, Q.-V., Kusaka, H., & Ho, Q.-B. (2016). Impact of future urbanization on temperature and thermal comfort index in a developing tropical city: Ho Chi Minh City. *Urban Clim.*, *17*, 20–31. https://doi.org/10.1016/j.uclim.2016.04.003

Doan, Q.-V., Kusaka, H., & Nguyen, T. M. (2019). Roles of past, present, and future land use and anthropogenic heat release changes on urban heat island effects in Hanoi, Vietnam: Numerical experiments with a regional climate model. *Sustain. Cities Soc.*, *47*, 101479. https://doi.org/10.1016/j.scs.2019.101479

Dong, Y., Varquez, A. C. G., & Kanda, M. (2017). Global anthropogenic heat flux database with high spatial resolution. *Atmospheric Environ.*, *150*, 276–294. https://doi.org/10.1016/j.atmosenv.2016.11.040

Ekström, M., Grose, M. R., & Whetton, P. H. (2015). An appraisal of downscaling methods used in climate change research. *Wiley Interdiscip. Rev. Clim. Chang.*, *6*(3), 301–319. https://doi.org/10.1002/wcc.339

Elvidge, C. D., Baugh, K., Zhizhin, M., Hsu, F. C., & Ghosh, T. (2017). VIIRS night-time lights. *Int. J. Remote. Sens.*, *38*(21), 5860–5879. https://doi.org/10.1080/01431161.2017.1342050

Fallmann, J., Emeis, S., & Suppan, P. (2013). Mitigation of urban heat stress–a modelling case study for the area of Stuttgart. *Die Erde–J. Geogr. Soc. Berl.*, *144*(3-4), 202–216. https://doi.org/10.12854/erde-144-15

Fox, S. (2012). Urbanization as a global historical process: Theory and evidence from sub-Saharan Africa. *Popul. Dev. Rev.*, *38*(2), 285–310. https://doi.org/10.1111/j.1728-4457.2012.00493.x

Fujibe, F. (2011). Urban warming in Japanese cities and its relation to climate change monitoring. *Int. J. Clim.*, *31*(2), 162–173. https://doi.org/10.1002/joc.2142

Gao, Y., Wang, L., & Yue, Y. (2024). Impact of irrigation on vulnerability of winter wheat under extreme climate change scenario: A case study of North China Plain. *Front. Sustain. Food Syst.*, *7*, 1291866. https://doi.org/10.3389/fsufs.2023.1291866

Garuma, G. F. (2018). Review of urban surface parameterizations for numerical climate models. *Urban Clim.*, *24*, 830–851. https://doi.org/10.1016/j.uclim.2017.10.006

Geleta, T. D., Dadi, D. K., Funk, C., Garedew, W., Eyelade, D., & Worku, A. (2022). Downscaled climate change projections in urban centers of Southwest Ethiopia using CORDEX Africa simulations. *Climate*, *10*(10), 158. https://doi.org/10.3390/cli10100158

Giannaros, T. M., Melas, D., Daglis, I. A., Keramitsoglou, I., & Kourtidis, K. (2013). Numerical study of the urban heat island over Athens (Greece) with the WRF model. *Atmospheric Environ.*, *73*, 103–111. https://doi.org/10.1016/j.atmosenv.2013.02.055

Gonzalez-Aparicio, I., Monforti, F., Volker, P., Zucker, A., Careri, F., Huld, T., & Badger, J. (2017). Simulating European wind power generation applying statistical downscaling to reanalysis data. *Appl. Energy*, *199*, 155–168. https://doi.org/10.1007/s00703-008-0330-7

Hamdi, R., Degrauwe, D., & Termonia, P. (2012). Coupling the Town Energy Balance (TEB) scheme to an operational limited-area NWP model: Evaluation for a highly urbanized area in Belgium. *Weather Forecast.*, *27*(2), 323–344. https://doi.org/10.1175/WAF-D-11-00064.1

Hamed, M. M., Nashwan, M. S., & Shahid, S. (2022). Inter-comparison of historical simulation and future projections of rainfall and temperature by CMIP5 and CMIP6 GCMs over Egypt. *Int. J. Clim.*, *42*(8), 4316–4332. https://doi.org/10.1002/joc.7468

Hara, M., Yoshikane, T., Kawase, H., & Kimura, F. (2008). Estimation of the impact of global warming on snow depth in Japan by the pseudo-global-warming method. *Hydrol. Res. Lett.*, *2*, 61–64. https://doi.org/10.3178/hrl.2.61

He, W., Zhang, L., & Yuan, C. (2022). Future air temperature projection in high-density tropical cities based on global climate change and urbanization–a study in Singapore. *Urban Clim.*, *42*, 101115. https://doi.org/10.1016/j.uclim.2022.101115

Honjo, T., Lin, T.-P., & Seo, Y. (2019). Sky view factor measurement by using a spherical camera. *J. Agric. Meteorol.*, *75*(2), 59–66. https://doi.org/10.2480/agrmet.D-18-00027

Hrisko, J., Ramamurthy, P., Melecio-Vázquez, D., & Gonzalez, J. E. (2020). Spatiotemporal variability of heat storage in major US cities—a satellite-based analysis. *Remote Sens.*, *13*(1), 59. https://doi.org/10.3390/rs13010059

Huth, R. (2002). Statistical downscaling of daily temperature in Central Europe. *J. Clim.*, *15*(13), 1731–1742. https://doi.org/10.1175/1520-0442(2002)015<1731:SDODTI>2.0.CO;2

Ichinose, T., Shimodozono, K., & Hanaki, K. (1999). Impact of anthropogenic heat on urban climate in Tokyo. *Atmospheric Environ.*, *33*(24-25), 3897–3909. https://doi.org/10.1016/S1352-2310(99)00132-6

Inagaki, A., Watanabe, T., Makedonas, A. M., Khanh, D. N., & Kanda, M. (2022). Improvement of roughness length modelling for densely packed highrise building areas. *J. Jpn. Soc. Civ. Eng. Ser. B1 (Hydraulic Eng.)*, *78*(2), I_709–I_714. https://doi.org/10.2208/jscejhe.78.2_I_709

IPCC. (1992). *Climate change: The 1990 and 1992 IPCC assessments: IPCC First Assessment Report, overview and policymaker summaries and 1992 IPCC supplement.*

IPCC. (1995). *IPCC Second Assessment: Climate change 1995.*

IPCC. (2001). *Climate change 2001: Synthesis report: A contribution of Working Groups I, II, and III to the Third Assessment Report of the Integovernmental Panel on Climate Change* (R. T. Watson & Core Writing Team, Eds.). Cambridge University Press.

IPCC. (2007). *Climate change 2007: Synthesis report: Contribution of Working Groups I, II and III to the Fourth Assessment Report of the Intergovernmental Panel on Climate Change* (Core Writing Team, R. K. Pachauri, & A. Reisinger, Eds.).

IPCC. (2012). Summary for policymakers. In C. B. Field, V. Barros, T. F. Stocker, D. Qin, D. J. Dokken, K. L. Ebi, M. D. Mastrandrea, K. J. Mach, G.-K. Plattner, S. K. Allen, M. Tignor, & P. M. Midgley (Eds.), *Managing the risks of extreme events and disasters to advance climate change adaptation: Special report of the Intergovernmental Panel on Climate Change* (pp. 1–19). Cambridge University Press.

IPCC. (2014). *Climate change 2014: Synthesis report: Contribution of Working Groups I, II and III to the Fifth Assessment Report of the Intergovernmental Panel on Climate Change* (Core Writing Team, R. K. Pachauri, & L. A. Meyer, Eds.).

IPCC. (2023). *Climate change 2023: Synthesis report: Contribution of Working Groups I, II and III to the Sixth Assessment Report of the Intergovernmental Panel on Climate Change* (Core Writing Team, H. Lee, & J. Romero, Eds.). https://doi.org/10.59327/IPCC/AR6-9789291691647

Jyoteeshkumar Reddy, P., Sriram, D., Gunthe, S. S., & Balaji, C. (2021). Impact of climate change on intense Bay of Bengal tropical cyclones of the post-monsoon season: A pseudo global warming approach. *Clim. Dyn.*, *56*, 2855–2879. https://doi.org/10.1007/s00382-020-05618-3

Kanda, M., Inagaki, A., Miyamoto, T., Gryschka, M., & Raasch, S. (2013). A new aerodynamic parametrization for real urban surfaces. *Bound.-Layer Meteorol.*, *148*(2), 357–377. https://doi.org/10.1007/s10546-013-9818-x

Kanda, M., Kawai, T., & Nakagawa, K. (2005). A simple theoretical radiation scheme for regular building arrays. *Bound.-Layer Meteorol.*, *114*, 71–90. https://doi.org/10.1007/s10546-004-8662-4

Karttunen, S., Kurppa, M., Auvinen, M., Hellsten, A., & Järvi, L. (2020). Large-eddy simulation of the optimal street-tree layout for pedestrian-level aerosol particle concentrations–a case study from a city-boulevard. *Atmospheric Environ. X*, *6*, 100073. https://doi.org/10.1016/j.aeaoa.2020.100073

Kawano, N. (2018). *Distributed urban parametric database for global urban climatology* [Doctoral dissertation, Tokyo Institute of Technology].

Khanh, D. N. (2019). *Construction of high-resolution global urban parameters dataset for climate models* [Bachelor's Independent Research Project Report]. Tokyo Institute of Technology.

Khanh, D. N., Varquez, A. C. G., & Kanda, M. (2020). Future climate projection of megacities considering urbanization scenarios. *J. Jpn. Soc. Civ. Eng., Ser. B1 (Hydraul. Eng.)*, *76*(2), I_103–I_108. https://doi.org/10.2208/jscejhe.76.2_I_103

Khanh, D. N., Varquez, A. C. G., & Kanda, M. (2021). Present and future 1 km resolution global population density and urban morphological parameters. https://doi.org/10.6084/m9.figshare.17108981

Khanh, D. N., Varquez, A. C. G., & Kanda, M. (2023a). Impact of urbanization on exposure to extreme warming in megacities. *Heliyon*, *9*(4), e1551. https://doi.org/10.1016/j.heliyon.2023.e15511

Khanh, D. N., Varquez, A. C. G., & Kanda, M. (2023b). Multi-megacity investigation of heat wave events under various climate change and urbanization scenarios. *J. Jpn. Soc. Civ. Eng. Ser. B1 (Hydraulic Eng.)*

Kimura, F., & Kitoh, A. (2007). Downscaling by pseudo global warming method. *The Final Report of ICCAP*, *4346*.

Kiyomoto, S. (2018). *Global future anthropogenic heat estimation* [Master's thesis, Tokyo Institute of Technology].

Kondo, H., Genchi, Y., Kikegawa, Y., Ohashi, Y., Yoshikado, H., & Komiyama, H. (2005). Development of a multi-layer urban canopy model for the analysis of energy consumption in a big city: Structure of the urban canopy model and its basic performance. *Bound.-Layer Meteorol.*, *116*, 395–421. https://doi.org/10.1007/s10546-005-0905-5

Krayenhoff, E. S., Jiang, T., Christen, A., Martilli, A., Oke, T. R., Bailey, B. N., Nazarian, N., Voogt, J. A., Giometto, M. G., Stastny, A., et al. (2020). A multi-layer urban canopy meteorological model with trees (BEP-Tree): Street tree impacts on pedestrian-level climate. *Urban Clim.*, *32*, 100590. https://doi.org/10.1016/j.uclim.2020.100590

Kusaka, H., Chen, F., Tewari, M., Dudhia, J., Gill, D. O., Duda, M. G., Wang, W., & Miya, Y. (2012). Numerical simulation of urban heat island effect by the WRF model with 4-km grid increment: An inter-comparison study between the urban canopy model and slab model. *J. Meteorol. Soc. Jpn. Ser II*, *90*(0), 33–45. https://doi.org/10.2151/jmsj.2012-B03

Kusaka, H., & Kimura, F. (2004). Coupling a single-layer urban canopy model with a simple atmospheric model: Impact on urban heat island simulation for an idealized case. *J. Meteorol. Soc. Jpn. Ser. II*, *82*(1), 67–80. https://doi.org/10.2151/jmsj.82.67

Kusaka, H., Kondo, H., Kikegawa, Y., & Kimura, F. (2001). A simple single-layer urban canopy model for atmospheric models: Comparison with multi-layer and slab models. *Bound.-Layer Meteorol.*, *101*, 329–358. https://doi.org/10.1023/A:1019207923078

Kusaka, H., Suzuki-Parker, A., Aoyagi, T., Adachi, S. A., & Yamagata, Y. (2016). Assessment of RCM and urban scenarios uncertainties in the climate projections for August in the 2050s in Tokyo. *Clim. Chang.*, *137*(3), 427–438. https://doi.org/10.1007/s10584-016-1693-2

Lee, S.-H., Song, C.-K., Baik, J.-J., & Park, S.-U. (2009). Estimation of anthropogenic heat emission in the Gyeong-In region of Korea. *Theor. Appl. Clim.*, *96*, 291–303. https://doi.org/10.1007/s00704-008-0040-6

Lemonsu, A., Beaulant, A. L., Somot, S., & Masson, V. (2014). Evolution of heat wave occurrence over the Paris basin (France) in the 21st century. *Clim. Res.*, *61*(1), 75–91. https://doi.org/10.3354/cr01235

Lemonsu, A., Kounkou-Arnaud, R., Desplat, J., Salagnac, J.-L., & Masson, V. (2013). Evolution of the Parisian urban climate under a global changing climate. *Clim. Change*, *116*, 679–692. https://doi.org/10.1007/s10584-012-0521-6

Levermore, G., Parkinson, J., Lee, K., Laycock, P., & Lindley, S. (2018). The increasing trend of the urban heat island intensity. *Urban Clim.*, *24*, 360–368. https://doi.org/10.1016/j.uclim.2017.02.004

Lhotka, O., Kyselŷ, J., & Farda, A. (2018). Climate change scenarios of heat waves in Central Europe and their uncertainties. *Theor. Appl. Climatol.*, *131*(3), 1043–1054. https://doi.org/10.1007/s00704-016-2031-3

Li, D., & Bou-Zeid, E. (2013). Synergistic interactions between urban heat islands and heat waves: The impact in cities is larger than the sum of its parts. *J. Appl. Meteorol. Clim.*, *52*(9), 2051–2064. https://doi.org/10.1175/JAMC-D-13-02.1

Li, D., Liao, W., Rigden, A. J., Liu, X., Wang, D., Malyshev, S., & Shevliakova, E. (2019). Urban heat island: Aerodynamics or imperviousness? *Sci. Adv.*, *5*(4), eaau4299. https://doi.org/10.1126/sciadv.aau4299

Li, D., Malyshev, S., & Shevliakova, E. (2016). Exploring historical and future urban climate in the Earth System Modeling framework: 1. Model development and evaluation. *J. Adv. Model. Earth Syst.*, *8*(2), 917–935. https://doi.org/10.1002/2015MS000578

Li, H., Liu, Y., Zhang, H., Xue, B., & Li, W. (2021). Urban morphology in China: Dataset development and spatial pattern characterization. *Sustain. Cities Soc.*, *71*, 102981. https://doi.org/10.1016/j.scs.2021.102981

Li, H., Zhou, Y., Wang, X., Zhou, X., Zhang, H., & Sodoudi, S. (2019). Quantifying urban heat island intensity and its physical mechanism using WRF/UCM. *Sci. Total Environ.*, *650*, 3110–3119. https://doi.org/10.1016/j.scitotenv.2018.10.025

Li, Y., Schubert, S., Kropp, J. P., & Rybski, D. (2020). On the influence of density and morphology on the urban heat island intensity. *Nat. Commun.*, *11*(1), 2647. https://doi.org/10.1038/s41467-020-16461-9

Luber, G., & McGeehin, M. (2008). Climate change and extreme heat events. *Am. J. Prev. Med.*, *35*(5), 429–435. https://doi.org/10.1016/j.amepre.2008.08.021

Macdonald, R. W., Griffiths, R. F., & Hall, D. J. (1998). An improved method for the estimation of surface roughness of obstacle arrays. *Atmospheric Environ.*, *32*(11), 1857–1864. https://doi.org/10.1016/s1352-2310(97)00403-2

Martilli, A., Clappier, A., & Rotach, M. W. (2002). An urban surface exchange parameterisation for mesoscale models. *Bound.-Layer Meteorol.*, *104*, 261–304. https://doi.org/10.1023/A:1016099921195

Martilli, A., Krayenhoff, E. S., & Nazarian, N. (2020). Is the urban heat island intensity relevant for heat mitigation studies? *Urban Clim.*, *31*, 100541. https://doi.org/10.1016/j.uclim.2019.100541

Martinez-García, F. P., Contreras-de-Villar, A., & Muñoz-Perez, J. J. (2021). Review of wind models at a local scale: Advantages and disadvantages. *J. Mar. Sci. Eng.*, *9*(3), 318. https://doi.org/10.3390/jmse9030318

Masson, V. (2000). A physically-based scheme for the urban energy budget in atmospheric models. *Bound.-Layer Meteorol.*, *94*(3), 357–397. https://doi.org/10.1023/A:1002463829265

Matta, C. F., Massa, L., Gubskaya, A. V., & Knoll, E. (2011). Can one take the logarithm or the sine of a dimensioned quantity or a unit? dimensional analysis involving transcendental functions. *J. Chem. Educ.*, *88*(1), 67–70. https://doi.org/10.1021/ed1000476

McCarthy, M. P., Best, M. J., & Betts, R. A. (2010). Climate change in cities due to global warming and urban effects. *Geophys. Res. Lett.*, *37*(9). https://doi.org/10.1029/2010GL042845

Messina, J. P., Brady, O. J., Golding, N., Kraemer, M. U. G., Wint, G. R. W., Ray, S. E., Pigott, D. M., Shearer, F. M., Johnson, K., Earl, L., et al. (2019). The current and future global distribution and population at risk of dengue. *Nat. Microbiol.*, *4*(9), 1508–1515. https://doi.org/10.1038/s41564-019-0476-8

Miao, S., Chen, F., Li, Q., & Fan, S. (2011). Impacts of urban processes and urbanization on summer precipitation: A case study of heavy rainfall in Beijing on 1 August 2006. *J. Appl. Meteorol. Clim.*, *50*(4), 806–825. https://doi.org/10.1175/2010JAMC2513.1

Middel, A., Lukasczyk, J., Maciejewski, R., Demuzere, M., & Roth, M. (2018). Sky view factor footprints for urban climate modeling. *Urban Clim.*, *25*, 120–134. https://doi.org/10.1016/j.uclim.2018.05.004

Miyamoto, Y., Kajikawa, Y., Yoshida, R., Yamaura, T., Yashiro, H., & Tomita, H. (2013). Deep moist atmospheric convection in a subkilometer global simulation. *Geophys. Res. Lett.*, *40*(18), 4922–4926. https://doi.org/10.1002/grl.50944

Morisita, M. (1965). The fitting of the logistic equation to the rate of increase of population density. *Res. Popul. Ecol.*, *7*(1), 52–55. https://doi.org/10.1007/BF02518815

Moriwaki, R., Kanda, M., Senoo, H., Hagishima, A., & Kinouchi, T. (2008). Anthropogenic water vapor emissions in Tokyo. *Water Resour. Res.*, *44*(11). https://doi.org/10.1029/2007WR006624

Nakajima, K., Takane, Y., Kikegawa, Y., & Yamaguchi, K. (2023). Improvement of WRF–CM–BEM and its application to high-resolution hindcasting of summertime urban electricity consumption. *Energy Build.*, *296*, 113336. https://doi.org/10.1016/j.enbuild.2023.113336

Narita, Y., Varquez, A. C. G., Nakayoshi, M., & Kanda, M. (2019). Construction of land use database before urbanization for global urban climate analysis. *J. Jpn. Soc. Civ. Eng., Ser. B1 (Hydraul. Eng.)*, *75*(2), I_1039–I_1044. https://doi.org/10.2208/jscejhe.75.2_I_1039

NASA Earth Observatory. (2022). *Heatwaves and fires scorch Europe, Africa, and Asia*. Retrieved May 28, 2023, from https://earthobservatory.nasa.gov/images/150083/heatwaves-and-fires-scorch-europe-africa-and-asia

NOAA NCEI. (2024). *Climate at a glance: Global time series*. Retrieved January 19, 2024, from https://www.ncei.noaa.gov/access/monitoring/climate-at-a-glance/global/time-series

Oh, M., Lee, J., Kim, J.-Y., & Kim, H.-G. (2022). Machine learning-based statistical downscaling of wind resource maps using multi-resolution topographical data. *Wind Energy*, *25*(6), 1121–1141. https://doi.org/10.1002/we.2718

Oke, T. R. (1982). The energetic basis of the urban heat island. *Q. J. R. Meteorol. Soc.*, *108*(455), 1–24. https://doi.org/10.1002/qj.49710845502

Oke, T. R., Mills, G., Christen, A., & Voogt, J. A. (2017). *Urban climates*. Cambridge University Press.

Our World in Data. (2024). *Energy use per person vs. GDP per capita, 2021*. Retrieved January 26, 2024, from https://ourworldindata.org/grapher/energy-use-per-person-vs-gdp-per-capita

Perkins-Kirkpatrick, S. E., & Gibson, P. B. (2017). Changes in regional heatwave characteristics as a function of increasing global temperature. *Sci. Rep.*, *7*(1), 1–12. https://doi.org/10.1038/s41598-017-12520-2

Reder, A., Raffa, M., Padulano, R., Rianna, G., & Mercogliano, P. (2022). Characterizing extreme values of precipitation at very high resolution: An experiment over twenty European cities. *Weather Clim. Extremes*, 100407. https://doi.org/10.1016/j.wace.2022.100407

Riahi, K., van Vuuren, D. P., Kriegler, E., Edmonds, J., O'Neill, B. C., Fujimori, S., Bauer, N., Calvin, K., Dellink, R., Fricko, O., Lutz, W., Popp, A., Cuaresma, J. C., KC, S., Leimbach, M., Jiang, L., Kram, T., Rao, S., Emmerling, J., … Tavoni, M. (2017). The shared socioeconomic pathways and their energy, land use, and greenhouse gas emissions implications: An overview. *Glob. Environ. Change*, *42*, 153–168. https://doi.org/10.1016/j.gloenvcha.2016.05.009

Rubel, F., & Kottek, M. (2010). Observed and projected climate shifts 1901–2100 depicted by world maps of the Köppen-Geiger climate classification. *Meteorol. Z.*, *19*(2), 135–141. https://doi.org/10.1127/0941-2948/2010/0430

Sachindra, D. A., Ahmed, K., Rashid, M. M., Shahid, S., & Perera, B. J. C. (2018). Statistical downscaling of precipitation using machine learning techniques. *Atmospheric Res.*, *212*, 240–258. https://doi.org/10.1016/j.atmosres.2018.05.022

Sailor, D. J., Georgescu, M., Milne, J. M., & Hart, M. A. (2015). Development of a national anthropogenic heating database with an extrapolation for international cities. *Atmospheric Environ.*, *118*, 7–18. https://doi.org/10.1016/j.atmosenv.2015.07.016

Salam, M. A., Furuya, J., & Kobayashi, S. (2017). Climate effect on supply and market price stability of rice in Bangladesh: Assessment of climate and socioeconomic scenarios. *Jpn. J. Agric. Econ.*, *19*, 60–65. https://doi.org/10.18480/jjae.19.0_60

Schär, C., Frei, C., Lüthi, D., & Davies, H. C. (1996). Surrogate climate-change scenarios for regional climate models. *Geophys. Res. Lett.*, *23*(6), 669–672. https://doi.org/10.1029/96GL00265

Schneider, A., Friedl, M. A., & Potere, D. (2009). A new map of global urban extent from MODIS satellite data. *Environ. Res. Lett.*, *4*(4), 044003. https://doi.org/10.1088/1748-9326/4/4/044003

Shaffer, S. R., Chow, W. T. L., Georgescu, M., Hyde, P., Jenerette, G. D., Mahalov, A., Moustaoui, M., & Ruddell, B. L. (2015). Multiscale modeling and evaluation of urban surface energy balance in the Phoenix metropolitan area. *J. Appl. Meteorol. Clim.*, *54*(2), 322–338. https://doi.org/10.1175/JAMC-D-14-0051.1

Shen, C., Liu, Y., Shen, A., Cui, Y., Chen, X., Fan, Q., Chan, P., Tian, C., Xie, Z., Wang, C., et al. (2023). Spatializing the roughness length of heterogeneous urban surfaces to improve the WRF simulation-Part 2: Impacts on the thermodynamic environment. *Atmospheric Environ.*, *294*, 119464. https://doi.org/10.1016/j.atmosenv.2022.119464

Stewart, I. D., & Oke, T. R. (2012). Local climate zones for urban temperature studies. *Bull. Am. Meteorol. Soc.*, *93*(12), 1879–1900. https://doi.org/10.1175/BAMS-D-11-00019.1

Steyn, D. (1980). The calculation of view factors from fisheye-lens photographs: Research note. *Atmosphere-Ocean*, *18*(3), 254–258. https://doi.org/10.1080/07055900.1980.9649091

Takahashi, K., Honda, Y., & Emori, S. (2007). Assessing mortality risk from heat stress due to global warming. *J. Risk Res.*, *10*(3), 339–354. https://doi.org/10.1080/13669870701217375

Takemi, T., Yoshida, T., Yamasaki, S., & Hase, K. (2019). Quantitative estimation of strong winds in an urban district during typhoon Jebi (2018) by merging mesoscale meteorological and large-eddy simulations. *SOLA*, *15*, 22–27. https://doi.org/10.2151/sola.2019-005

Taniguchi, K., & Sho, K. (2015). Application of the pseudo global warming dynamic downscaling method to the Tokai Heavy Rain in 2000. *J. Meteorol. Soc. Jpn. Ser II*, *93*(5), 551–570. https://doi.org/10.2151/jmsj.2015-043

Tareghian, R., & Rasmussen, P. F. (2013). Statistical downscaling of precipitation using quantile regression. *J. Hydrol.*, *487*, 122–135. https://doi.org/10.1016/j.jhydrol.2013.02.029

Tewari, M., Chen, F., Kusaka, H., & Miao, S. (2007). *Coupled WRF/unified Noah/urban-canopy modeling system.*

UN DESA. (2018). *The world's cities in 2018–data booklet*. UN. https://doi.org/10.18356/c93f4dc6-en

UN-Habitat. (2022). *World cities report 2022*.

Varentsov, M., Wouters, H., Platonov, V., & Konstantinov, P. (2018). Megacity-induced mesoclimatic effects in the lower atmosphere: A modeling study for multiple summers over Moscow, Russia. *Atmosphere*, *9*(2), 50. https://doi.org/10.3390/atmos9020050

Varquez, A. C. G. (2014). *The meteorological effects of detailed urban parameter inclusion to Weather Research and Forecasting Model on dry days* [Doctoral dissertation, Tokyo Institute of Technology].

Varquez, A. C. G., Darmanto, N., Kawano, N., Takakuwa, S., Kanda, M., & Xin, Z. (2017). Representative urban growing scenarios for future climate models. *J. Jpn. Soc. Civ. Eng., Ser. B1 (Hydraul. Eng.)*, *73*(4), I_103–I_108. https://doi.org/10.2208/jscejhe.73.i_103

Varquez, A. C. G., Darmanto, N. S., Honda, Y., Ihara, T., & Kanda, M. (2020). Future increase in elderly heat-related mortality of a rapidly growing Asian megacity. *Sci. Rep.*, *10*(1), 1–9. https://doi.org/10.1038/s41598-020-66288-z

Varquez, A. C. G., & Kanda, M. (2018). Global urban climatology: A meta-analysis of air temperature trends (1960–2009). *npj Clim. Atmospheric Sci.*, *1*(1), 1–8. https://doi.org/10.1038/s41612-018-0042-8

Varquez, A. C. G., Kawano, N., Kanda, M., & Nakayoshi, M. (2018). Numerical investigation of anthropogenic heat emission impacts on large Asian cities. *J. Jpn. Soc. Civ. Eng. Ser. B1 (Hydraulic Eng.)*, *74*(5), I_1177–I_1182. https://doi.org/10.2208/jscejhe.74.5_I_1177

Varquez, A. C. G., Kiyomoto, S., Khanh, D. N., & Kanda, M. (2021). Global 1-km present and future hourly anthropogenic heat flux. *Sci. Data*, *8*, 64. https://doi.org/10.1038/s41597-021-00850-w

Varquez, A. C. G., Nakayoshi, M., & Kanda, M. (2015). The effects of highly detailed urban roughness parameters on a sea-breeze numerical simulation. *Bound.-Layer Meteorol.*, *154*(3), 449–469. https://doi.org/10.1007/s10546-014-9985-4

Wang, F., Ge, Q., Wang, S., Li, Q., & Jones, P. D. (2015). A new estimation of urbanization's contribution to the warming trend in China. *J. Clim.*, *28*(22), 8923–8938. https://doi.org/10.1175/JCLI-D-14-00427.1

Wang, L., Sun, T., Zhou, W., Liu, M., & Li, D. (2023). Deciphering the sensitivity of urban canopy air temperature to anthropogenic heat flux with a forcing-feedback framework. *Environ. Res. Lett.*, *18*(9), 094005. https://doi.org/10.1088/1748-9326/ace7e0

Wang, M., Kroeze, C., Strokal, M., van Vliet, M. T. H., & Ma, L. (2020). Global change can make coastal eutrophication control in China more difficult. *Earth's Future*, *8*(4), e2019EF001280. https://doi.org/10.1029/2019EF001280

Wang, X., Wu, Z., & Liang, G. (2009). WRF/CHEM modeling of impacts of weather conditions modified by urban expansion on secondary organic aerosol formation over Pearl River Delta. *Particuology*, *7*(5), 384–391. https://doi.org/10.1016/j.partic.2009.04.007

Wang, Z.-H., Bou-Zeid, E., Au, S. K., & Smith, J. A. (2011). Analyzing the sensitivity of WRF's single-layer urban canopy model to parameter uncertainty using advanced Monte Carlo simulation. *J. Appl. Meteorol. Clim.*, *50*(9), 1795–1814. https://doi.org/10.1175/2011JAMC2685.1

Wiltshire, A. J., Duran Rojas, M. C., Edwards, J. M., Gedney, N., Harper, A. B., Hartley, A. J., Hendry, M. A., Robertson, E., & Smout-Day, K. (2020). JULES-GL7: The global land configuration of the Joint UK Land Environment Simulator version 7.0 and 7.2. *Geosci. Model. Dev.*, *13*(2), 483–505. https://doi.org/10.5194/gmd-13-483-2020

Wouters, H., Demuzere, M., Blahak, U., Fortuniak, K., Maiheu, B., Camps, J., Tielemans, D., & van Lipzig, N. P. M. (2016). The efficient urban canopy dependency parametrization (SURY) v1.0 for atmospheric modelling: Description and application with the COSMO-CLM model for a Belgian summer. *Geosci. Model. Dev.*, *9*(9), 3027–3054. https://doi.org/10.5194/gmd-9-3027-2016

Xie, Z.-T., & Castro, I. P. (2009). Large-eddy simulation for flow and dispersion in urban streets. *Atmospheric Environ.*, *43*(13), 2174–2185. https://doi.org/10.1016/j.atmosenv.2009.01.016

Yoshikane, T., Kimura, F., Kawase, H., & Nozawa, T. (2012). Verification of the performance of the pseudo-global-warming method for future climate changes during June in East Asia. *SOLA*, *8*, 133–136. https://doi.org/10.2151/sola.2012-033

Yucel, M., Varquez, A. C. G., Darmanto, N., & Kanda, M. (2016). Improvements of urban representation in weather models using global datasets. *J. Jpn. Soc. Civ. Eng., Ser. B1 (Hydraul. Eng.)*, *72*(4), I_91–I_96. https://doi.org/10.2208/jscejhe.72.I_91

Zhao, L., Lee, X., Smith, R. B., & Oleson, K. (2014). Strong contributions of local background climate to urban heat islands. *Nature*, *511*(7508), 216–219. https://doi.org/10.1038/nature13462

Zhao, L., Oleson, K., Bou-Zeid, E., Krayenhoff, E. S., Bray, A., Zhu, Q., Zheng, Z., Chen, C., & Oppenheimer, M. (2021). Global multi-model projections of local urban climates. *Nat. Clim. Chang.*, *11*(2), 152–157. https://doi.org/10.1038/s41558-020-00958-8

Zhou, Y., Varquez, A. C. G., & Kanda, M. (2019). High-resolution global urban growth projection based on multiple applications of the SLEUTH urban growth model. *Sci. Data*, *6*(1). https://doi.org/10.1038/s41597-019-0048-z

Zhou, Y., Smith, S. J., Zhao, K., Imhoff, M., Thomson, A., Bond-Lamberty, B., Asrar, G. R., Zhang, X., He, C., & Elvidge, C. D. (2015). A global map of urban extent from nightlights. *Environ. Res. Lett.*, *10*(5), 054011. https://doi.org/10.1088/1748-9326/10/5/054011

APPENDIX A

Supplementary Tables

Table A.1: Average values of urban morphological parameters and anthropogenic heat emisison (AHE) in the 2010s and 2050s, and warming level in the 2010s $\left(\Delta T_{2010s} = T_{2010s} - T_{preindustrial}\right)$ of the 43 megacities. The value in the 2050s are given in percentage increase from the value in the 2010s. Note that because present and future city boundaries are different, the spatial average values are taken within the present city boundary for a fair comparison. Refer to Table 1.1 for city codes.

City	H_{avg} (m)		λ_p		λ_f		z_0 (m)		d (m)		AHE (W/m^2)		ΔT_{2010s}
	2010	Δ2050	2010	Δ2050	2010	Δ2050	2010	Δ2050	2010	Δ2050	2010	Δ2050	(°C)
AMD	7.18	4.9%	0.11	3.1%	0.07	3.0%	0.49	10.8%	8.29	7.5%	3.56	108.1%	1.07
BKK	6.68	6.8%	0.11	6.4%	0.08	5.5%	0.56	13.1%	7.77	11.9%	5.14	3.1%	1.11
BLR	8.24	22.9%	0.13	1.9%	0.10	1.1%	0.96	41.6%	11.28	31.9%	4.66	126.7%	1.19
BOG	9.91	18.5%	0.17	14.6%	0.13	19.3%	1.16	41.6%	14.24	28.5%	9.25	49.0%	1.17
BOM	7.53	9.8%	0.11	0.3%	0.08	0.4%	0.59	21.1%	9.12	14.5%	5.14	109.3%	0.99
BUE	9.95	22.6%	0.16	12.9%	0.12	15.8%	1.03	45.0%	14.09	32.0%	10.44	77.9%	0.80
CAI	8.44	4.3%	0.14	2.8%	0.10	2.2%	0.77	7.0%	11.20	6.3%	8.78	23.6%	1.10
CAN	5.18	5.6%	0.08	0.3%	0.06	0.1%	0.30	15.4%	4.88	10.3%	3.76	120.5%	0.64
CCU	6.29	3.2%	0.09	1.5%	0.06	1.2%	0.38	9.5%	6.60	5.7%	2.37	110.8%	0.83
CKG	5.68	3.5%	0.08	1.4%	0.06	1.5%	0.34	11.3%	5.64	6.9%	5.73	127.3%	0.60
CTU	5.85	6.2%	0.09	0.1%	0.06	0.1%	0.37	19.2%	5.96	11.1%	5.24	130.0%	0.73
DAC	5.91	3.1%	0.08	2.9%	0.06	1.4%	0.34	5.0%	5.92	5.8%	1.62	1.2%	0.73
DAR	7.46	47.2%	0.12	63.5%	0.09	69.7%	0.63	119.7%	9.04	85.6%	1.91	1729.5%	1.01
DEL	8.29	7.5%	0.13	3.8%	0.09	3.0%	0.74	14.0%	10.82	10.5%	4.23	110.5%	1.00
FIH	9.08	24.5%	0.14	31.8%	0.10	36.1%	0.87	56.2%	12.23	39.2%	3.14	1127.8%	1.17
HYD	8.82	14.9%	0.13	1.0%	0.09	0.9%	0.81	34.0%	11.61	21.3%	4.88	118.3%	1.21
IST	8.93	13.0%	0.14	9.2%	0.10	9.8%	0.89	25.9%	12.23	19.0%	11.64	17.5%	1.02
JKT	7.45	8.4%	0.11	8.0%	0.07	3.2%	0.51	9.9%	8.49	14.4%	3.55	97.2%	1.02
KHI	9.21	32.5%	0.15	32.4%	0.11	36.4%	0.95	65.5%	12.70	48.1%	6.71	143.8%	1.11
LAD	9.36	39.4%	0.15	48.5%	0.12	50.0%	1.06	64.3%	13.25	56.3%	4.78	145.8%	0.92

Table A.1: (Cont.)

City	H_{avg} (m)		λ_p		λ_f		z_0 (m)		d (m)		AHE (W/m^2)		ΔT_{2010s}
	2010	Δ2050	2010	Δ2050	2010	Δ2050	2010	Δ2050	2010	Δ2050	2010	Δ2050	(°C)
LAX	6.72	3.0%	0.10	4.4%	0.07	2.5%	0.45	4.2%	7.32	4.7%	14.31	39.5%	0.82
LHE	7.75	11.8%	0.12	11.7%	0.08	8.0%	0.63	16.2%	9.69	16.8%	3.73	72.3%	0.90
LIM	8.06	17.6%	0.14	12.2%	0.10	13.3%	0.83	39.4%	10.40	29.9%	5.99	38.1%	1.21
LON	8.30	6.1%	0.12	0.7%	0.08	0.5%	0.68	11.6%	10.47	8.5%	12.01	-17.4%	0.99
LOS	7.27	31.1%	0.11	38.9%	0.08	35.1%	0.55	58.5%	8.67	50.6%	2.50	1968.0%	0.83
MAA	7.02	2.9%	0.10	1.3%	0.07	0.8%	0.44	6.1%	7.98	4.2%	3.58	114.7%	0.96
MEX	9.54	19.1%	0.16	10.5%	0.12	11.1%	1.04	34.0%	13.64	26.2%	10.08	100.2%	1.19
MNL	7.68	16.9%	0.12	18.8%	0.09	19.3%	0.65	36.6%	9.72	27.3%	3.24	39.2%	0.90
MOW	7.98	5.9%	0.12	0.2%	0.08	0.1%	0.63	11.9%	9.88	8.3%	23.19	-28.9%	1.29
NKG	7.56	26.8%	0.11	0.0%	0.08	0.0%	0.70	55.0%	9.31	40.0%	9.28	126.8%	0.75
NYC	5.08	6.1%	0.07	6.8%	0.06	4.0%	0.27	14.9%	3.90	17.4%	14.64	36.6%	1.27
OSA	8.58	0.1%	0.14	0.1%	0.10	0.2%	0.80	0.4%	11.51	0.1%	14.80	-37.5%	0.86
PAR	8.32	5.0%	0.13	2.9%	0.09	2.5%	0.76	9.2%	10.75	7.3%	15.15	-6.6%	1.15
PEK	7.14	3.3%	0.11	0.2%	0.08	0.1%	0.53	6.5%	8.52	4.9%	5.94	122.5%	0.93
RIO	7.53	7.7%	0.12	6.3%	0.09	6.1%	0.63	16.1%	9.33	13.3%	6.36	42.5%	1.01
SAO	8.85	13.2%	0.14	7.5%	0.10	8.5%	0.81	26.2%	11.74	19.5%	8.95	41.8%	1.05
SEL	8.31	2.3%	0.13	1.3%	0.09	1.1%	0.73	3.7%	10.80	3.1%	25.98	-33.1%	0.80
SGN	6.52	13.8%	0.10	12.6%	0.08	8.9%	0.55	20.5%	7.72	21.8%	3.43	133.9%	0.93
SHA	7.17	4.6%	0.11	0.2%	0.08	0.1%	0.53	10.5%	8.58	6.9%	6.08	123.9%	0.72
SZX	6.46	5.6%	0.10	1.3%	0.07	1.2%	0.42	14.6%	6.86	9.8%	12.93	-25.4%	0.66
THR	8.55	10.9%	0.14	7.7%	0.10	6.8%	0.89	18.0%	11.64	16.1%	22.45	28.6%	0.99
TSN	7.30	4.3%	0.11	0.2%	0.08	0.2%	0.61	8.6%	8.99	6.1%	7.73	122.5%	0.90
TYO	9.04	0.1%	0.15	0.1%	0.10	0.1%	0.87	0.2%	12.25	0.1%	16.15	-37.4%	0.92

Table A.2: Verification of hindcasting simulation including the number of observations (n), root-mean-square error (RMSE), bias, and Pearson correlation coefficient (r). Each observation is the ensemble average of observed temperatures at one station, one time of the day, and one month throughout the 2006–2015 decade. Stations are grouped to urban and non-urban stations using the MODIS land use dataset, which is also inputted to the WRF model. Shenzhen (SHE) and São Paulo (SAO) are covered by Guangzhou (GUA) and Rio de Janeiro (RIO) domains, respectively. Refer to Table 1.1 for city codes. Station locations are shown in Appendix B.

	Urban stations				Non-urban stations			
City	n	RMSE	Bias	r	n	RMSE	Bias	r
AMD	96	1.54	0.90	0.98	0			
BKK	1176	1.26	0.43	0.93	672	0.97	-0.12	0.95
BLR	166	1.29	-0.49	0.95	0			
BOG	288	2.80	2.44	0.96	144	1.18	-0.41	0.87
BOM	192	1.63	0.88	0.96	0			
BUE	755	2.58	1.12	0.98	141	2.48	0.17	0.95
CAI	288	2.07	-0.28	0.98	0			
CAN	1632	2.36	1.81	0.96	384	1.95	1.43	0.97
CCU	220	1.99	0.77	0.96	27	1.85	-0.39	0.97
CKG	288	2.31	1.70	0.98	0			
CTU	288	2.29	2.02	0.99	96	2.49	2.05	0.98
DAC	215	2.47	1.36	0.95	0			
DAR	288	1.00	0.38	0.97	280	1.17	-0.56	0.95
DEL	384	2.26	1.17	0.98	0			
FIH	576	2.21	1.17	0.86	0			
HYD	96	1.27	0.81	0.98	0			
IST	228	2.23	-1.00	0.98	0			
JKT	840	1.38	0.83	0.96	0			
KHI	288	2.03	-0.17	0.96	0			
LAD	214	1.23	0.83	0.98	0			
LAX	144	2.71	-1.60	0.96	0			
LHE	384	2.86	1.42	0.99	126	2.76	0.94	0.98
LIM	288	1.76	1.51	0.96	0			
LON	1440	2.39	-0.52	0.98	864	2.01	-0.67	0.98
LOS	630	0.95	0.21	0.93	0			
MAA	96	1.43	0.12	0.95	0			
MEX	280	2.01	-0.98	0.93	84	1.41	0.39	0.96
MNL	1242	1.13	0.38	0.91	762	1.05	0.12	0.93
MOW	384	2.65	-1.03	0.99	576	3.09	-1.47	0.99
NKG	384	2.64	1.77	0.98	0			
NYC	408	2.37	0.17	0.98	568	2.17	0.05	0.98
OSA	3216	1.77	1.16	0.99	1308	1.57	0.95	0.99
PAR	1440	2.29	-0.11	0.99	1484	2.05	-0.39	0.99
PEK	288	2.50	0.97	0.99	0			
RIO	2892	1.98	0.83	0.91	685	1.50	0.64	0.95
SEL	1536	2.01	0.45	0.99	672	1.67	0.61	0.99
SGN	288	1.69	1.33	0.95	0			
SHA	672	1.95	1.14	0.99	384	1.34	-0.28	0.99
THR	480	2.09	-0.22	0.99	288	2.17	-0.06	0.99
TSN	264	2.59	1.48	0.99	288	2.51	0.84	0.99
TYO	5451	2.08	1.55	0.99	972	1.58	0.78	0.98

Appendix B

Simulation Domain Configuration

Simulation was conducted with a fine domain (2 km resolution) nested in a coarse domain (10 km resolution). Data analysis (except for model verification) was performed for only a part of the fine domain because the minimum recommended domain size of 100 grids by 100 grids is much larger than the actual size of many cities. Analysis domains were chosen to capture metropolitan areas rather than the administrative borders of cities.

The domain configuration for each cities are drawn in the following pages. Cities are listed in lexicographical order. The maps were downloaded from Google Maps.

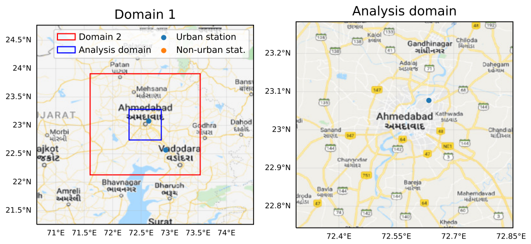
Ahmadabad

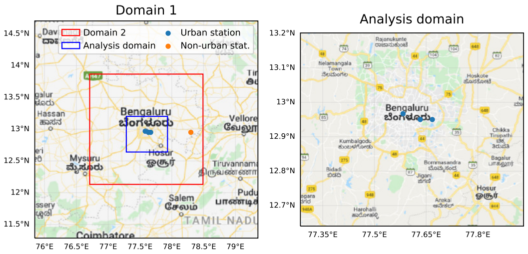
Bangalore

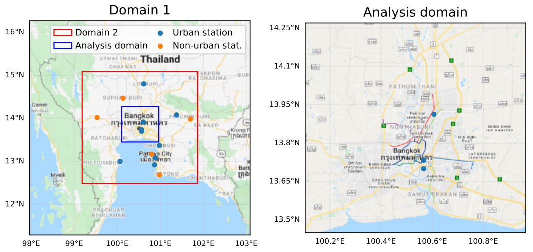
Bangkok

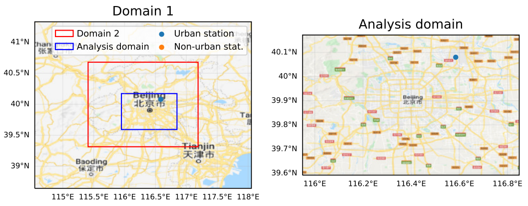
Beijing

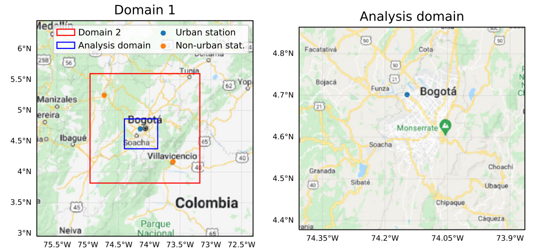
Bogota

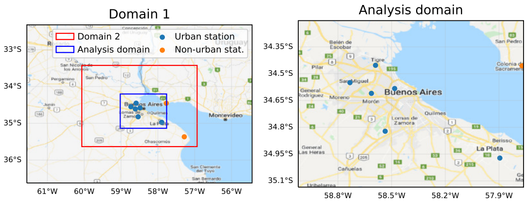
Buenos Aires

Cairo

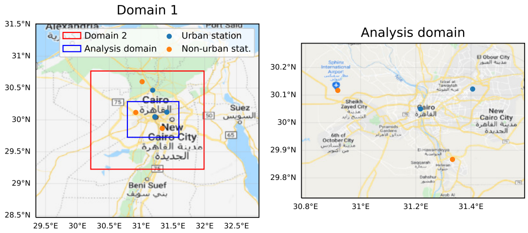

Chengdu

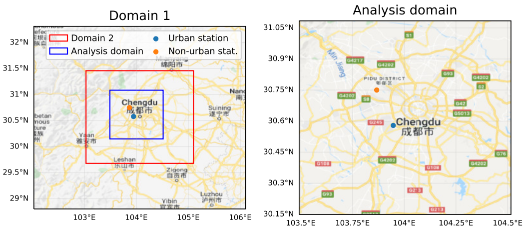

Chennai

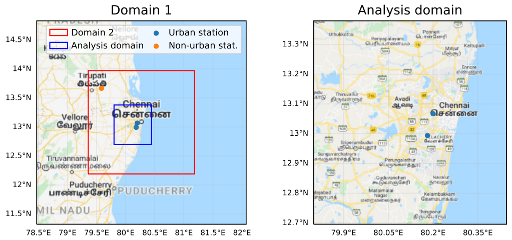

Chongqing

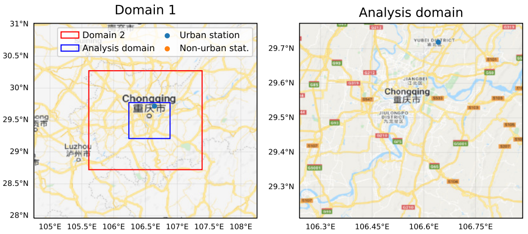

Dar es Salaam

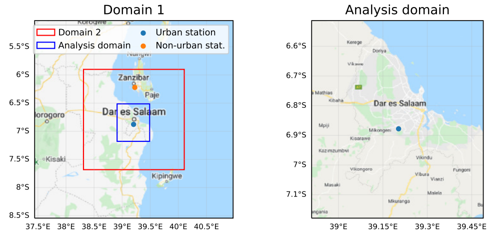

Delhi

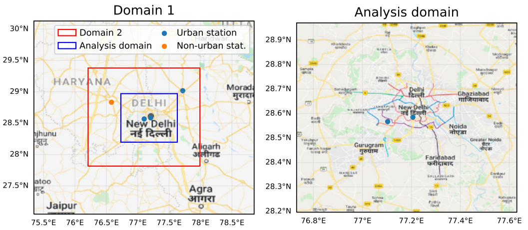

Dhaka

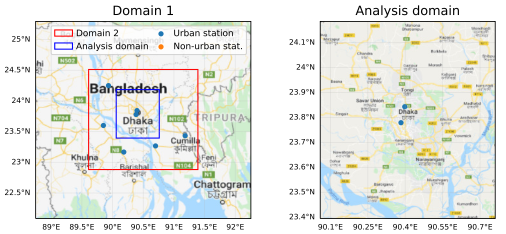

Guangzhou

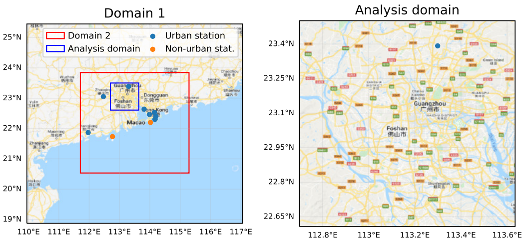

Ho Chi Minh City

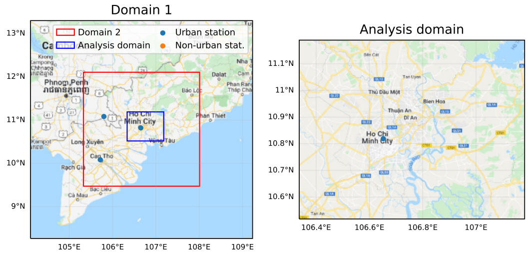

Hyderabad

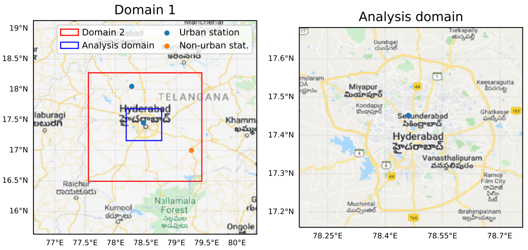

Istanbul

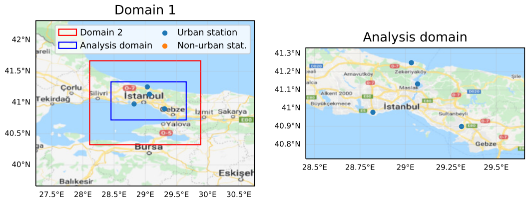

Jakarta

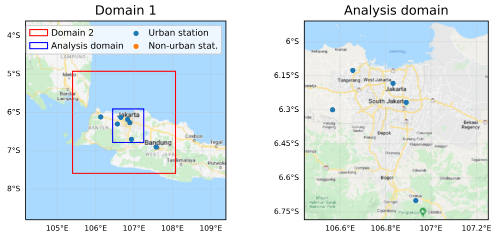

Karachi

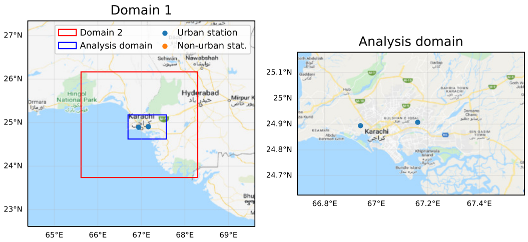

Kinshasa

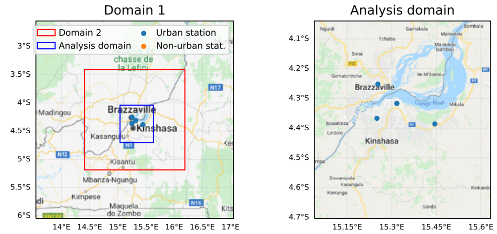

Kolkata

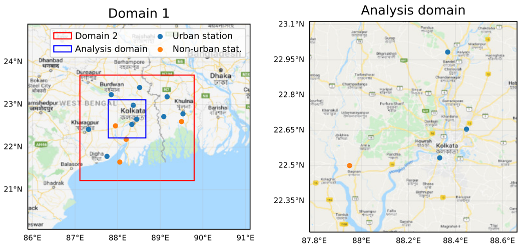

Lagos

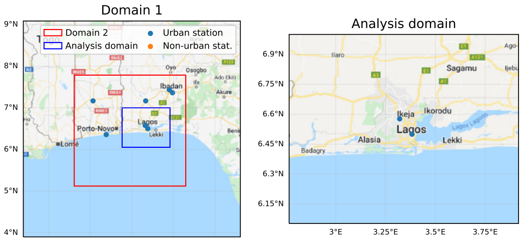

Lahore

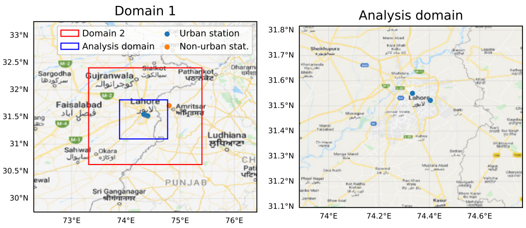

Lima

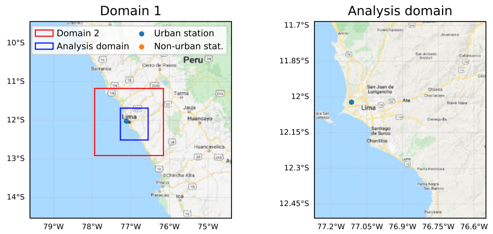

London

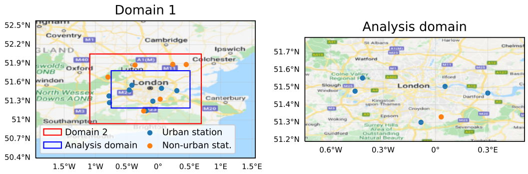

Los Angeles

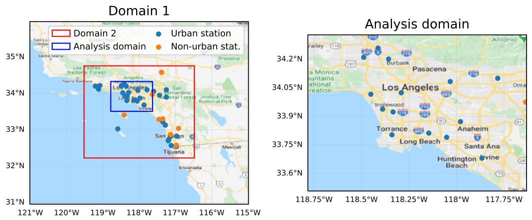

Luanda

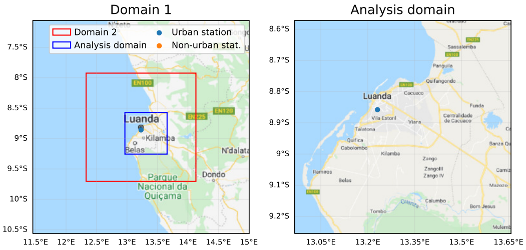

Manila

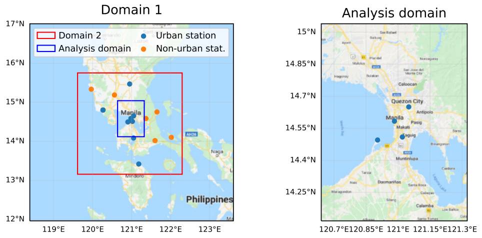

Mexico City

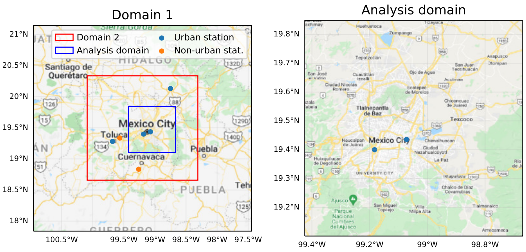

Moscow

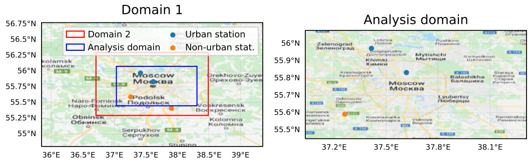

Mumbai

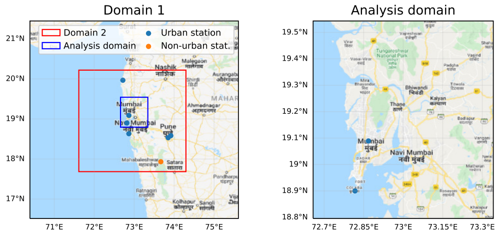

Nanjing

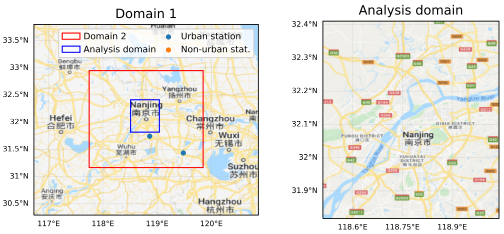

New York

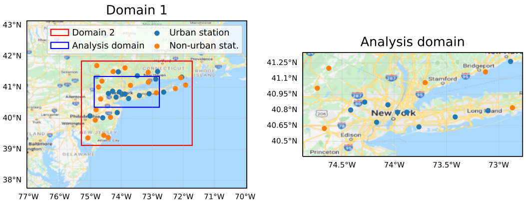

Osaka

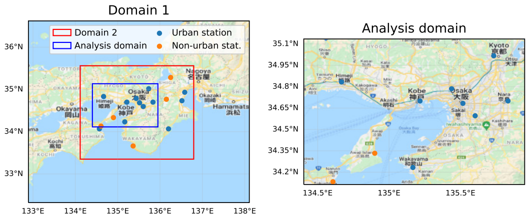

Paris

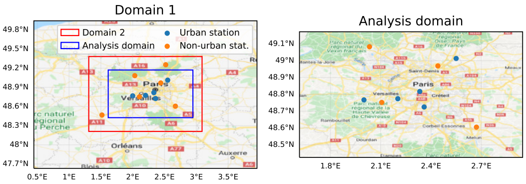

Rio de Janeiro

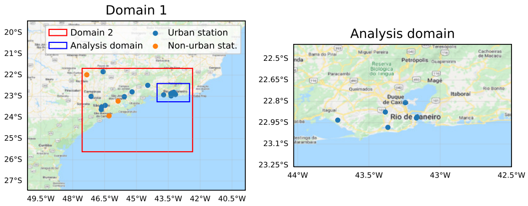

São Paulo

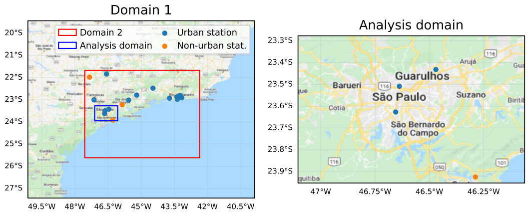

Seoul

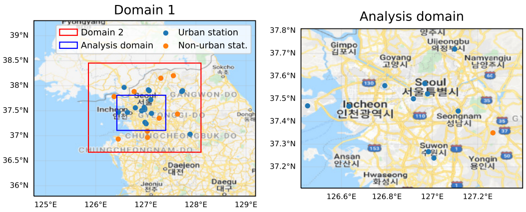

Shanghai

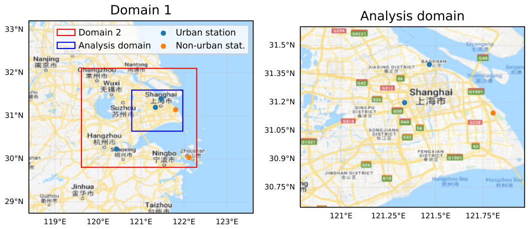

Shenzhen

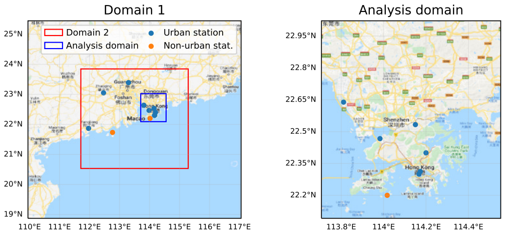

Tehran

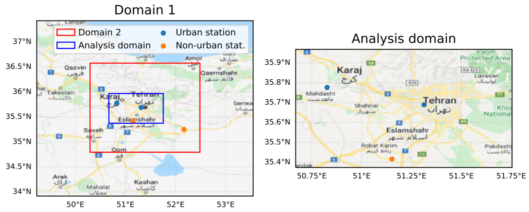

Tianjin

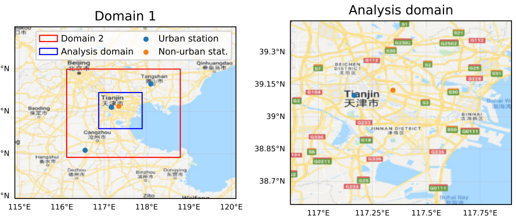

Tokyo

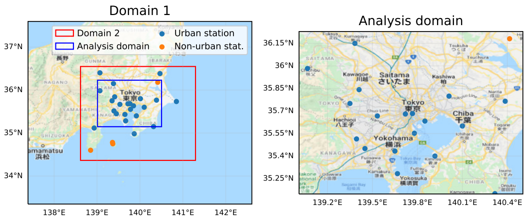

APPENDIX C

Maps of Global Warming and Urbanization Effect

The spatial maps of global warming in the 2050s (in reference to the preindustrial level) and urbanization effect projected for the 43 megacities are listed in this section. Cities are sorted in lexicographical order. Color scales are different among the cities.

Ahmadabad

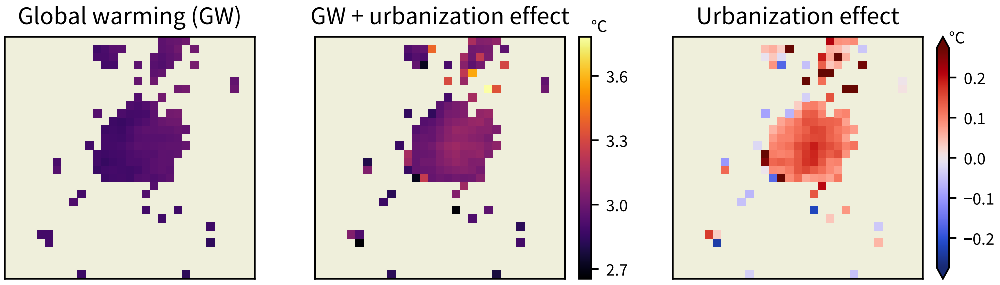

Bangalore

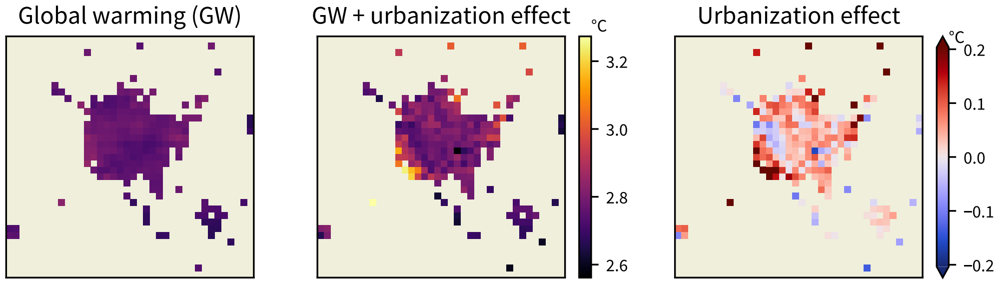

Bangkok

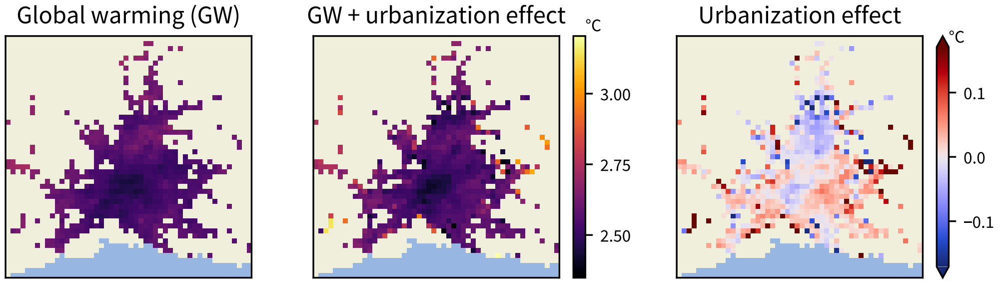

Beijing

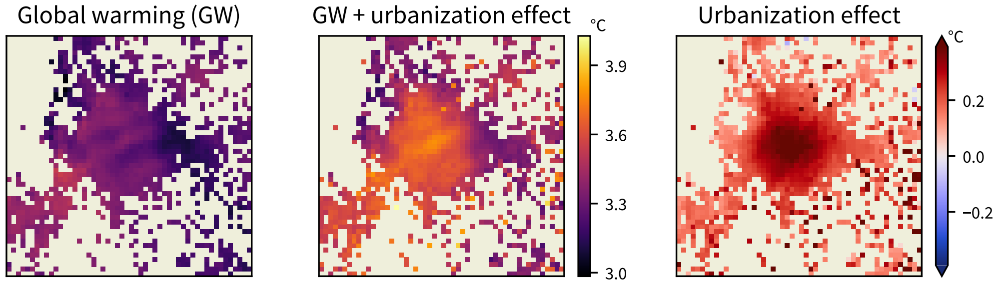

Global warming (GW)

GW + urbanization effect

Urbanization effect

Bogota

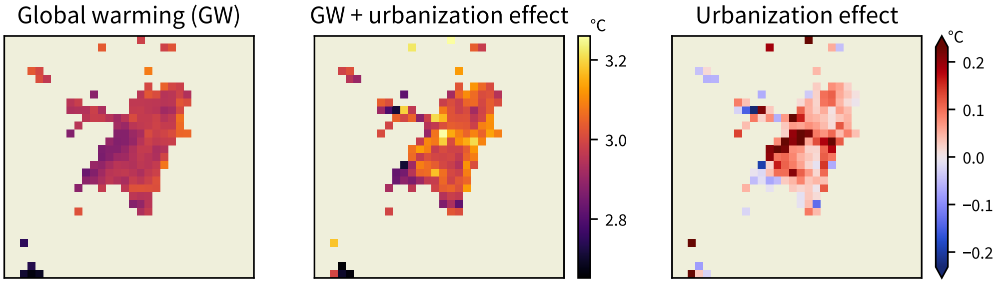

Global warming (GW)

GW + urbanization effect

Urbanization effect

Buenos Aires

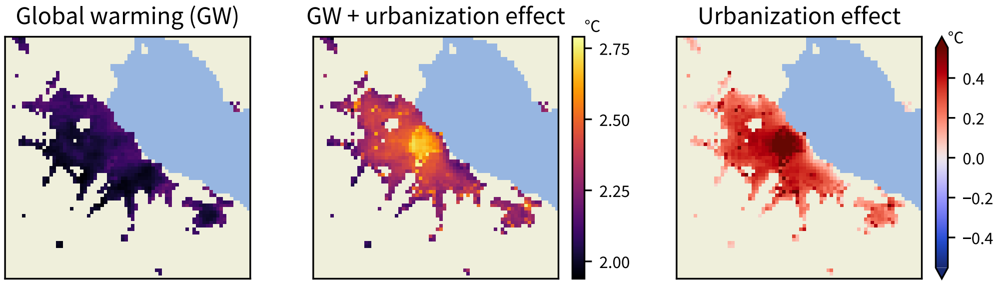

Global warming (GW)

GW + urbanization effect

Urbanization effect

Cairo

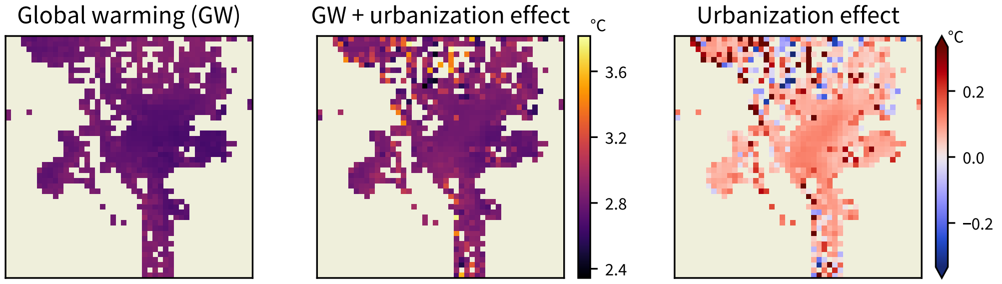

Global warming (GW)

GW + urbanization effect

Urbanization effect

Chengdu

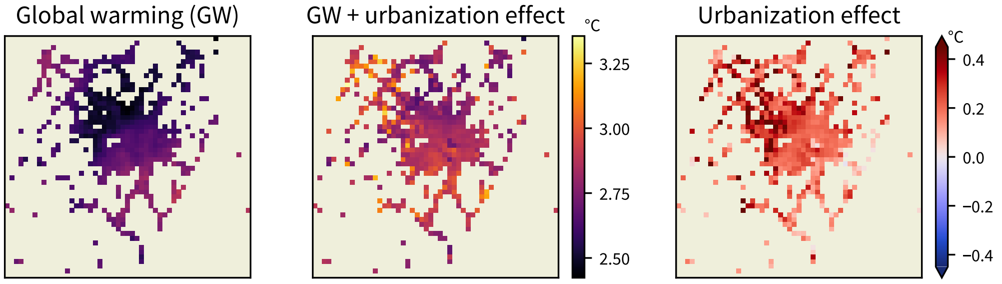

Global warming (GW)

GW + urbanization effect

Urbanization effect

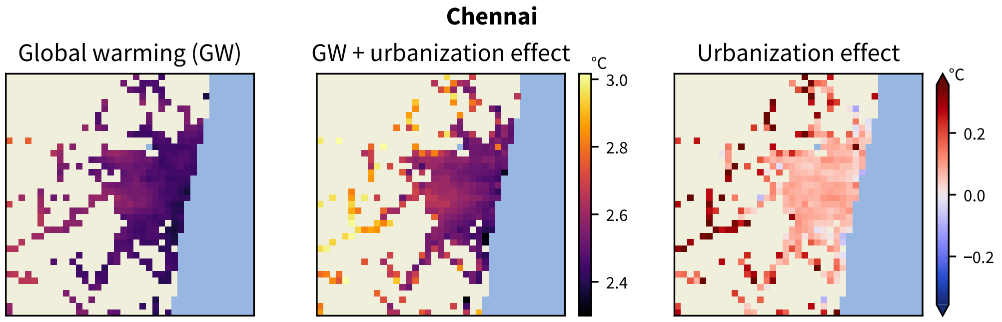
Chennai
Global warming (GW)
GW + urbanization effect
°C
3.0
2.8
2.6
2.4
Urbanization effect
°C
0.2
0.0
−0.2

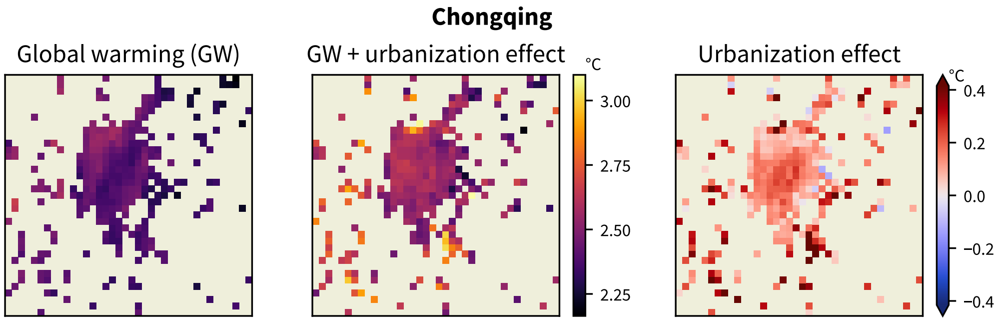
Chongqing
Global warming (GW)
GW + urbanization effect
°C
3.00
2.75
2.50
2.25
Urbanization effect
°C
0.4
0.2
0.0
−0.2
−0.4

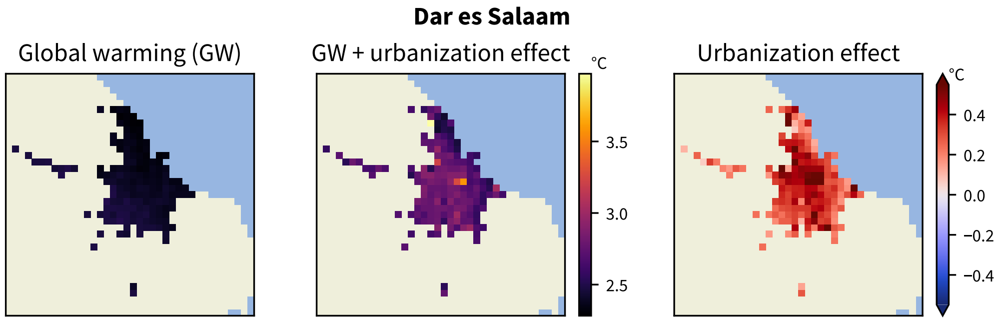
Dar es Salaam
Global warming (GW)
GW + urbanization effect
°C
3.5
3.0
2.5
Urbanization effect
°C
0.4
0.2
0.0
−0.2
−0.4

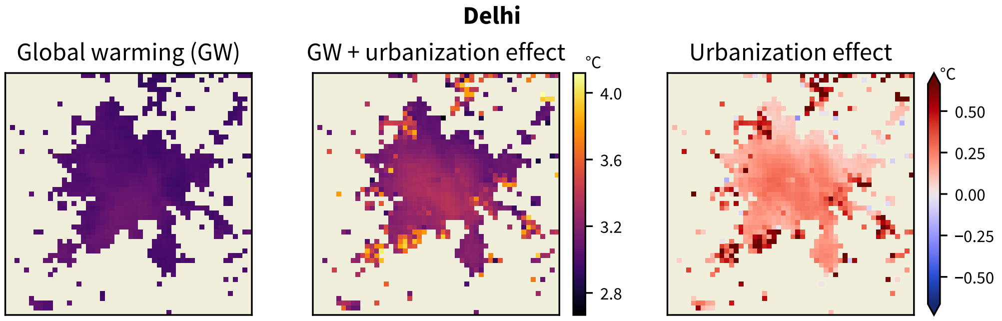
Delhi
Global warming (GW)
GW + urbanization effect
°C
4.0
3.6
3.2
2.8
Urbanization effect
°C
0.50
0.25
0.00
−0.25
−0.50

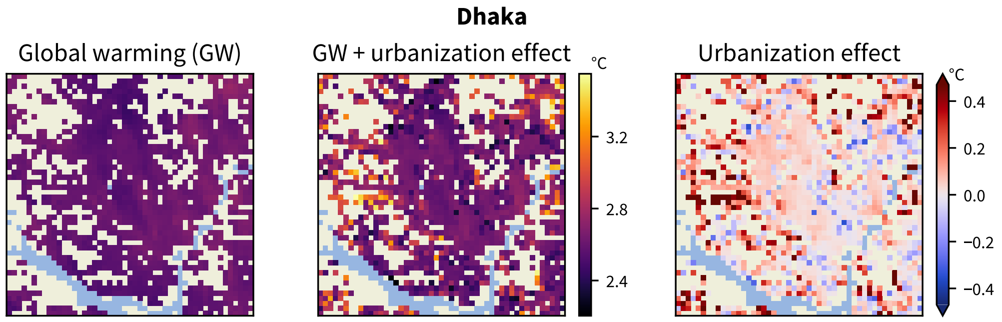
Dhaka
Global warming (GW)
GW + urbanization effect
°C
3.2
2.8
2.4
Urbanization effect
°C
0.4
0.2
0.0
−0.2
−0.4

Guangzhou

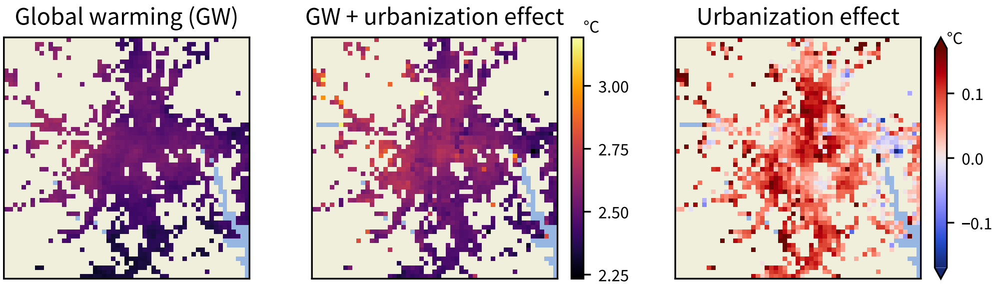

Ho Chi Minh City

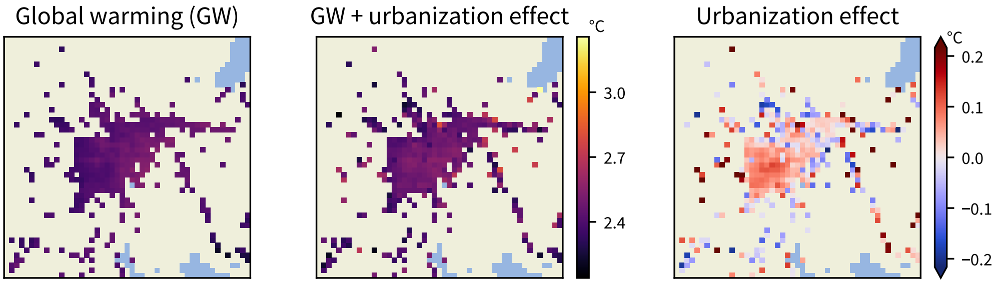

Hyderabad

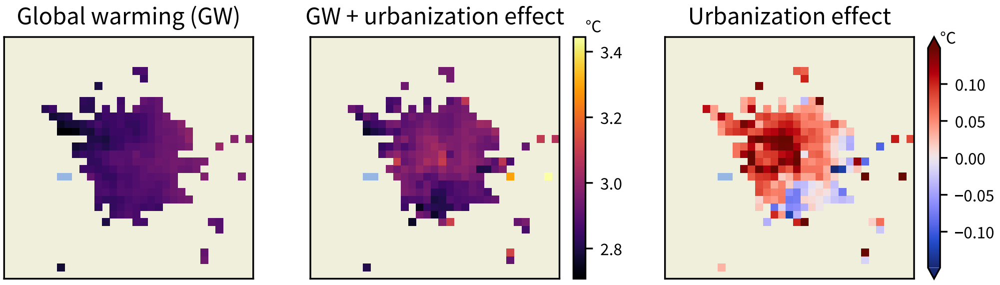

Istanbul

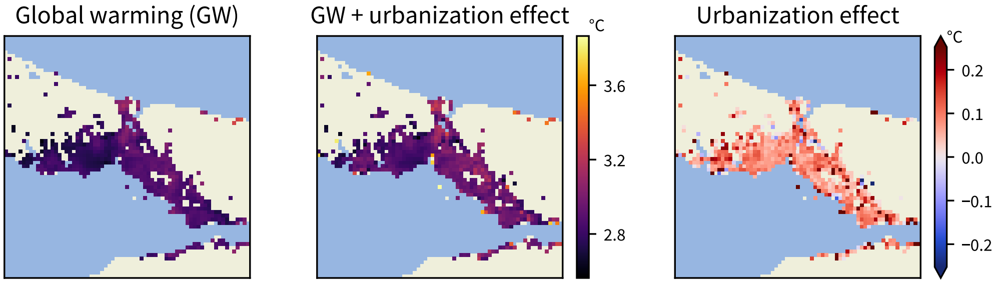

Jakarta

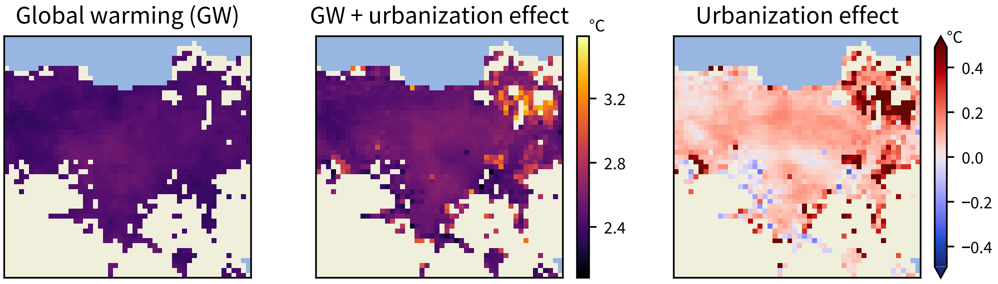

Karachi

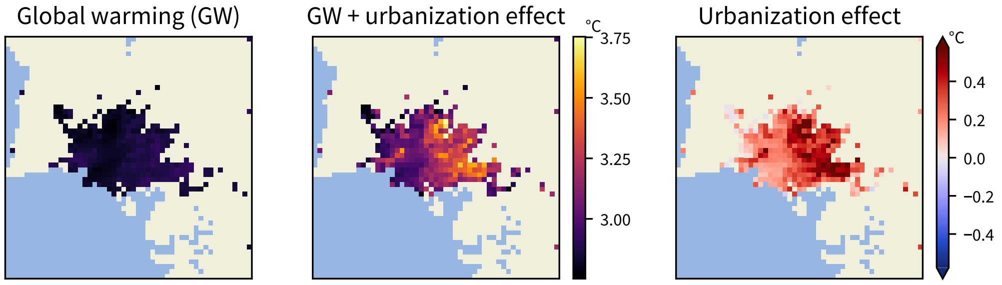

Kinshasa

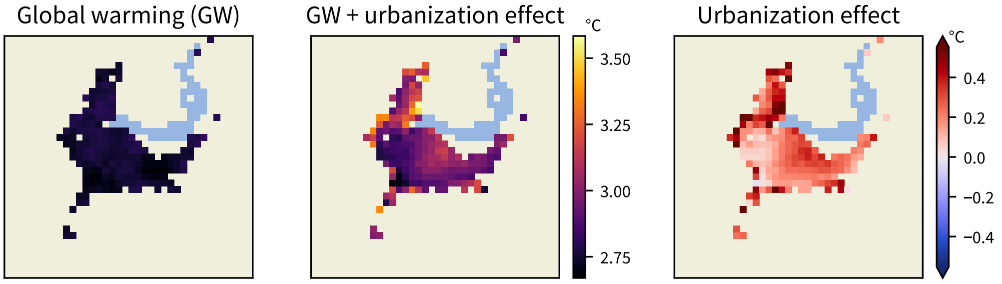

Kolkata

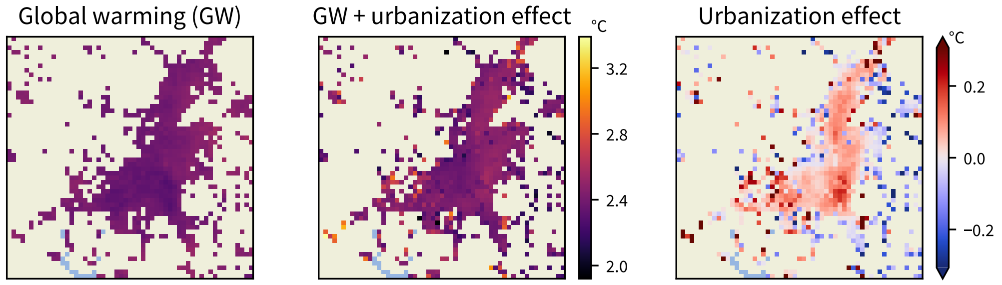

Lagos

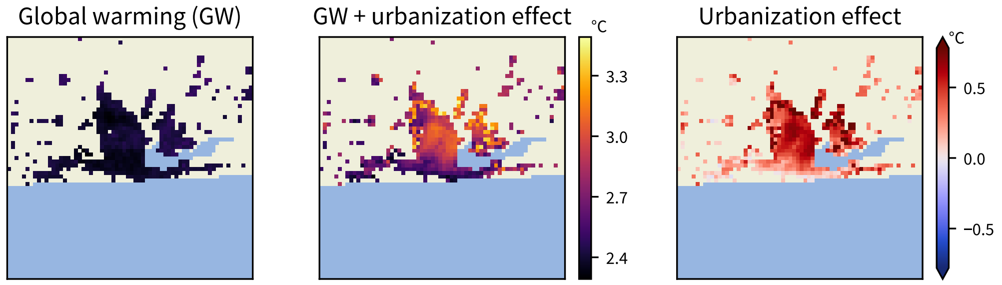

Lahore

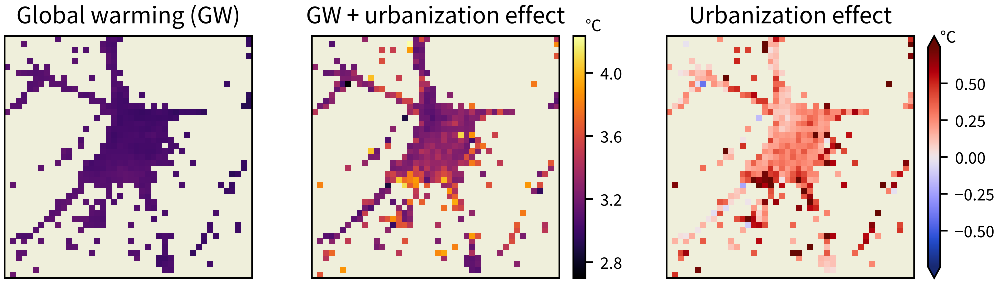

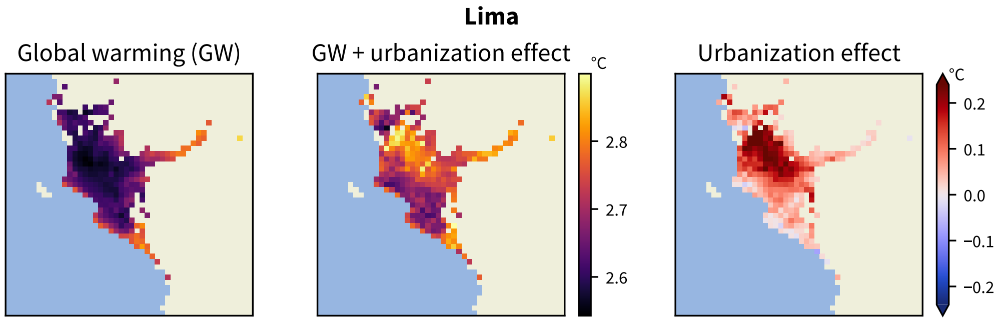

Lima

Global warming (GW)

GW + urbanization effect

Urbanization effect

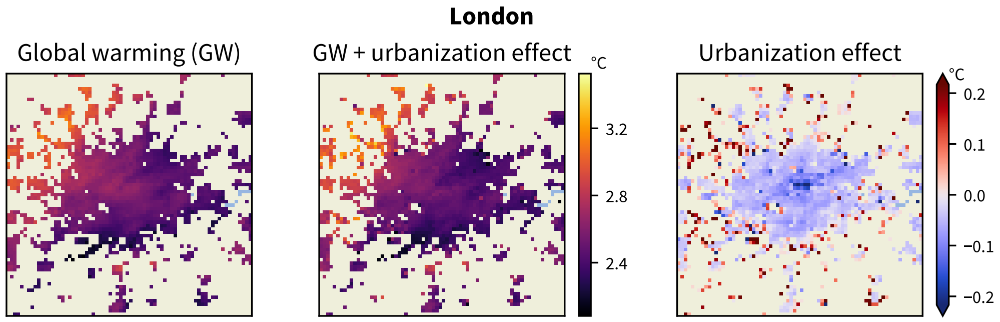

London

Global warming (GW)

GW + urbanization effect

Urbanization effect

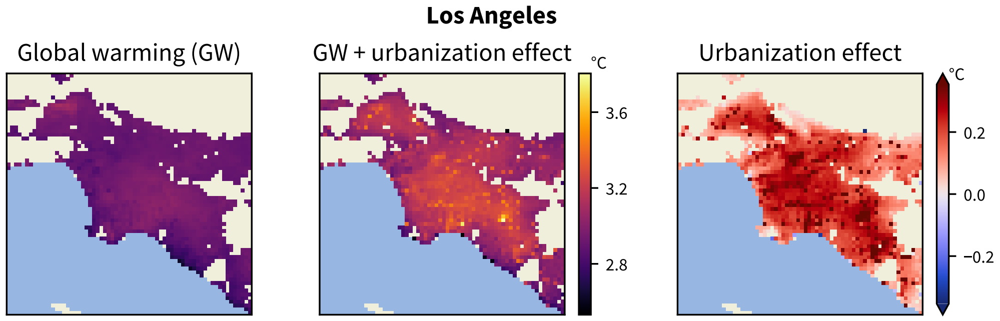

Los Angeles

Global warming (GW)

GW + urbanization effect

Urbanization effect

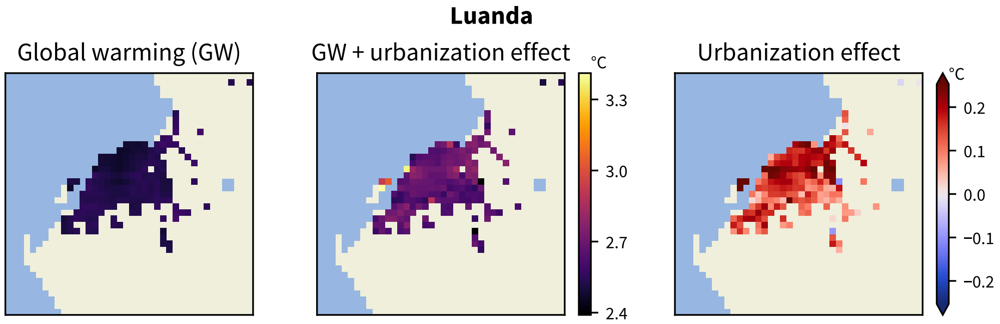

Luanda

Global warming (GW)

GW + urbanization effect

Urbanization effect

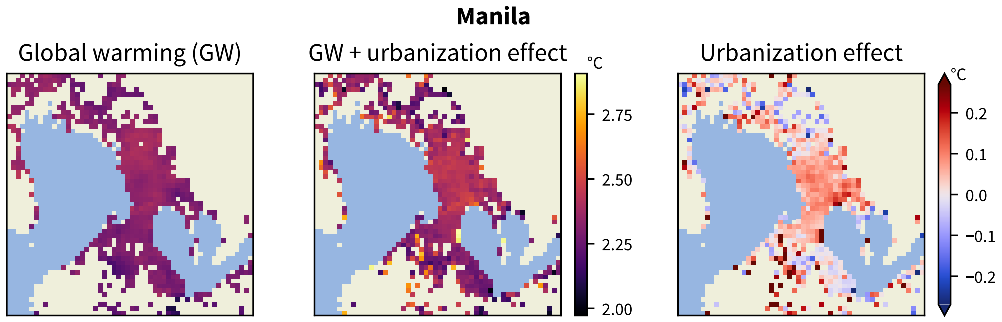

Manila

Global warming (GW)

GW + urbanization effect

Urbanization effect

Mexico City

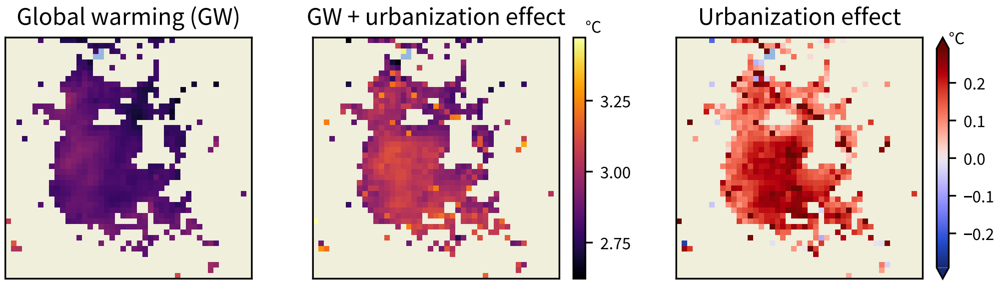

Moscow

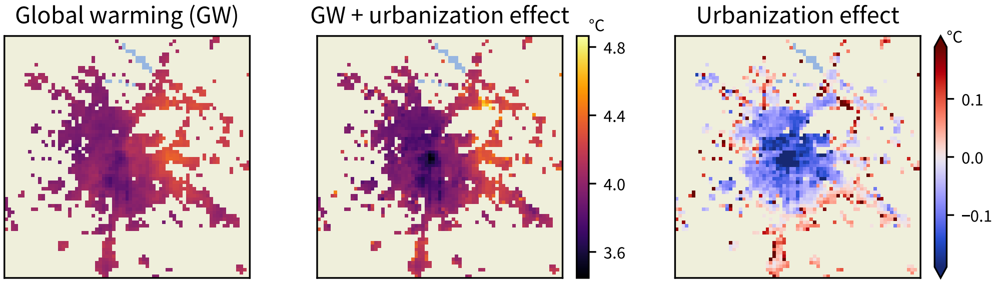

Mumbai

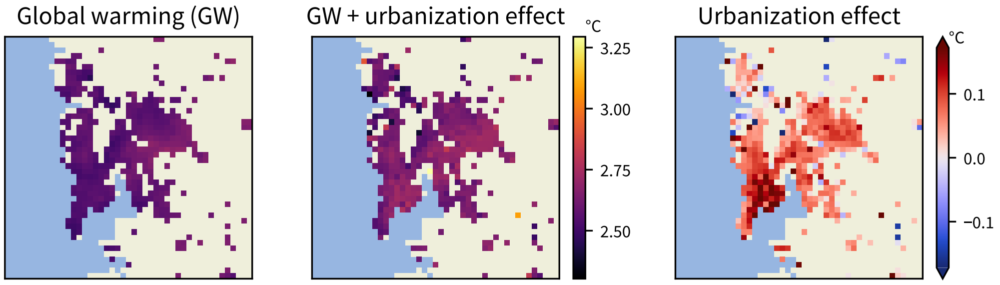

Nanjing

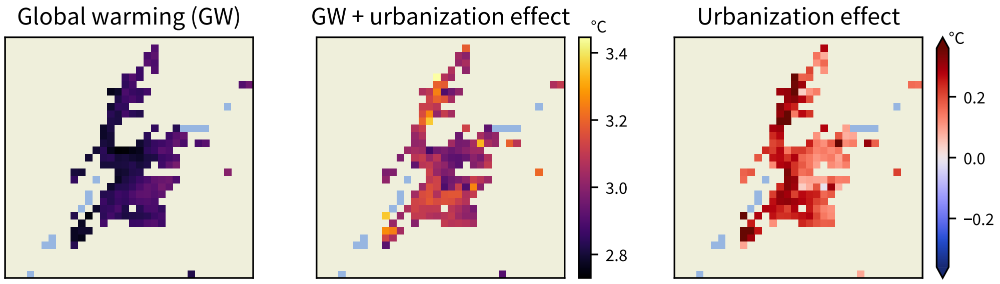

New York

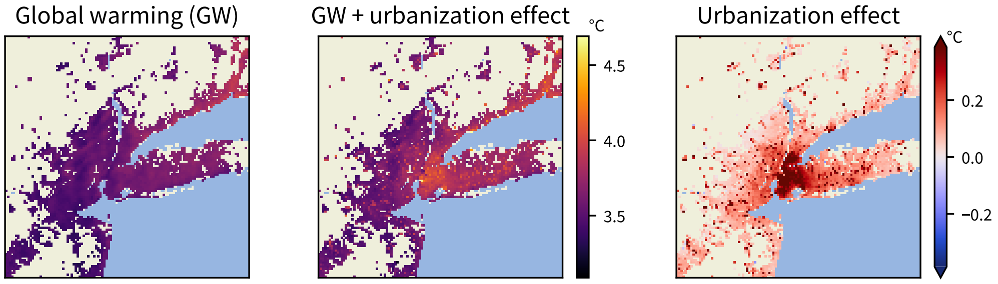

Osaka

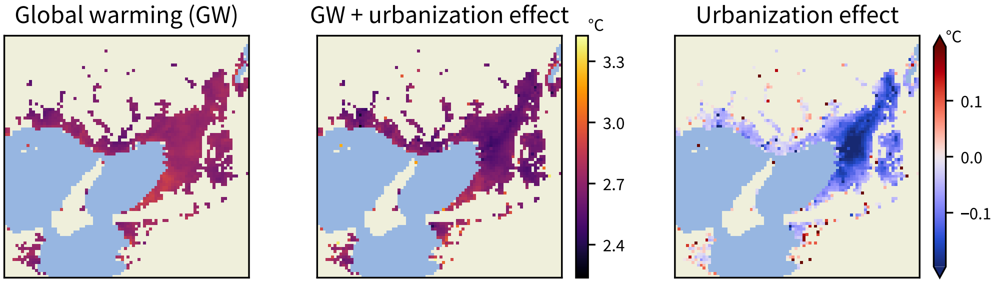

Paris

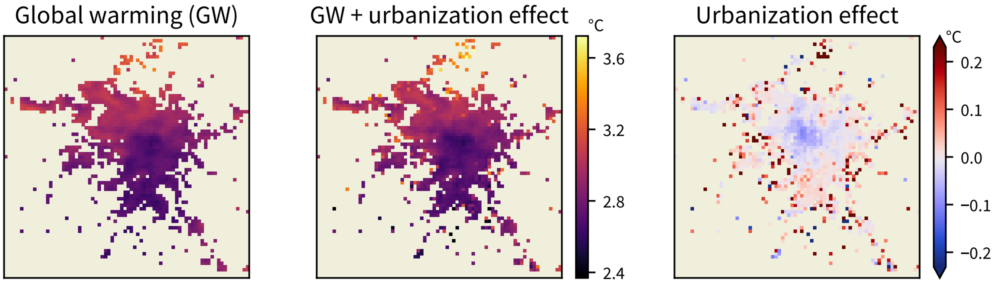

Rio de Janeiro

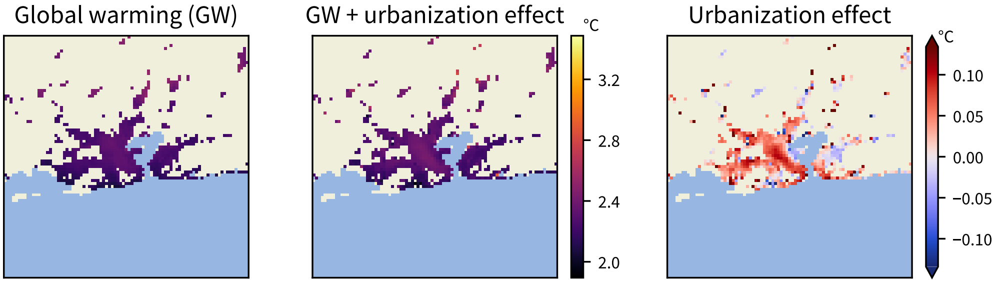

Seoul

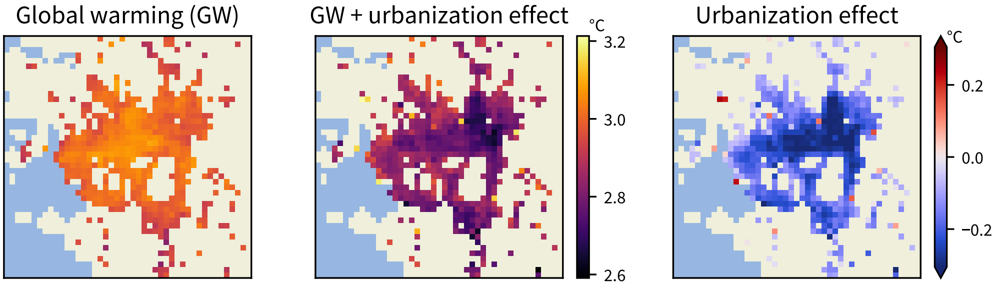

Shanghai

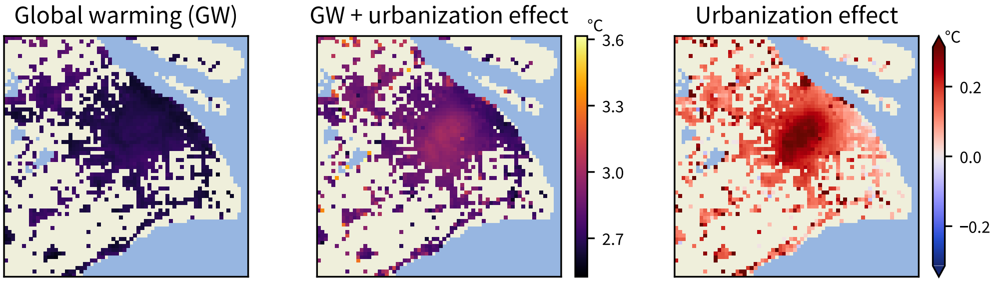

Shenzhen

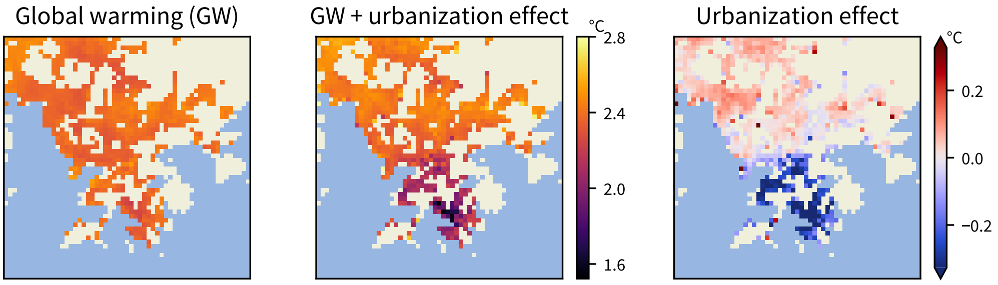

São Paulo

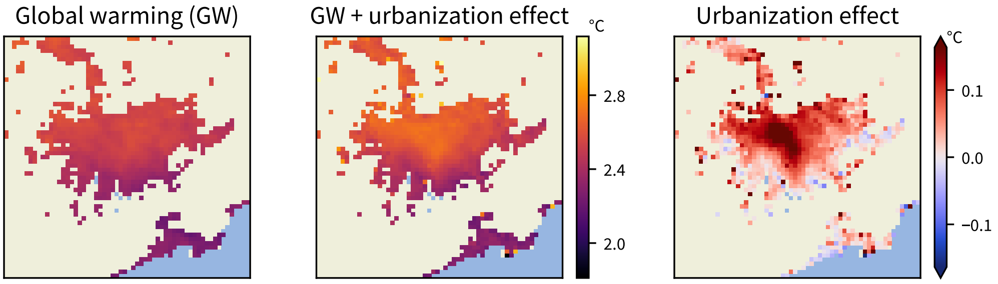

Tehran

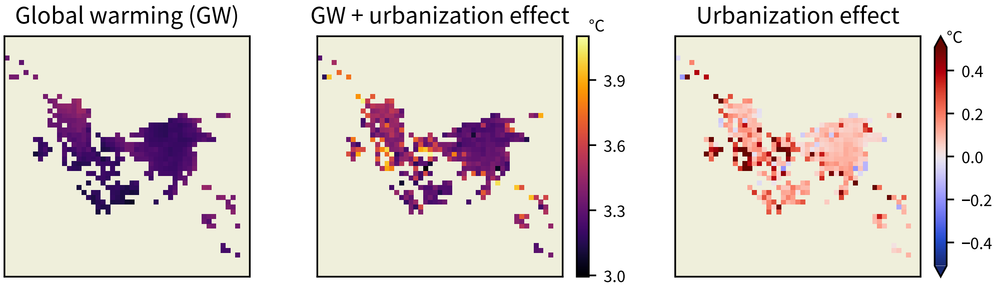

Tianjin

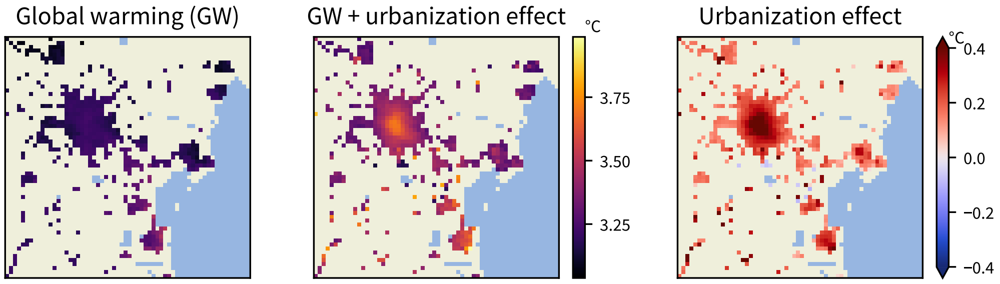

Tokyo